FORMATION OF POROUS SILICON CARBIDE AND ITS SUITABILITY AS A
CHEMICAL AND TEMPERATURE DETECTOR

BY

TILGHMAN LEE RITTENHOUSE

B.S., United States Air Force Academy, 1994
M.S., Massachusetts Institute of Technology, 1999

DISSERTATION

Submitted in partial fulfillment of the requirements
for the degree of Doctor of Philosophy in Chemistry
in the Graduate College of the
University of Illinois at Urbana-Champaign, 2004

Urbana, Illinois

Report Documentation Page

*Form Approved
OMB No. 0704-0188*

Public reporting burden for the collection of information is estimated to average 1 hour per response, including the time for reviewing instructions, searching existing data sources, gathering and maintaining the data needed, and completing and reviewing the collection of information. Send comments regarding this burden estimate or any other aspect of this collection of information, including suggestions for reducing this burden, to Washington Headquarters Services, Directorate for Information Operations and Reports, 1215 Jefferson Davis Highway, Suite 1204, Arlington VA 22202-4302. Respondents should be aware that notwithstanding any other provision of law, no person shall be subject to a penalty for failing to comply with a collection of information if it does not display a currently valid OMB control number.

1. REPORT DATE **19 AUG 2004**	2. REPORT TYPE **N/A**	3. DATES COVERED **-**

4. TITLE AND SUBTITLE **Formation Of Porous Silicon Carbide And Its Suitability As A Chemical And Temperature Detector**	5a. CONTRACT NUMBER
	5b. GRANT NUMBER
	5c. PROGRAM ELEMENT NUMBER
6. AUTHOR(S)	5d. PROJECT NUMBER
	5e. TASK NUMBER
	5f. WORK UNIT NUMBER

7. PERFORMING ORGANIZATION NAME(S) AND ADDRESS(ES) **University of Illinois at Urbana**	8. PERFORMING ORGANIZATION REPORT NUMBER

9. SPONSORING/MONITORING AGENCY NAME(S) AND ADDRESS(ES)	10. SPONSOR/MONITOR'S ACRONYM(S)
	11. SPONSOR/MONITOR'S REPORT NUMBER(S)

12. DISTRIBUTION/AVAILABILITY STATEMENT
Approved for public release, distribution unlimited

13. SUPPLEMENTARY NOTES
The original document contains color images.

14. ABSTRACT

15. SUBJECT TERMS

16. SECURITY CLASSIFICATION OF:			17. LIMITATION OF ABSTRACT **UU**	18. NUMBER OF PAGES **150**	19a. NAME OF RESPONSIBLE PERSON
a. REPORT **unclassified**	b. ABSTRACT **unclassified**	c. THIS PAGE **unclassified**			

Standard Form 298 (Rev. 8-98)
Prescribed by ANSI Std Z39-18

FORMATION OF POROUS SILICON CARBIDE AND ITS SUITABILITY AS A
CHEMICAL AND TEMPERATURE DETECTOR

Tilghman Lee Rittenhouse, Ph. D.
Department of Chemistry
University of Illinois at Urbana-Champaign, 2004
Paul W. Bohn, Advisor

The need to sense chemical mixtures in a variety of hostile environments (such as high temperature caustic gases) continues to grow. However, silicon electrical devices are limited to relatively low temperatures ($< 250\ ^{o}$C). For this reason, wide bandgap materials such as silicon carbide have received increased attention. Current SiC sensors such as Schottky diodes composed of catalytic metals show deficiencies such as unacceptable drift in the signal. Alternative sensor structures, such as porous semiconductors, may provide improved sensor performance.

A novel electroless method of producing porous silicon carbide (PSiC) is presented. Unlike anodic methods of producing PSiC, the electroless process does not require electrical contact during etching. Rather, platinum metal deposited on the wafer before etching serves as a catalyst for the reduction of a chemical oxidant, which combined with UV illumination injects holes into the valence band, the holes subsequently participating in the oxidation and dissolution of the substrate. The etchant is composed of HF and $K_2S_2O_8$ in water. Various porous morphologies are presented as a function of etchant concentration, time of etching, and SiC polytype. Wafer quality is of the utmost concern when utilizing the electroless wet etchant, since defects such as stacking faults, dislocations, and micropipes have a large impact on the resulting porous structure.

Results of imaging and spectroscopic characterization are presented and compared to PSiC produced via anodic etching of the same wafer material. In general, it is found that electrolessly etched PSiC has photoluminescent, cathodoluminescent, and Raman scattering properties relatively unchanged from bulk SiC. However, the spectroscopic properties of the anodically etched PSiC were dramatically different than those found for bulk SiC. Cathodoluminescence studies of anodically etched porous layers yield luminescence peaks in the ultraviolet region (energies higher than the bandgap energy of bulk SiC). Additional spectroscopic results (photoluminescence, Raman emission) have been collected from the

same porous films in order to determine the origin of the UV cathodoluminescence emission. The photoluminescence from these samples showed a wide range of peak luminescence and can be linked to the degree of etching in the porous film. Raman scattering spectra show the development of Fröhlich modes as etching proceeds. Therefore, although quantum confinement is one possible cause of the UV cathodoluminescence, other results indicate that defect structures or surface state species are the most likely origin of the UV emission.

Anodically etched PSiC films are then investigated for their suitability as chemical and temperature detectors particularly suited for high temperature, caustic environments. Studies utilizing interferometry as well as conductivity have been conducted. PSiC layers were unresponsive in interferometry for a wide variety of adsorbate gases, and this method of analyte detection proved unsuccessful.

Ohmic contacts to PSiC were investigated in order to study changes in the bulk conductivity of the semiconducting skeleton when exposed to various chemical and temperature conditions. Conductometric investigations show that PSiC has a measurable response to high concentrations of hydrogen gas (~6% decrease in resistance when exposed to 20% H_2) comparable to currently used platinum alloy resistive films. However, similar to the resistive films, strict temperature control of the PSiC sensor is necessary. Current hydrogen sensing arrays may be improved by the introduction of a PSiC sensor for the specific role of high concentration sensing. Eventually, it may be possible to form an array of PSiC sensors capable of distinguishing the concentrations of individual components within a gas flow as well as the temperature of the gas flow.

ACKNOWLEDGMENTS

TABLE OF CONTENTS

CHAPTER 1

INTRODUCTION

1.1 Motivation

Today, the need for high temperature sensing of hydrogen within gas mixtures is finding

increased attention. Within the aerospace industry specifically, there is a need for sensors that can be

used in fuel leak detection, fire safety monitoring, and engine emission monitoring. For example, the

ability to monitor the exhaust of a jet or rocket engine would allow for much greater safety and engine

performance. However, these exhausts can be expected to be at high temperature and contain caustic

species in addition to the hydrogen to be detected. A solid state device that can monitor these exhaust

gases *in situ* does not exist.

The current widespread use of silicon in electronics (primarily due to the facility with which an

insulating oxide can be formed) combined with the ability to obtain highly pure silicon inexpensively has

made it the most studied semiconductor to date. However, silicon carbide has several intrinsic properties

that make it favorable to silicon for some applications, especially those that are at elevated temperature or

in caustic environments,[1-3] as shown in Table 1.1. Si is typically limited to approximately 250 ^{o}C in

electronic applications and about 600 ^{o}C in mechanical devices; Si microelectromechanical systems

operating in excess of 250 ^{o}C would require the use of bulky cooling schemes.[4] However, due to its

stability at high temperature and in harsh chemical environments, SiC can operate in conditions in which

Si fails. Sensing applications that play to silicon carbide's strengths include rocket engines, nuclear

reactors, materials growth chambers, automotive systems, and other high temperature, caustic

environments. For these reasons, SiC was chosen as the sensor material for this work.

SiC-based distributed control electronics are envisioned to eliminate 90% of the wiring and

connectors needed in conventional sheltered-electronic aircraft control systems.[5] For the U.S. Air Force,

SiC sensors implemented on an F-16 would result in 800 pounds of reduced weight. In addition, the

occurrence of wiring and connector problems (the most frequent cause of propulsion maintenance action

Table 1.1. Properties of Si and SiC

Material	Melting Point (Si)/ Sublimation Point (SiC) (^{o}C)	Thermal Conductivity at 298 K (W/m*K)	Breakdown Electric Field (V/m)	Saturation Electron Drift Velocity at 298 K (m/s)	Bandgap (eV)
Si	1410	150	3×10^{7}	0.9×10^{5}	1.1
4H/6H-SiC	2700	370-490	$2\text{-}4 \times 10^{8}$	2.0×10^{5}	3-3.3

and downtime in aircraft today) would be greatly reduced. For commercial jetliners, the increased fuel efficiency, weight savings, and reduced pollution would carry large economic and environment payoffs. It has been estimated that the economic savings value of high temperature SiC-based electronics would result in savings of millions of dollars per aircraft over the course of an aircraft's multi-decade operational lifetime.

1.2 Current Crystalline Semiconductor Sensor Studies

The literature details numerous efforts utilizing crystalline wafers of silicon carbide to detect hydrogen gas flow at various elevated temperatures. Most of these studies have revolved around conductometric methods of detection. SiC sensors for hydrogen gas have taken the form of either Schottky diodes, metal-insulator-SiC capacitors, or occasionally field effect transistor (FET) geometries.

The Schottky diodes utilize a metal gate material (usually the catalytic metals Pt or Pd) bonded directly to the SiC substrate with only a very thin (~2-5 nm thick) oxide separating the metal from the semiconductor. Hydrogen or hydrogen-containing species dissociatively adsorb to the metal and hydrogen atoms migrate to the metal-SiC interface, creating a polarized layer on the semiconductor surface. The work function of the metal decreases, accompanied by a lowering of the Schottky barrier height at the metal/SiC interface. Furthermore, in a Schottky diode structure, it is possible the thinness of the oxide allows for tunneling of electrons through the junction. The result is an exponential change in the current or a quadratic change in the capacitance of the device. The change in conductivity is measured and can be correlated to surface concentrations and to the levels of the sampled gas in the ambient. The advantage of a Schottky diode sensing structure in gas sensing applications is its high

2

sensitivity. However, numerous studies have shown that interfacial reactions between the gate metal and the SiC change the diode properties, and the metal-SiC structure must some how be stabilized in order to eliminate drift in sensor properties for long term operation at elevated temperatures.

Metal-insulator-SiC (MISiC) devices utilize a thicker insulating layer between the metal gate and the SiC substrate. Often the insulating layer is thermally- or ozone-grown oxide SiO_2 (MOSiC), but other insulating layers such as AlN[6,7] have been studied. Recent studies have also investigated the use of reactive insulators (such as SnO_2) as the barrier between the gate metal and the SiC substrate.[8] Regardless of the insulating material used, the adsorbing gas changes the space charge region under the metal clusters at the metal-insulator interface. This thicker insulating junction does not allow for tunneling, but rather relies solely upon a field effect for its sensing capabilities. The presence of the insulating layer aids in reducing reactions between the gate metal and the underlying semiconductor substrate. However, interfacial reactions have still been shown to have detrimental effects on device performance. Also as a result of the relatively thick insulating layer, MISiC devices have lower sensitivity than Schottky diode devices.

Field effect transistor devices again rely upon a fairly thick insulating layer at the gate, covered by a catalyzing metal such as Pt. However, now instead of a capacitor configuration, additional electrodes are configured as a source and a drain. A voltage applied between the source and drain contacts causes a current to flow between the contacts, through a channel region. The concentration of mobile carriers in the channel region is responsive to the ambient gas environment surrounding the gate electrode. Unfortunately, these field effect transistor devices suffer from many of the same problems encountered with MISiC devices, namely interdiffusion reactions and reduced sensitivity as compared to Schottky diodes.

Therefore, despite rapid improvement over the past decade, each of these devices has encountered technological hurdles that still need to be overcome before an operable device can be manufactured and installed. These shortcomings will be discussed and illustrated further in Chapter 4 of this dissertation.

1.3 Current Porous Semiconductor Sensor Studies

Although first discovered in 1956,[9] porous semiconductors have received particularly increased attention in the past decade. Porous semiconductors are attractive candidates for several potential applications; their inherent high surface area makes porous semiconductors particularly attractive for sensing applications. However, few reports detail the investigation of porous silicon (PSi) sensors, and even fewer studies of porous silicon carbide (PSiC) sensing have been reported. It appears that the widespread use of a porous semiconductor is most likely years away.

One vein of research with PSi sensors has utilized Fabry-Perot interference fringes.[10-13] When light is reflected from a porous film, the reflected spectrum will show fringes whose spacing is dependent upon the refractive index of the porous film (Fig. 1.1).[11] This detection method has been successful for measuring biomolecules as well as vapors of organic solvents such as ethanol in the hundreds of ppb. It has been proposed that capillary condensation is the primary cause of refractive index changes in the PSi film.[12] However, this method has not been shown to be effective in measuring gases that have refractive indices very near that of air or inert gases (such as H_2). In addition, signal from these devices can drift as silicon in the porous film oxidizes (Fig. 1.2).[12,14]

Similar to the Fabry-Perot interference fringe work described above, Snow et. al. has made PSi devices that act as Bragg mirrors.[15] Snow et. al. theorize that capillary condensation of organic vapors (saturated vapors of acetone and chlorobenzene) lead to the relatively large (75-125 nm) shifts in reflection fringes they witness.

PSi devices have also been studied via conductometric studies. In general, conductometric devices can be expected to be more straightforward and easier to apply in many sensing applications than optical interference measurements. Schechter et. al. conducted some of the earliest conductometric studies.[16] Schechter et. al. report large changes in conductivity through a Schottky contact when a PSi sensor is exposed to a vapor with a large dipole moment (such as methanol or acetone). After investigating a variety of adsorbate gases, Schechter et. al. concluded that the increase in conductivity was
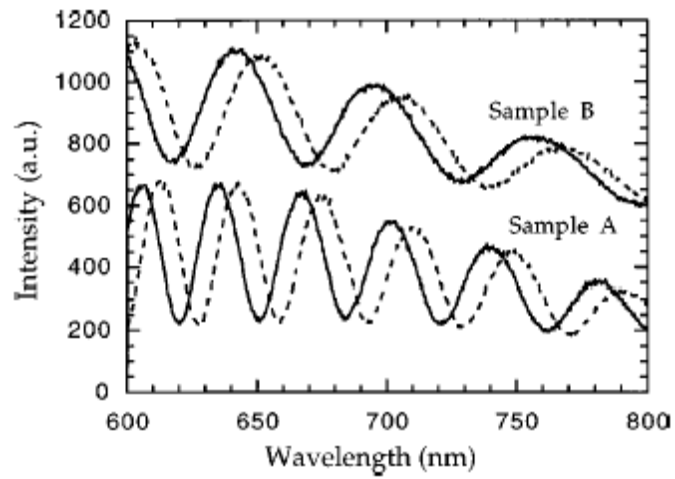
Figure 1.1.[11] Reflection spectra of two porous silicon thin films with different thicknesses, in air (solid curves) and after exposure to 1.7% ethanol in air (dashed curves). The Fabry-Perot interference fringes shift as a result of the change in the dielectric constant of the porous layer.
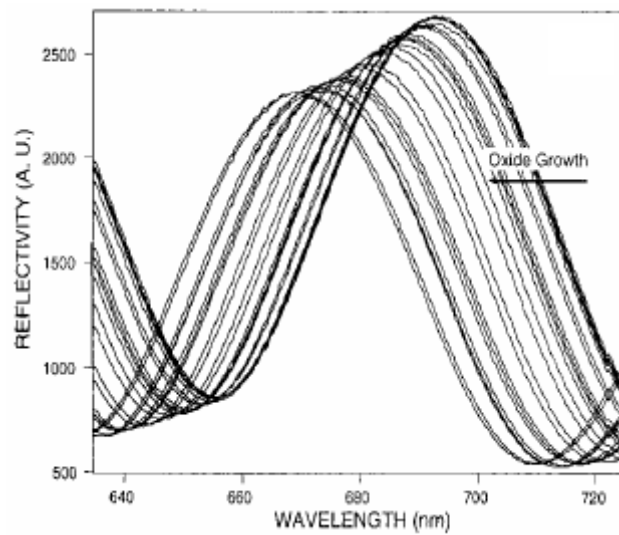
Figure 1.2.[14] Reflection spectra from a porous silicon film during the growth of native oxide over the course of ten days. The Fabry-Perot fringe shifts to the blue upon oxidation of the PSi film, representing a change in baseline for the device over time.

dependent upon the adsorbate's dipole moment. They further proposed that the increases in conductivity are due to an increase in the density of charge carriers within the porous nanostructure.

The results[17] of Kim et. al. are similar in nature to those reported by Schechter. Kim et. al. report ethanol, methanol, and acetone vapor detection near room temperature with porous silicon devices. Kim's FET devices are rectifying in nature, at least partially due to interfaces between n^+ silicon with p-type porous silicon regions. With 5 V applied, Kim et. al. report a seven-fold increase in current flow when the device is exposed to 0.5% ethanol (Fig. 1.3).[17] They propose that capillary condensation of the analyte gases within the porous layer, accompanied by a reduction of the built-in potential of the p-n junction, is responsible for the change in conductivity. Their initial studies also show a strong dependence of the device's response to processing of the PSi surface. It was found that oxidized (hydrophilic) porous silicon layers are relatively insensitive to organic vapors as compared to reduced (hydrophobic) porous silicon layers.

Angelucci et. al. have researched porous silicon membranes that are permeated with semiconducting oxides such as SnO_2. Their devices have shown 80-100% increases in current when exposed to 30 ppm of benzene and CO.[18] Furthermore, the porous devices have shown a sensitivity to humidity.

A thin (20 nm), continuous layer of gold was used as the top electrical contact to porous silicon in a device fabricated by Foucaran et. al.[19] The Schottky contacts showed a response to acetone and ethanol. Their results indicate that the thin gold layer on the porous silicon surface does not affect the adsorption of polar molecules. Like Angelucci's device, Foucaran's experiments indicate an irreversible response of the sensor to humidity.

The investigation of porous SiC devices has been more limited. Shields et. al.[20] investigated a PSiC sensor in the presence of hydrocarbons at 200-400 ^{o}C. This work was able to detect 0.5% methane and propane and rudimentarily discriminate between the two gases. Their contacts were made of chromium, and the I/V characteristics indicate fairly Schottky behavior of the contacts to the PSiC.
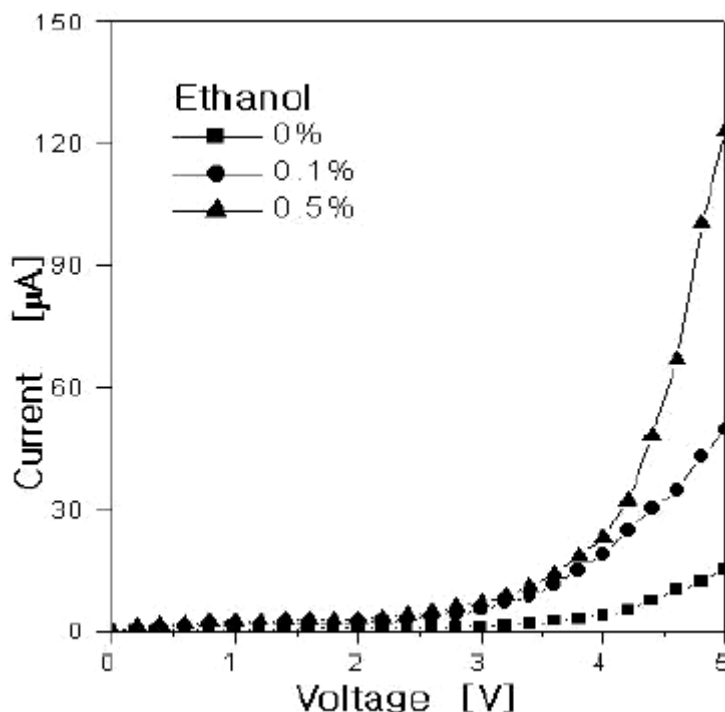
Figure 1.3.[17] I/V curves measured for ethanol in air exposed to a bare porous silicon film.

The sensing studies referenced above all indicate that PSiC sensors show promise as a suitable device for engine exhaust monitoring. If the high surface area of a PSiC film can be properly harnessed, porous semiconductor devices have the ability to provide high sensitivity at high temperatures and caustic environments where current sensors cannot operate. However, many unresolved issues remain. For example, all of the conductometric studies reported above utilized Schottky contacts to the porous network. Therefore, it is difficult to distinguish whether the changes in conductivity were due to interactions between the adsorbate gas and the porous skeleton, or due to reduction of the Schottky barrier height at the metal-semiconductor interface.

1.4 Outline of Work

Initially, this work investigated electroless etching of SiC to form PSiC. After discovering a suitable electroless etching technique for PSiC, this research progressed to measure the spectroscopic properties (cathodoluminescence, photoluminescence, and Raman scattering) of the porous material. Particularly, cathodoluminescence and photoluminescence were conducted to look for light emission from

7

the PSiC that was blue of the bandgap emission. Such emission could be indicative of nanocrystallite formation. Raman studies were conducted to further investigate quantum confinement effects in the nanoparticles.

After characterizing the PSiC formed with the electroless etchant, this work then proceeded to a study of the formation of PSiC by anodic etching under conditions similar to those reported in the literature. These samples served to enable a comparison of the spectroscopic properties between electrolessly etched and anodically etched PSiC, because the anodically etched pieces came from the same wafer as the PSiC etched with the electroless etchant. One highlight of this section of the research was the discovery of ultraviolet emission in cathodoluminescence. Anodic etching was also found to produce porous layers of a more reproducible and controllable thickness.

This work next proceeded to investigate the sensing capabilities of PSiC. The anodic etching process was fine tuned until PSiC films could be produced that yielded Fabry-Perot interference fringes in their reflectance spectra. Shifting of Fabry-Perot fringes due to changes in the dielectric constant of the film was sought to provide sensing capabilities complementary to conductometric measurements. The porous films were investigated for their optical sensing properties with several gaseous species at a range of elevated temperatures.

Finally, conductivity measurements were made on PSiC layers in a variety of gas atmospheres at elevated temperatures. One major hurdle during this phase of the work was the formation of ohmic contacts to the PSiC. Results from the conductivity test series were evaluated for their ability to produce an array of PSiC sensors able to identify and quantify a combination of gases within a range of elevated temperatures.

1.5 References

(1)   Gotz, W.; Schoner, A.; Pensl, G.; Suttrop, W.; Choyke, W. J.; Stein, R.; Leibenzeder, S. *J. Appl. Phys.* **1993**, *73*, 3332.

(2)   Shor, J. S.; Bemis, L.; Kurtz, A. D.; Grimberg, I.; Weiss, B. Z.; MacMillan, M. F.; Choyke, W. J. *J. Appl. Phys.* **1994**, *76*, 4045.

(3)   Ioffe Physico-Technical Institute, http://www.iioffe.rssi.ru/SVA/NSM/Semicond/Si/electric.html

(4)   Mehregany, M.; Zorman, C. A.; Rajan, N.; Wu, C. H. *Proc. IEEE* **1998**, *86*, 1594.

(5)   Hunter, G. W.; Chen, L.; Neudeck, P. G.; Knight, D.; Liu, C.; Wu, Q.; Zhou, H. *NASA Technical Memorandum 107444* **1997**.

(6)   Samman, A.; Gebremariam, S.; Rimai, L.; Zhang, X.; Hangas, J.; Auner, G. W. *J. Appl. Phys.* **2000**, *87*, 3101.

(7)   Serina, F.; Ng, K. Y. S.; Huang, C.; Auner, G. W.; Rimai, L.; Naik, R. *Appl. Phys. Lett.* **2001**, *79*, 3350.

(8)   Hunter, G. W.; Neudeck, P. G.; Gray, M.; Androjna, D.; Chen, L.; Hoffman, R. W.; Liu, C. C.; Wu, Q. H. *Mat. Sci. Forum* **2000**, *338-342*, 1439.

(9)   Uhlir, A. *Bell Syst. Tech. J.* **1956**, *35*, 333.

(10)   Curtis, C. L.; Doan, V. V.; Credo, G. M.; Sailor, M. J. *J. Electrochem. Soc.* **1993**, *140*, 3492.

(11)   Gao, J.; Gao, T.; Sailor, M. J. *Appl. Phys. Lett.* **2000**, *77*, 901.

(12)   Gao, J.; Gao, T.; Li, Y. Y.; Sailor, M. J. *Langmuir* **2002**, *18*, 2229.

(13)   Dancil, K. P. S.; Greiner, D. P.; Sailor, M. J. *J. Am. Chem. Soc.* **1999**, *121*, 7925.

(14)   Letant, S. E.; Sailor, M. J. *Adv. Mater.* **2000**, *12*, 355.

(15)   Snow, P. A.; Squire, E. K.; Russell, P. S. J.; Canham, L. T. *J. Appl. Phys.* **1999**, *86*, 1781.

(16)   Schechter, I.; Ben-Chorin, M.; Kux, A. *Anal. Chem* **1995**, *67*, 3727.

(17)   Kim, S. J.; Lee, S. H.; Lee, C. J. *J. Phys. D: Appl. Phys.* **2001**, *34*, 3505.

(18)   Angelucci, R.; Poggi, A.; Dori, L.; Tagliani, A.; Cardinali, G. C.; Corticelli, F.; Marisaldi, M. *J. Porous Mat.* **2000**, *7*, 197.

(19)   Foucaran, A.; Pascal-Delannoy, F.; Giani, A.; Sackda, A.; Combette, P.; Boyer, A. *Thin Solid Films* **1997**, *297*, 317.

(20)   Shields, V. B.; Ryan, M. A.; Williams, R. M.; Spencer, M. G.; Collins, D. M.; Zhang, D. *Inst. Phys. Conf. Ser.* **1996**, *142*, 1067.

CHAPTER 2

ETCHING AND MORPHOLOGY

2.1 Introduction

Due to their unique morphological and optical properties, porous semiconductors are candidates for several varied applications. For example, porous semiconductors have been investigated as compliant substrates for epitaxial growth.[1-6] Some research indicates that epitaxial layers grown on top of porous substrates may lead to fewer defects as well as strain relaxation.[2] In addition, because of their inherent high surface-to-volume ratios, porous semiconductors are attractive candidates for chemical[7-11] or physical (temperature, pressure, flow)[12] sensing. The suitability of porous semiconductors as epitaxial substrates or sensors is highly dependent upon the porous nanostructure.

The literature documents several early variations of forming porous semiconductors that eventually lead to the aqueous anodic methods commonly used today. PSi has been formed with anhydrous etchants such as HF/acetonitrile mixtures.[13,14] Also, stain etching of Si to form thin PSiC layers utilizes Al films in the presence of an aqueous HF/HNO_3 etching solution.[15] Electroless etching of GaN has been demonstrated using $K_2S_2O_8/KOH$ etching solutions.[16] Finally, as a forbearer to current PSiC production, Shor et. al. conducted a series of experiments investigating the use of photoelectrochemical etching of SiC in the hope of finding faster, smoother, and more selective bulk etching processes.[17-20]

Semiconductors, such as silicon and gallium nitride, can easily be made porous via wet etching techniques (both electrochemical and more recently metal-assisted electroless etching techniques[21-24]), and a variety of porous morphologies can be formed. In silicon, the morphology is highly dependent upon the etching conditions. In gallium nitride, the etching conditions have significant impact on the resulting morphology, but the porous structure is also highly dependent upon the particular properties of the wafer (doping, defect density, etc.), since the material quality of available gallium nitride does not approach that of commercially available single crystal silicon. Morphologies of porous materials range

from sponge-like networks of pores to very regular arrays of long columnar nanocrystals/pores oriented perpendicular to the semiconductor free surface. Regardless of the morphology, though, all porous semiconductors are characterized by a high surface area.

Currently available anodic etching techniques produce PSiC of varying morphology and properties.[25-45] The results reported in the literature detail specific changes in morphological and spectroscopic properties upon formation of a porous nanostructure in SiC; however, wide discrepancies often exist in the properties measured by independent researchers. As a result, definitive conclusions about the causes of spectroscopic phenomena in PSiC are difficult to determine. In addition, the need for electrical contacts in the anodization process is a limitation on the large-scale production of PSiC. The development of an electroless wet etching chemistry could permit large areas of homogeneous PSiC to be produced, and the electroless technique is better suited for small or odd shaped piece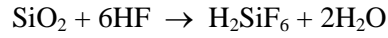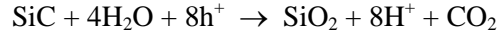s. Electroless etching also offers the advantage of masking areas to remain unetched. Finally, electroless etching has shown the ability to produce PSi with tunable optical properties.[24]

The electroless etching of Si and GaN is made possible by using ultrathin ($d < 10$ nm) films of Pt metal to catalyze the reduction of a chemical oxidant in the presence of HF, which combined with UV illumination injects holes into the valence band, the holes subsequently participating in the oxidation and dissolution of the substrate. H_2O_2 is used as the oxidant for Si and GaN. However, although H_2O_2 produces PSiC anodically, preliminary research showed that SiC etches very inefficiently in HF:H_2O_2 etchant without anodization (even in the presence of Pt catalyst). The more active oxidant potassium persulfate, $K_2S_2O_8$, is required for the efficient electroless production of PSiC. $K_2S_2O_8$ in the presence of Pt and illumination is competent to inject holes into the valence band of SiC. The holes may then travel laterally and participate in etching reactions in a manner similar to that observed in PGaN.[16] One hypothesis is that SiC is oxidized in an 8e$^-$ process analogous to the electroless etching of PSi and PGaN, the products subsequently reacting with HF to produce a soluble product according to:
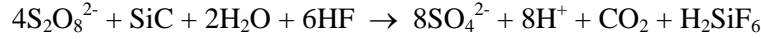
Cathode (Pt):

$$4S_2O_8^{2-} + h\nu \rightarrow 8SO_4^{2-} + 8h^+$$

Anode (SiC):

$$SiC + 4H_2O + 8h^+ \rightarrow SiO_2 + 8H^+ + CO_2$$

$$SiO_2 + 6HF \rightarrow H_2SiF_6 + 2H_2O$$

Overall:

$$4S_2O_8^{2-} + SiC + 2H_2O + 6HF \rightarrow 8SO_4^{2-} + 8H^+ + CO_2 + H_2SiF_6$$
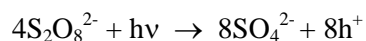
It is also possible that the ultraviolet irradiation utilized during etching is creating a short-lived diffusible oxidant species (a free radical form of SO_x, for example) that participates in the etching process; no mechanistic studies have been investigated in this work to verify the exact reaction mechanism.

Silicon carbide forms over 250 different polytypes. Polytype refers to the stacking sequences within the crystalline material. The polytypes of silicon carbide generally fall into three primary categories: cubic, hexagonal, and rhombohedral. The cubic form of SiC, 3C- or β-SiC, is face-centered cubic with alternating layers of carbon and silicon atoms in the [111] direction. However, this polytype is difficult to crystallize and was not used in this research. Rather, two forms of hexagonal SiC were used exclusively. Most work was conducted with 6H-SiC, which has alternating layers of silicon and carbon in the sequence ABCACBABCACB… along the c-axis of the hexagonal cell. Limited work was also conducted with the 4H-SiC polytype, which has alternating layers of silicon and carbon in the sequence ABACABAC… along the c-axis of the hexagonal cell.

The etching reaction proposed above does not explicitly indicate that Pt must be deposited onto the SiC surface in order for electroless etching to proceed. However, Pt catalyzes the reduction of the oxidant (in our case, $S_2O_8^{2-}$) and acts as a local cathode site for hole injection into the semiconductor (Fig. 2.1). In addition to the Pt catalyst, UV illumination is also necessary during electroless etching. The energy of the holes available from $S_2O_8^{2-}$ reduction is not sufficient to accomplish direct injection of holes into the valence band of SiC.[46,47] Fig. 2.2 shows the energy of the $S_2O_8^{2-}/SO_4^{2-}$ couple on the absolute scale referenced to the work function of Pt.[46,47] Clearly holes generated through this oxidation process do not possess sufficient energy to access the SiC valence band directly.

2.2 Experimental Methods

2.2.1 Etching Techniques

2.2.1.1 Electroless Etching Technique

Silicon carbide wafers were obtained from Cree and included a 6H n-type wafer ($\rho = 0.086\ \Omega$ cm), a 4H n-type wafer ($\rho = 0.067\ \Omega$ cm), and a 4H p-type wafer ($4.4 \times 10^{17}\ cm^{-3}$). Both n-doped wafers were cut on axis to expose the (0001) Si plane; the p-type wafer was cut 8° off the c-axis. The two n-doped wafers were polished on the silicon side only; the p-type wafer was double polished. Initial cleaning of the wafers consisted of consecutive 5-min dips in water, acetone, and methanol before sputter deposition of the Pt catalyst. Pt was sputter coated onto the SiC wafers using a Desk II TSC Turbo Sputter Coater (Denton Vacuum) through a physical mask to produce small (500 μm in diameter, 1.5 mm center-to-center) circles of 10 nm mass thickness.

Initially, wet etching was attempted with $CH_3OH:HF:H_2O_2$ (1:2:1 by volume of pure methanol, 49% HF, and 30% H_2O_2), since this etchant is known to etch both Si and GaN electrolessly.[21-24] However, this etchant produced only a small degree of pitting in SiC (Fig 2.3). Previous work conducted in our laboratory[23] has shown that careful precleaning of the GaN surface is required in order to produce porous morphology consistently. Therefore, a more aggressive precleaning (nitric acid) of the SiC samples was conducted; however, the same sparse pitting resulted from exposure to the $CH_3OH:HF:H_2O_2$ etchant. Next, an etchant composed of 0.1M $K_2S_2O_8$:0.08M KOH was attempted, since this etchant had been shown to electrolessly etch GaN.[16] This etchant produced SiC with a rougher surface (Fig. 2.4); however, the morphology was not porous and did not extend beyond the top surface of the SiC wafer.

The working hypothesis at this point in time was that the etching reaction needed to be initiated, since it was known that the $CH_3OH:HF:H_2O_2$ etchant can produce PSiC porous when SiC is used as a substrate below an etched GaN layer (Fig. 2.5).[48] Therefore, the surface of the SiC wafer was roughened with a scribe prior to immersion in $CH_3OH:HF:H_2O_2$ in order to produce initiation sites for etching. However, SiC prepared in this manner did not exhibit porosity either.
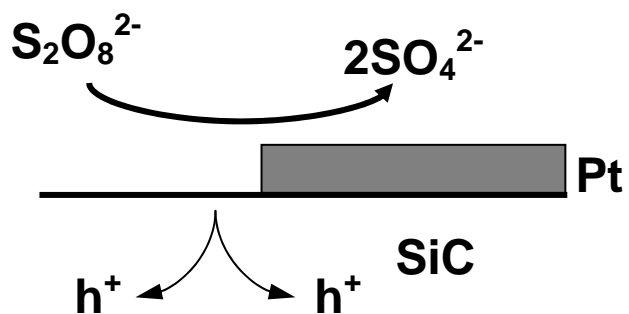
Figure 2.1. Schematic diagram of the reduction of persulfate ion accompanied by hole injection into the SiC wafer at the Pt catalyst deposited on the surface.
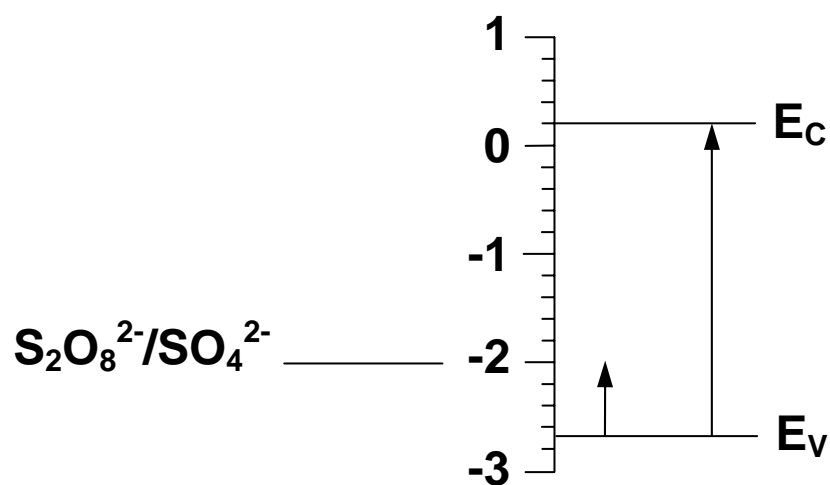
Figure 2.2.[46,47] Scale showing the reduction potential of the persulfate ion in relation to the conduction and valence bands of crystalline SiC on the absolute electrochemical energy scale.
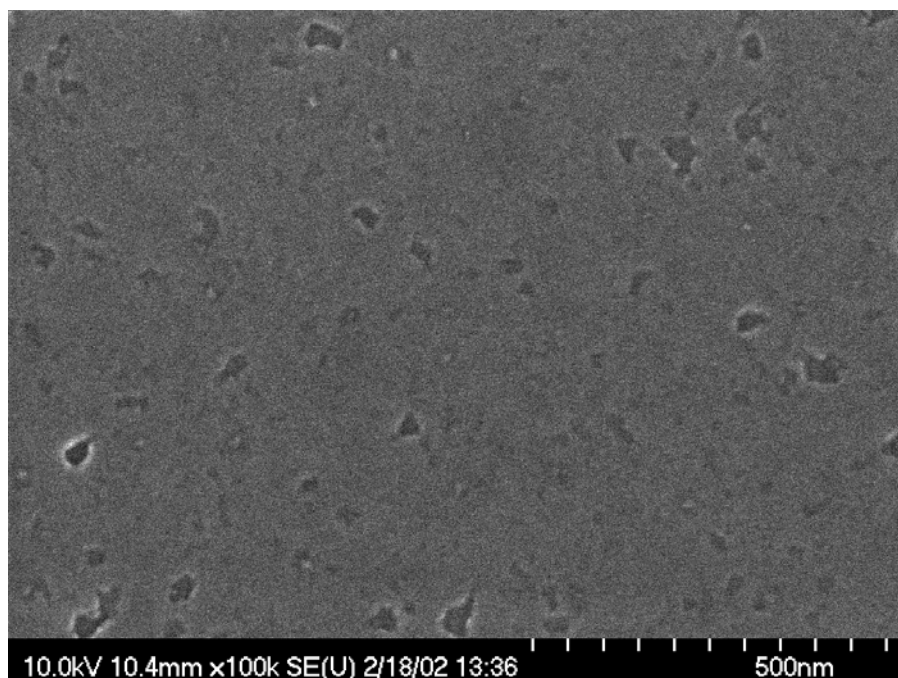
Figure 2.3. Plan view SEM image of the relatively sparse etch pits resulting from electroless etching of SiC in CH_3OH:HF:H_2O_2 etchant.
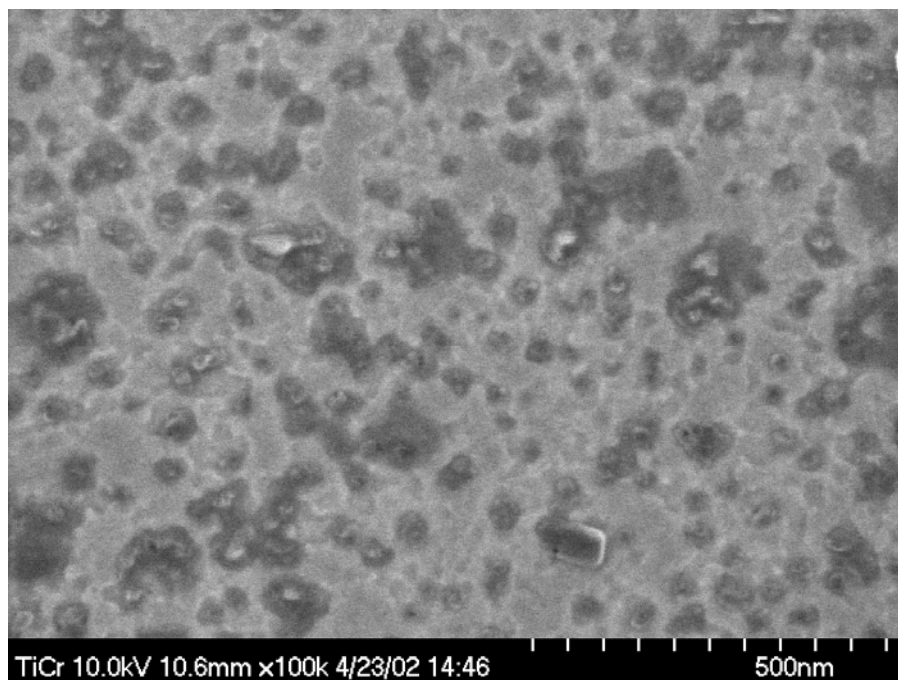
Figure 2.4. Plan view SEM image of the roughened SiC wafer surface after exposure to the 0.1M $K_2S_2O_8$:0.08M KOH etchant.

120201e 15.0kV 11.1mm x100k SE(M) 12/4/01   500nm
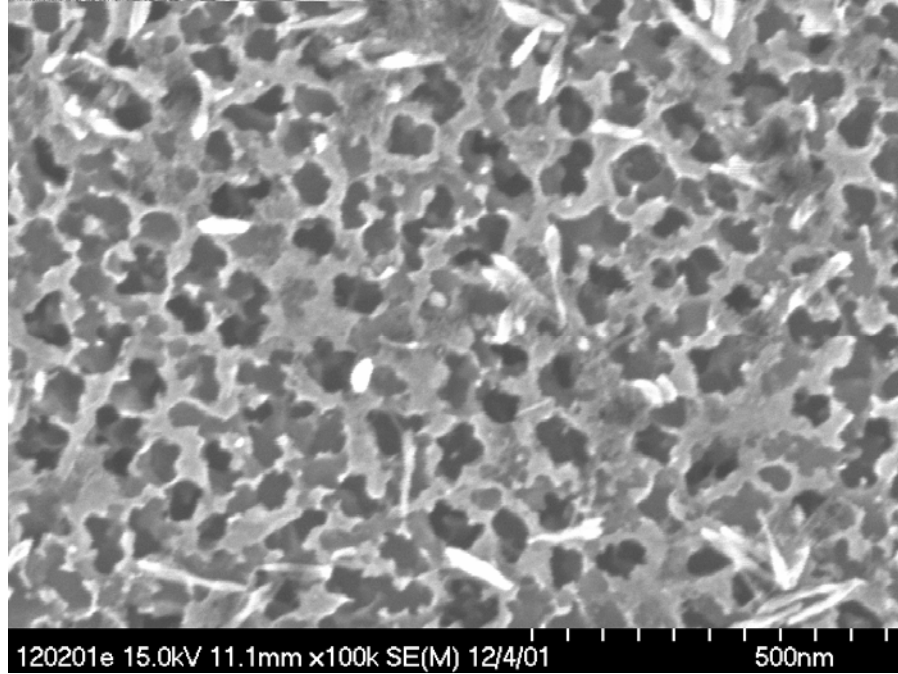
Figure 2.5.[48] Plan view SEM image of PSiC formed when an epilayer of GaN grown on a SiC substrate was entirely etched away with the $CH_3OH:HF:H_2O_2$ etchant.

In these initial experiments, even though a great majority of the surface remained planar and unetched, extensive porosity in the immediate vicinity (within 500 nm) of micropipes was often observed (Figs. 2.6 and 2.7), indicating a possible relationship between crystalline quality and porous morphology. One hypothesis is that the porous structure in the vicinity of micropipes is due to dislocations terminating at the free surface, since these micropipes obviously interfere with the short-range order of the lattice structure.

Some researchers have noted the formation of a "skin layer" on the surface of porous SiC during anodic etching.[25,32,34,37,49,50] The top thin skin layer remains primarily crystalline, with relatively few pits extending to the free surface of the wafer. This skin layer is approximately 20-50 nm thick, and it covers a fully porous morphology that extends deeper within the wafer. Therefore, several of the electrolessly etched SiC samples were reactive ion etched (RIE) to remove any potential skin layer. RIE was conducted at a power density of 0.8 W/cm^2 and with 20 sccm flow of SF_6 through the reactor; the total pressure in the reactor was 20 mtorr (maintained by argon). Etching times ranged from 2 to 6 min. These
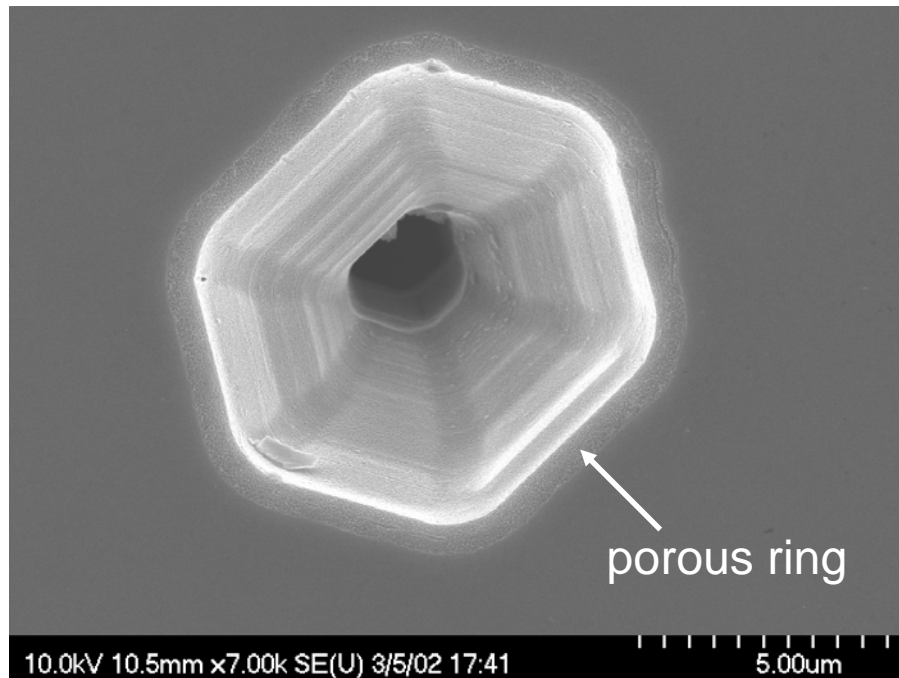
Figure 2.6. SEM image of a micropipe on the SiC wafer surface after exposure to the $CH_3OH:HF:H_2O_2$ etchant. Notice the porous ring extending approximately 1 μm laterally from the periphery of the micropipe.
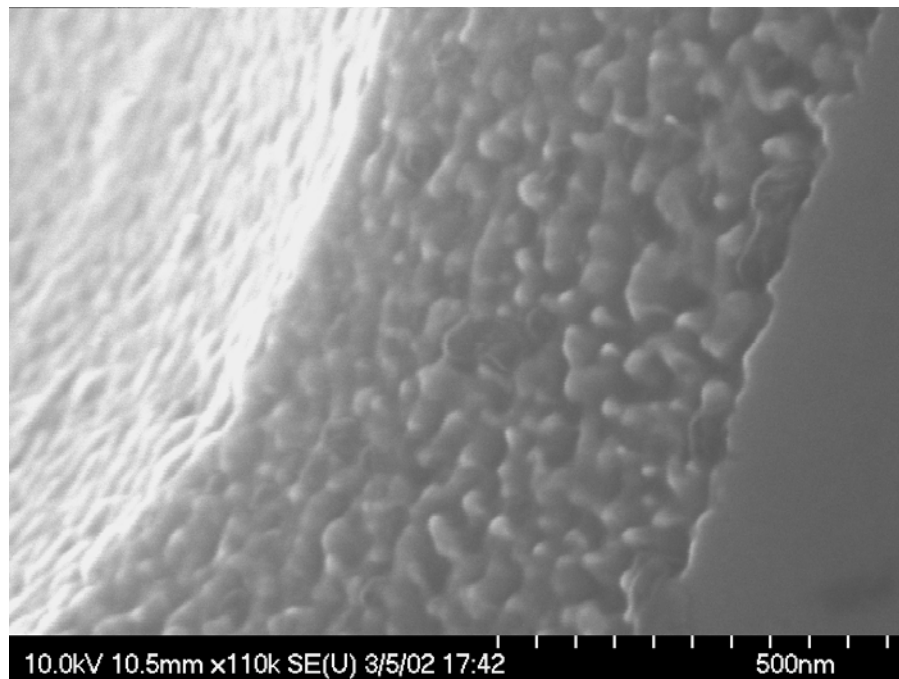
Figure 2.7. Close-up SEM image of the porous microstructure around the periphery of a micropipe that has been exposed to the $CH_3OH:HF:H_2O_2$ etchant.

conditions were selected to remove approximately 100 nm of material from the surface of the SiC wafer.[37,51] However, RIE revealed no definable submerged porosity, although the RIE results were hard to interpret definitively, because the RIE damage to crystalline material (Fig. 2.8) produced a morphology very similar to that in porous material. All of the samples exposed to RIE looked like the normal RIE damage shown in Fig. 2.8, with the exception of one sample (Fig. 2.9). However, it is believed that anomalies in the reactive ion etching produced the structure seen in Fig. 2.9, and that no submerged porosity existed in this wafer either.

Oxidation has also been cited in the literature as a method of exposing submerged porosity.[25,26] Several of the samples in this work were therefore oxidized (both before and after RIE). Oxidation was carried out with steam (in O_2) flowing at 5 L/min within a tube furnace maintained at 1150 ^{o}C; the oxidation time was typically 1 hr. However, there was no evidence of any submerged porosity after oxidation and a dip in HF. Finally, several techniques of cycling RIE, oxidation, and electroless etching were conducted in an attempt to initiate the etching process. None of these techniques were successful in producing extensive porosity, however.

Eventually, an etchant composed of HF and $K_2S_2O_8$ was tested. This etchant was investigated simply to combine the effects of the acid attack of SiO_2 by HF with $K_2S_2O_8$, which is a slightly stronger oxidizer than H_2O_2. This etchant proved the most successful and was used for the remainder of the electroless etching work. $S_2O_8^{2-}$ ($E^0 = -2.05$ V) has a very similar standard reduction potential to H_2O_2 ($E^0 = -1.776$ V), and one would not expect them to behave much differently as etchants on thermodynamic grounds. We are still not certain what gives rise to the significantly stronger etch behavior of $S_2O_8^{2-}$ relative to H_2O_2.

Once $S_2O_8^{2-}$ was identified as a suitable oxidant, two different concentrations of wet etchants were tested: (a) concentrated HF etchant, consisting of 14M HF (semiconductor grade, Transene Inc.) and 0.075M $K_2S_2O_8$ (Fisher Scientific); and (b) dilute HF etchant, consisting of 0.50M HF and 0.15M $K_2S_2O_8$ (the solubility limit of $K_2S_2O_8$ at room temperature). Tests were done with methanol in the etchant to lower surface tension and prevent the formation of bubbles on the SiC surface during etching. However,
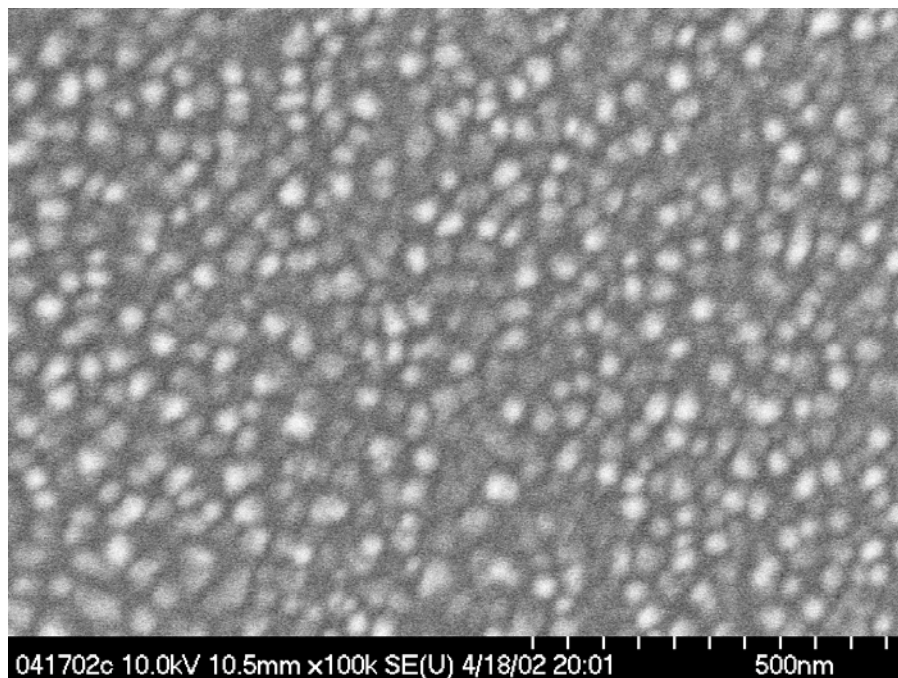
Figure 2.8. Plan view SEM image of a previously-unetched crystalline SiC wafer that has been etched via reactive ion etching using the conditions described in the text.
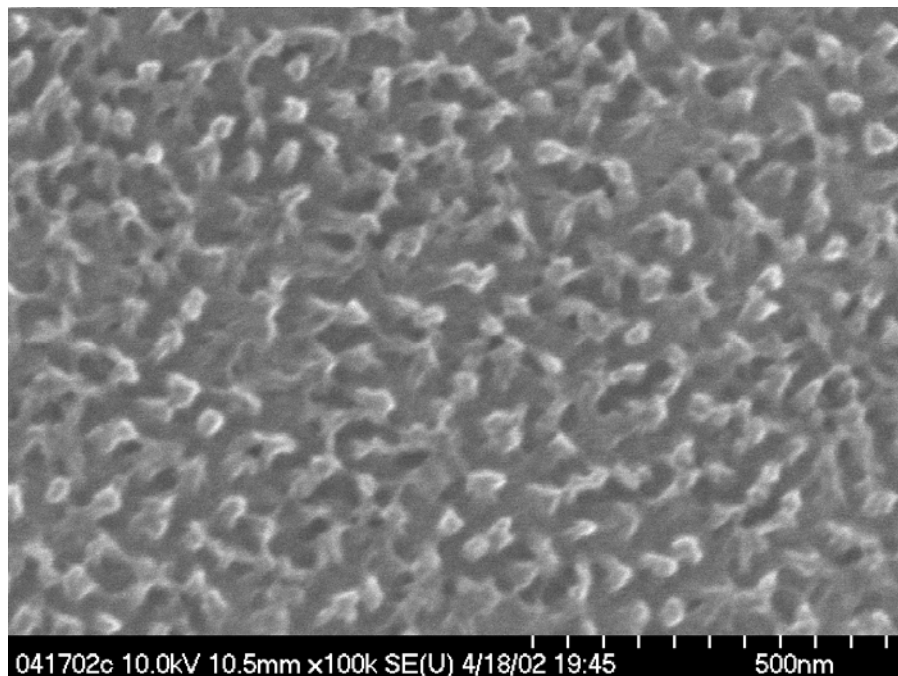
Figure 2.9. Plan view SEM image of SiC that has been exposed to the $CH_3OH:HF:H_2O_2$ etchant for 60 min, followed by reactive ion etching using the conditions described in the text. The wafer had shown only sparse etch pits on the surface after electroless etching.

methanol did not help the etching process; in fact, SiC did not etch with substantial methanol added to the etchant.

Etch times varied from 10 to 60 min. Ultraviolet irradiation was obtained from a Hg arc-lamp (Oriel Instruments Model 6281). The arc-lamp emission supplied for the duration of the etching at a distance of 10 cm was short-pass filtered to expose the wafer to 32 mW/cm^2 at $\lambda < 360$ nm. At the conclusion of etching, a rinse of 5 min each in water and methanol (2x) was conducted before air drying the porous samples.

2.2.1.2 Anodic Etching Technique

The same wafers and pre-cleaning procedures were used for anodic etching of SiC, with the exception that the Pt pattern, deposited onto the SiC wafers prior to electroless etching, was eliminated. Rather, to prepare the SiC pieces to undergo anodic etching, a corner of the wafer (~2 x 2 mm) was coated with 20 nm mass thickness of Pt for electrical contact with the etching probe.

The SiC was placed into a Teflon electrochemical cell, along with a Pt wire counter electrode and a saturated calomel reference electrode (Fig. 2.10). Dilute HF (5%) was employed as the etching solution. The SiC sample to be etched was illuminated by UV light (15 mW/cm^2 at $\lambda < 365$ nm) for the duration of the etching (usually 40 min). Upon the conclusion of etching, a rinse of 5 min each in water and methanol (2x) was conducted before air drying the porous samples.

2.2.2 Scanning Electron Microscopy

Scanning electron microscope (SEM) images were collected using a high-resolution field emission SEM (Hitachi S4700) using accelerating voltages of 10-15 keV.

2.2.3 BET Isotherms

Surface area measurements were conducted in order to further characterize the porous structure, as well as evaluate the suitability of the porous layers to serve as chemical sensors. One method of measuring the surface area of porous materials uses the method developed by Brunauer, Emmet, and Teller. BET isotherms are collected by adsorbing nitrogen to the surface of the sample material. Surface

area measurements were obtained at liquid nitrogen temperature using an ASAP 2400 apparatus

(Micromeritics). Each sample was outgassed for 24 hours at 150 $^{\circ}$C prior to analysis.
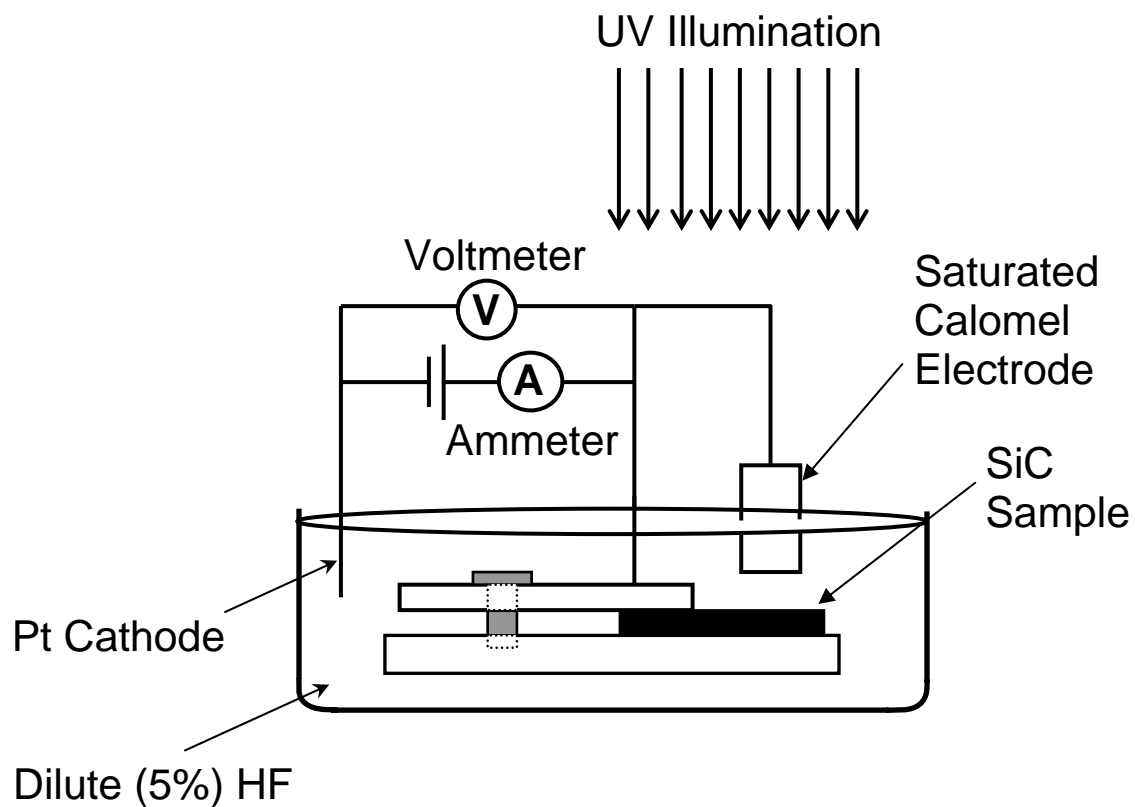
Figure 2.10. Diagram of the etching apparatus used to etch SiC wafers anodically.

2.3 Results and Discussion

2.3.1 Electrolessly Etched SiC

2.3.1.1 n-doped 6H-SiC

SEM analysis indicates that etch times ranging from 10 to 60 min yield a progression of PSiC morphologies. In general, for both the concentrated and dilute HF etchants, etch times less than approximately 30 min yield a ridged porous structure, as shown in Fig. 2.11. The porous morphology is homogeneous across the entire wafer surface, although occasional pockets of varying degrees of porosity are observed. The cause of the pockets of relatively unetched regions is unknown at this time. These isolated patches of lightly etched SiC do not occur consistently at a specific distance away from the Pt circles. The relatively unetched regions could result from regions of low dislocation density at the surface of the wafer. Or, it is possible that the wet etchant simply did not have good access to these small regions of the wafer, possibly due to the formation of bubbles during the etching process.

Often, wafers etched for these relatively short amounts of time were actually more porous directly between the Pt dots, rather than at the Pt dot edge. This is an unexpected result given the theory of hole injection occurring at the Pt cathode. It seems unlikely that hole injection occurs at the Pt, and then the holes are transported macroscopic (mm) distances away to produce etching. However, Pt is necessary for etching, as several experiments were conducted without Pt, and no PSiC was ever observed in the absence of Pt.

Longer etch times (~60 min) yield different morphologies depending upon the etchant used. When using the concentrated HF etchant, porosity restricted to the near-surface region is obtained (Fig. 2.12). However, when using the dilute HF etchant at longer etch times a spongelike morphology results (Fig. 2.13). One key difference between the morphologies obtained at short and long times appears in the lateral etching. At shorter etch times the etching occurs inhomogeneously in the plane, but is largely directed perpendicular to the original surface. At longer times the etching develops more lateral structure with etching proceeding to undercut some of the structures confined to the surface.
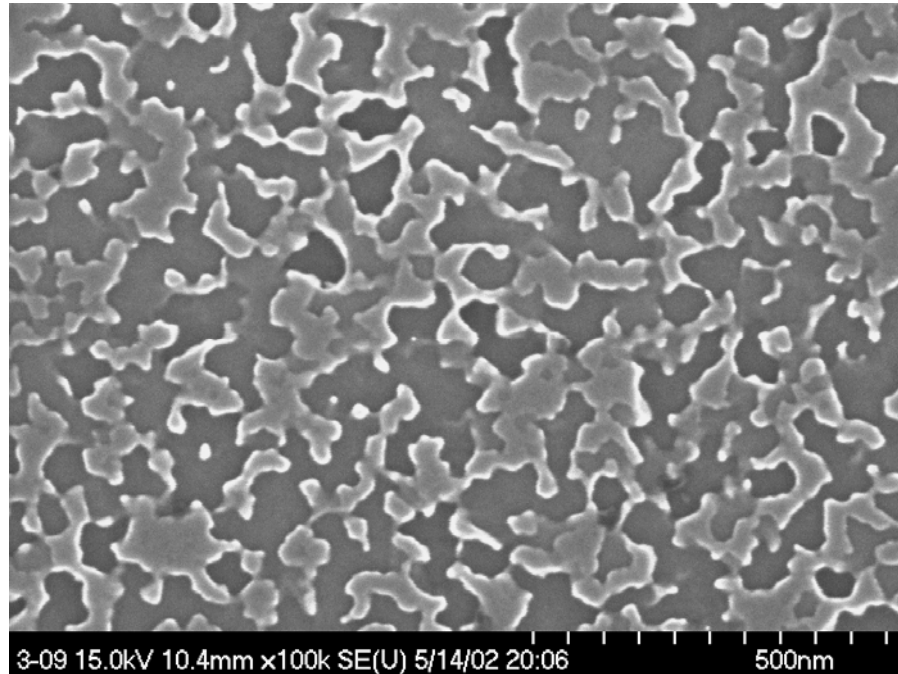
Figure 2.11. Plan view SEM image of PSiC prepared from n-type 6H-SiC by electroless etching in concentrated HF etchant for 20 min.
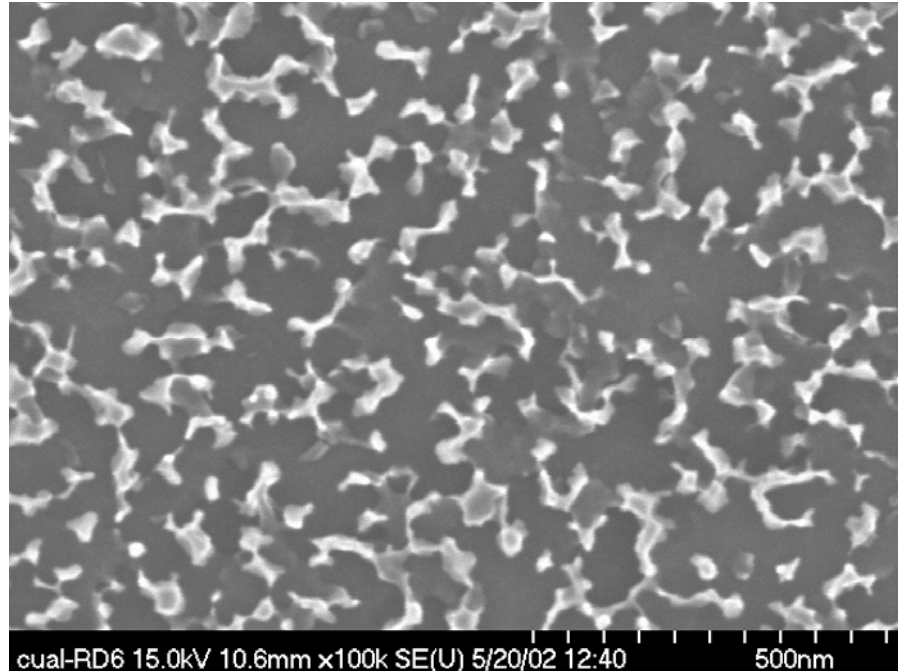
Figure 2.12. Plan view SEM image of PSiC prepared from n-type 6H-SiC by electroless etching in concentrated HF etchant for 60 min.
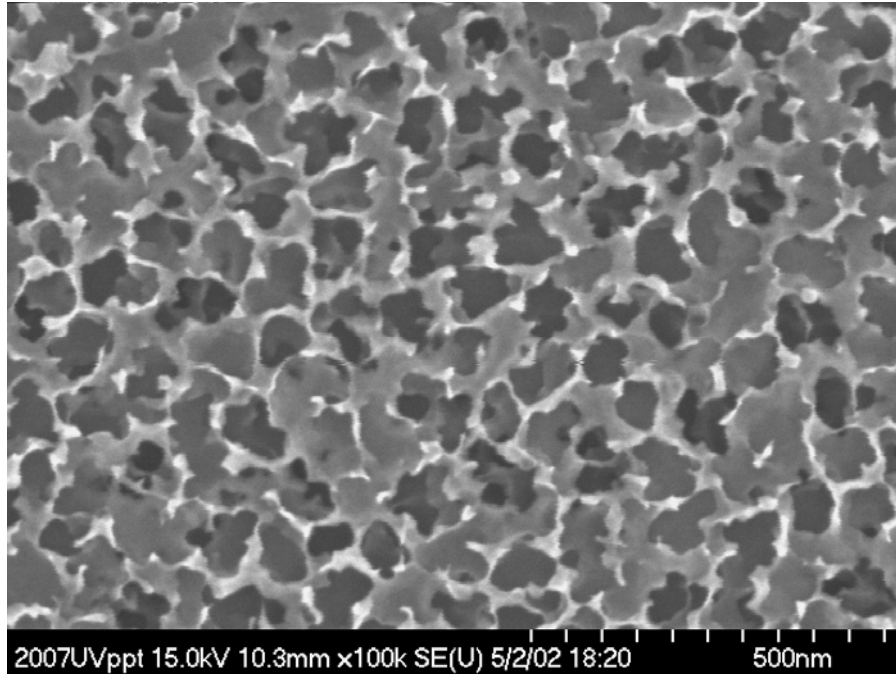
Figure 2.13. Plan view SEM image of PSiC prepared from n-type 6H-SiC by electroless etching in dilute HF etchant for 60 min.

Numerous porous wafers were cleaved and examined in cross-section to determine the internal depth of the porous structure. Despite the depth of the porous layer reasonably clean cleaves could be obtained. As shown in Fig. 2.14, a uniformly porous layer can be formed deep into the bulk of the wafer, extending > 100 μm in especially long etches. Furthermore, the porous structure extends all the way to the free surface of the wafer, without the formation of a skin layer reported in anodic etching experiments (Fig 2.15). All of the porous materials had the pattern of networked spherical or triangular pores/nanocrystallites as shown in Fig. 2.15; cylindrical nanocrystallites/pores were never formed. For the deeply porous layers, average nanocrystallite sizes on the order of 25-50 nm diameter were obtained.

The porous SiC to crystalline SiC interface took on several forms when examined in cross-section; occasionally multiple forms of porosity termination were witnessed in just one piece of porous SiC. First, relatively infrequently porosity stops abruptly (at least to the viewer of the exposed fracture plane) (Fig. 2.16). Second, the porosity can end at a front interspersed with relatively large pits (Fig.

24

2.17). Finally, the porous structure can just gradually become smoother until the broken cross section becomes planar (Fig. 2.18).

The formation of deep porous structure is striking, because reactants (HF) need to be transported to the evolving etch sites, and products need to be transported away. The postulated formation of CO_2 as an oxidation product undoubtedly impacts the transport process. More importantly the interconnected nature of the deep porous structures provides multiples paths for the transport of reactive species to the active etch front and for transport of products away. In PGaN where the pores are largely columnar, deep structures are difficult to obtain. Thus, it is quite likely that the lateral connections between pores facilitate transport and make the attainment of deep porosity possible.

Another conspicuous feature of the electroless etching of PSiC is the lateral extent of etching. PSiC is formed adjacent to, and as much as millimeters away from, the edges of the Pt coated areas. Fig. 2.19 illustrates the difference in etching behavior between the region covered by Pt and the areas adjacent to it. In this sample, after formation of PSiC, the Pt was removed with aqua regia, and a sharp interface (±50 nm) is revealed. In the region adjacent to the Pt porosity exists both at the surface and below the surface. In the region covered by Pt during etching, no surface porosity is observed, although the modulated light and dark areas in the SEM micrograph are a clear sign that some of the subsurface pores extend laterally under the edge of the Pt coated region. These results indicate that the Pt, in addition to serving as a catalyst, can be used as a mask to direct the formation of surface porosity patterns. Other experiments were conducted in which a continuous 10 nm thick sheet of Pt was deposited onto the back (unpolished) side of the SiC wafer prior to etching. This protocol resulted in porosity on the front (polished) side of the wafer, but the porosity was restricted to a shallow surface layer.

Unfortunately, the etch rate (depth of etch) was inconsistent from sample to sample. As shown in Fig. 2.14, deep porous structures could be formed in some samples. However, in many samples, etching/porosity was limited to the top 50 nm at the surface, regardless of how long the sample was exposed to the etchant (Fig. 2.20). For this reason, using currently available commercial SiC wafers, electroless etching does not result in the reproducible morphology necessary to mass produce PSiC films.

25
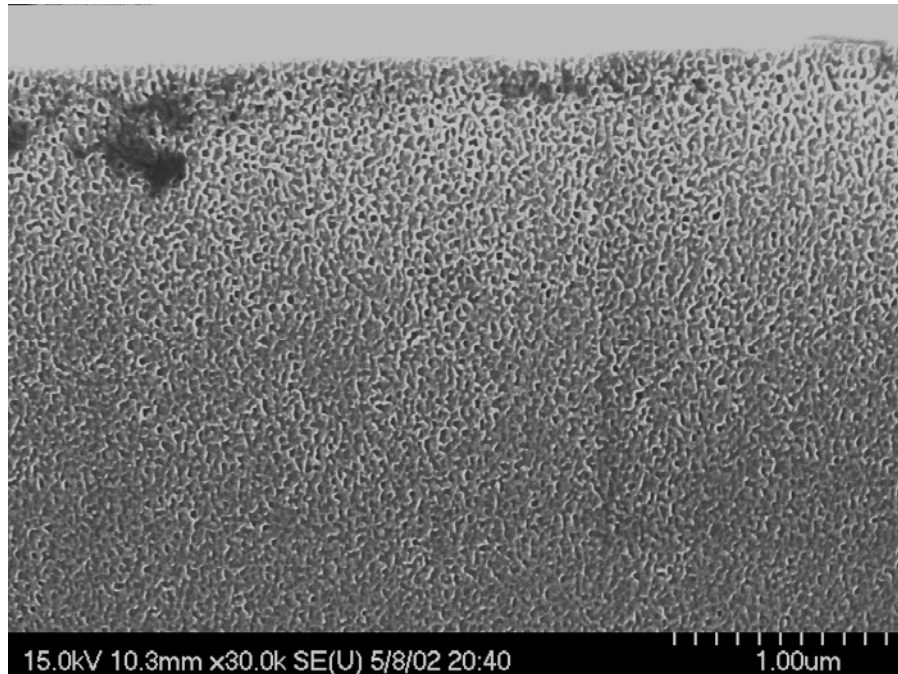
Figure 2.14. Cross-sectional SEM image of PSiC prepared from n-type 6H-SiC by electroless etching in dilute HF etchant for 60 min. Note the uniformity of the etched morphology throughout the depth of the etched region.

Figure 2.15. Cross-sectional SEM image of PSiC prepared from n-type 6H-SiC by electroless etching in dilute HF etchant for 60 min.
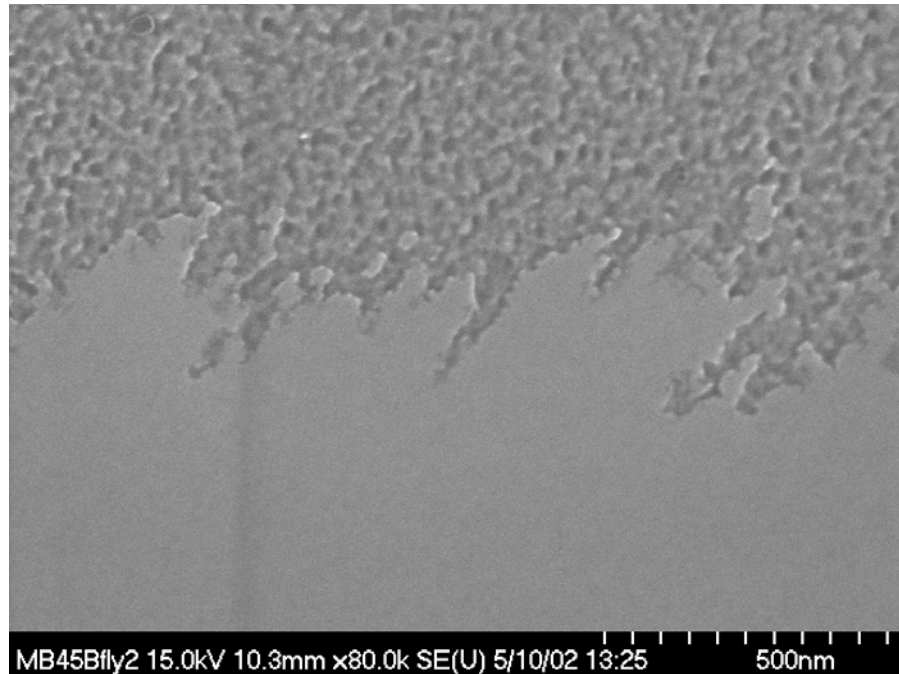
Figure 2.16. Cross-sectional SEM image of the abrupt termination of porosity at the PSiC/SiC interface.
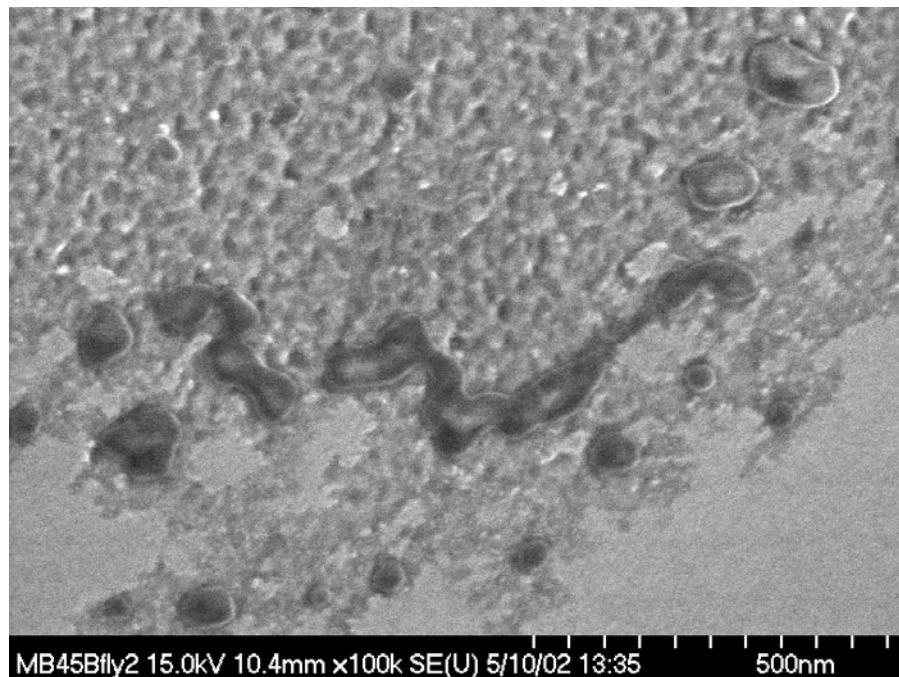
Figure 2.17. Cross-sectional SEM image of the PSiC/SiC interface that is marked by the presence of large etch pits.
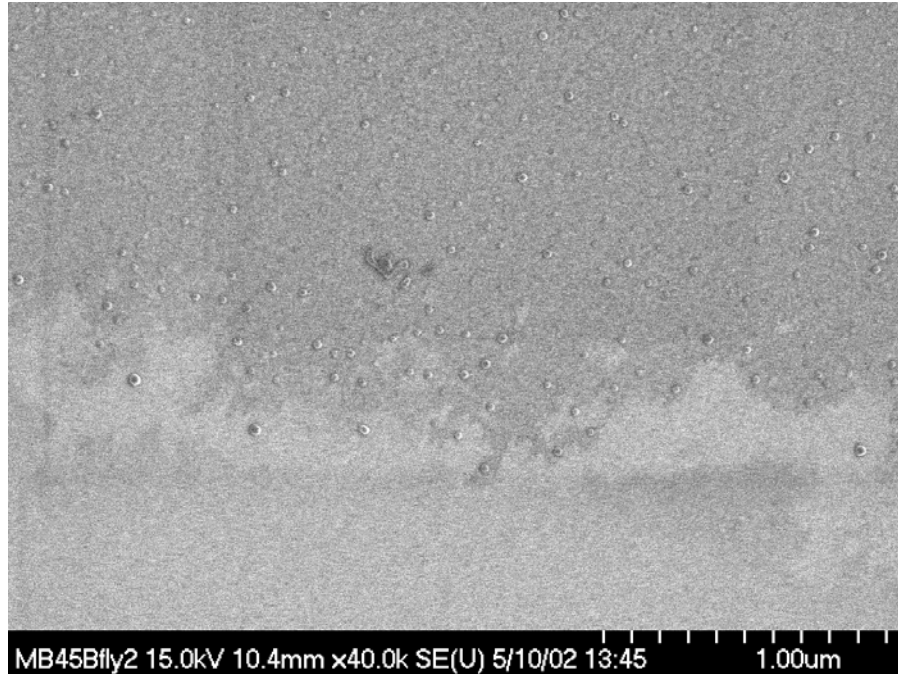
Figure 2.18. Cross-sectional SEM image of a gradual transition between PSiC and unetched SiC; no definable interface of porosity is discernable.

Figure 2.19. Plan view SEM image of PSiC prepared from n-type 6H-SiC by electroless etching in dilute HF etchant for 60 min. The image is obtained near the edge of a Pt-covered region, but after removal of the Pt.
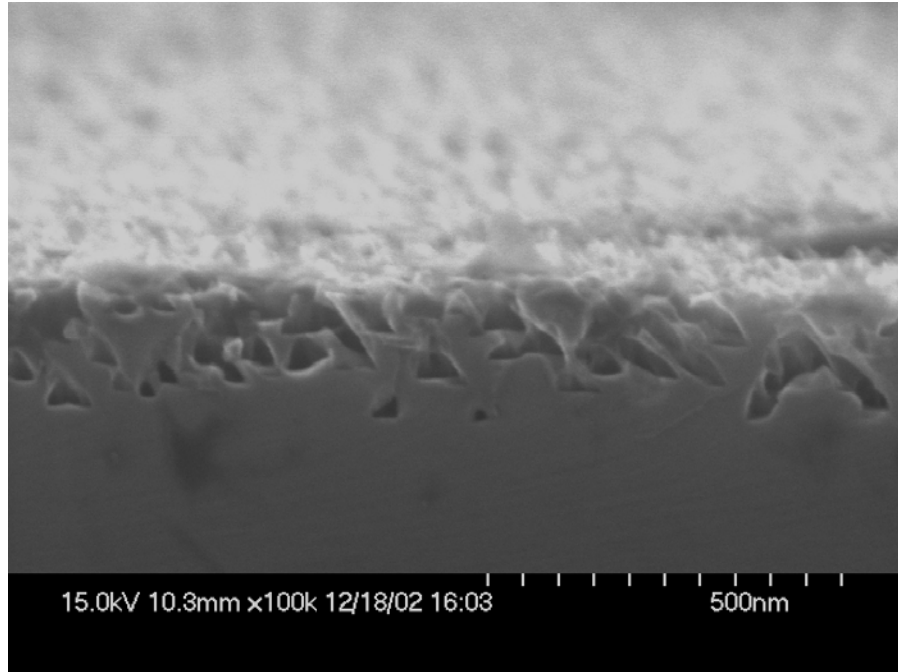
Figure 2.20. Cross-sectional SEM image of PSiC prepared from n-type 6H-SiC by electroless etching in dilute HF etchant for 60 min. Despite the long etch time, only a surface layer of pores are observed.

High resolution X-ray diffraction (HXRD) studies were conducted in order to determine if some feature of crystallographic quality (particularly defects) could be responsible for the inconsistencies in etch depth. HXRD studies can reveal changes in lattice constant, defect density, and impurities ($> 1\%$) for the typical X-ray sampling depth of ~25 μm. The results of the HXRD study of the porous samples were inconclusive. The unetched 6H-SiC wafer was found to have higher defect densities at the edges of the wafer, which is a normal result of crystal growth. Upon electroless etching, plan view SEM images indicated that samples from the edges of the SiC wafer did become more porous than samples from the central regions of the SiC wafer. However, upon cleaving the samples, cross-section analysis showed that none of the pieces examined in this test series exhibited submerged porosity.

The HXRD test series also showed a change in the lattice constant of the SiC after etching. The porous, etched material exhibited a variation of c-direction lattice spacing between the value for the unetched material (15.08 Å) and a 0.06% contraction of the lattice parameter (Fig. 2.21). The change in lattice parameter is similar to the behavior of etched PSi, where lattice parameter also changes upon

29

etching. Interestingly, though, in PSi the lattice parameter expands upon the formation of pores,[52-56] while our results indicate a small lattice contraction in PSiC. This contraction of the lattice parameter leads to tensile stress within the porous layer. This residual stress can affect the Raman spectra of these porous layers, and so this effect must be accounted for when analyzing the Raman data presented in Chapter 3.

2.3.1.2   n-doped 4H-SiC

The 4H polytype of SiC yields a distinctly different morphology than 6H material when exposed to the same electroless etching conditions. The resulting morphologies are independent of the concentration of etchants used. For short (~20 min) etch times a ridged porous structure similar to the 6H polytype is obtained in 4H wafers (similar to that shown in Fig. 2.11). For longer etch times (~60 min), different pieces of the 4H wafer yield different morphologies, from a cellular surface exhibiting nanofingers (Fig. 2.22) to highly porous spongelike structures (Fig. 2.23). One possible explanation for the variation in morphology observed when etching 4H material under nominally identical conditions arises from the observation that the 4H wafer studied contained at least some regions of 6H material as determined by Raman mapping experiments (see Chapter 3). It is reasonable to hypothesize that variations in etched morphology between different 4H-SiC samples arise from variations in the polytype distributions of the nominal 4H starting material. The principal difference between electroless etching of 4H and 6H wafers, however, is the consistent confinement of the porous structure to the near-surface region in 4H material. At most a surface layer of pores a few hundred nm deep is obtained in 4H material (Fig. 2.24).

Occasionally samples that contained both the 4H and 6H polytypes at the surface were etched. It was found that at the completion of etching, only the 4H regions had etched and become porous; the 6H regions remained planar and unetched (Fig. 2.25). This is an unexpected result, given the ability of pure 6H-SiC to etch much more completely than the apparently "pure" 4H-SiC pieces. In many regions the 4H/6H boundary was marked with relatively large micropipes (Fig. 2.26). In addition, in cross-section, the 4H polytype was detected to undercut the 6H polytype within the wafer (Fig. 2.27).
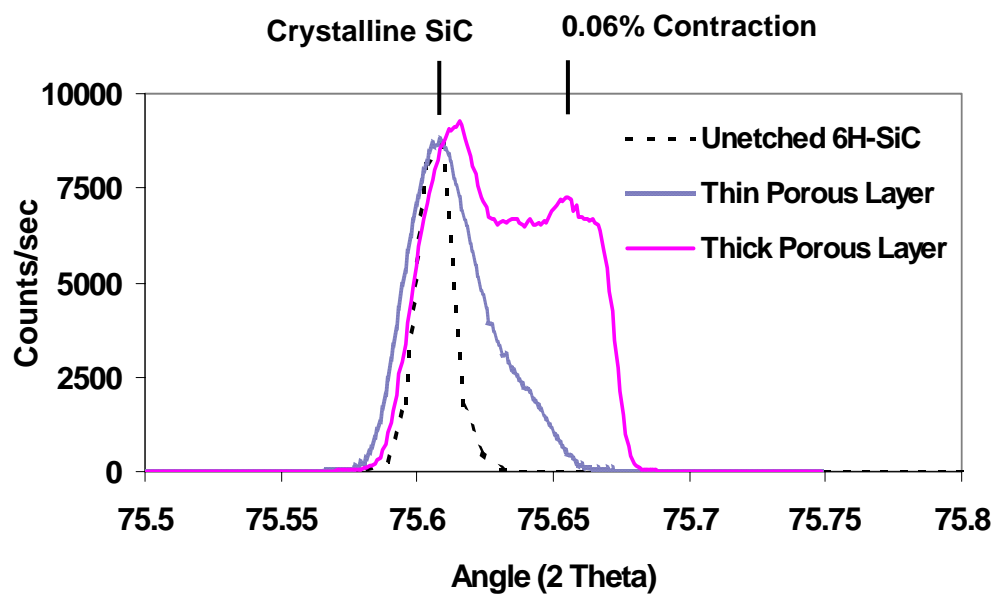
Figure 2.21. High resolution X-ray diffraction rocking curve of unetched 6H-SiC (dashed trace), a PSiC sample with only a surface layer of pores (dotted trace), and a PSiC sample that had a porous layer greater than 100 μm thick (solid trace).
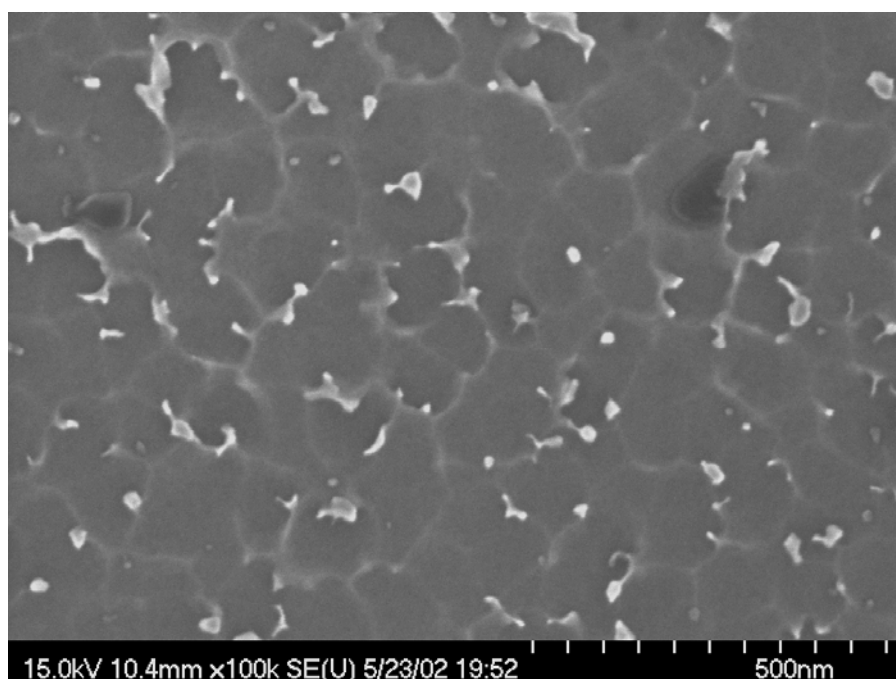
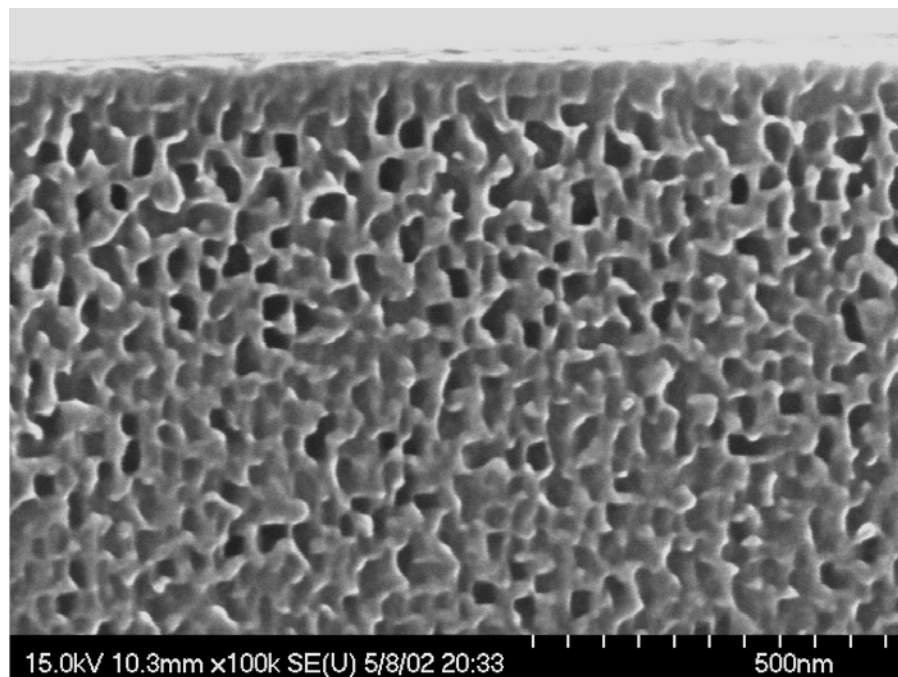Figure 2.22. Plan view SEM image of PSiC prepared from n-type 4H-SiC by electroless etching in dilute HF etchant for 60 min.

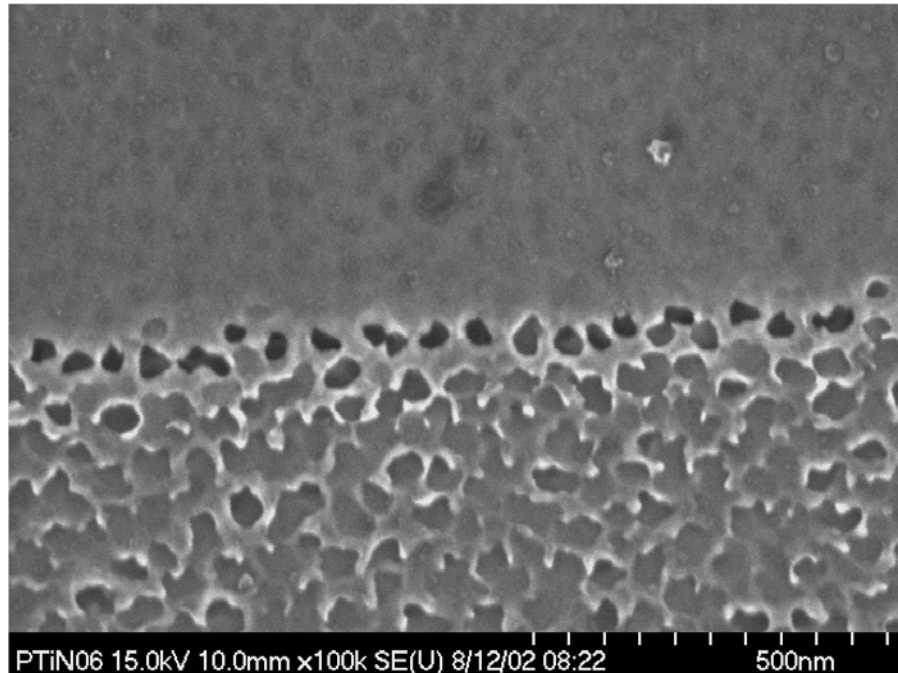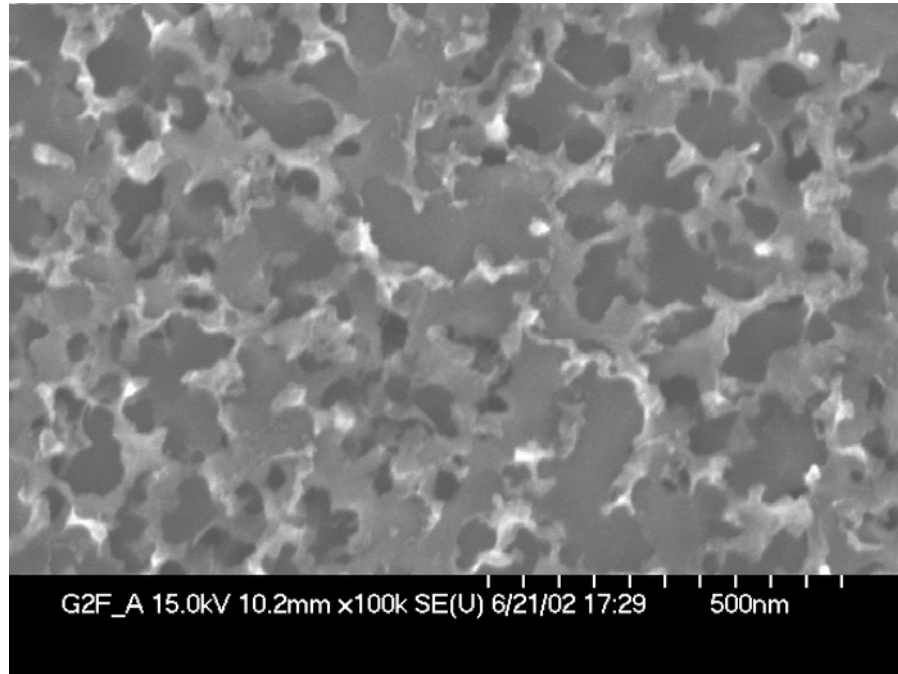Figure 2.23. Plan view SEM image of PSiC prepared from n-type 4H-SiC by electroless etching in dilute HF etchant for 60 min.
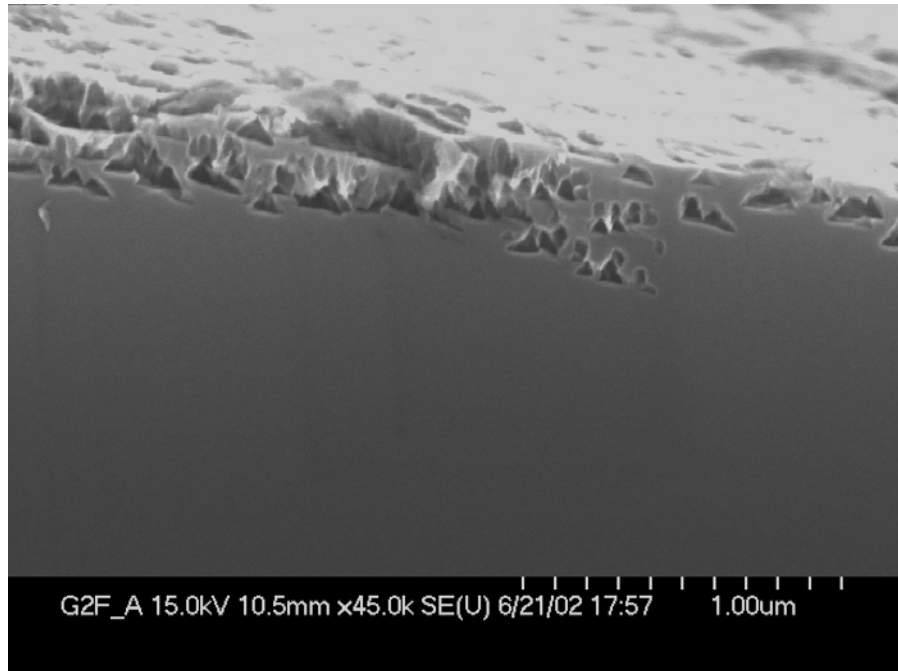
Figure 2.24. Cross-sectional SEM image of PSiC prepared from n-type 4H-SiC by electroless etching in dilute HF etchant for 60 min.
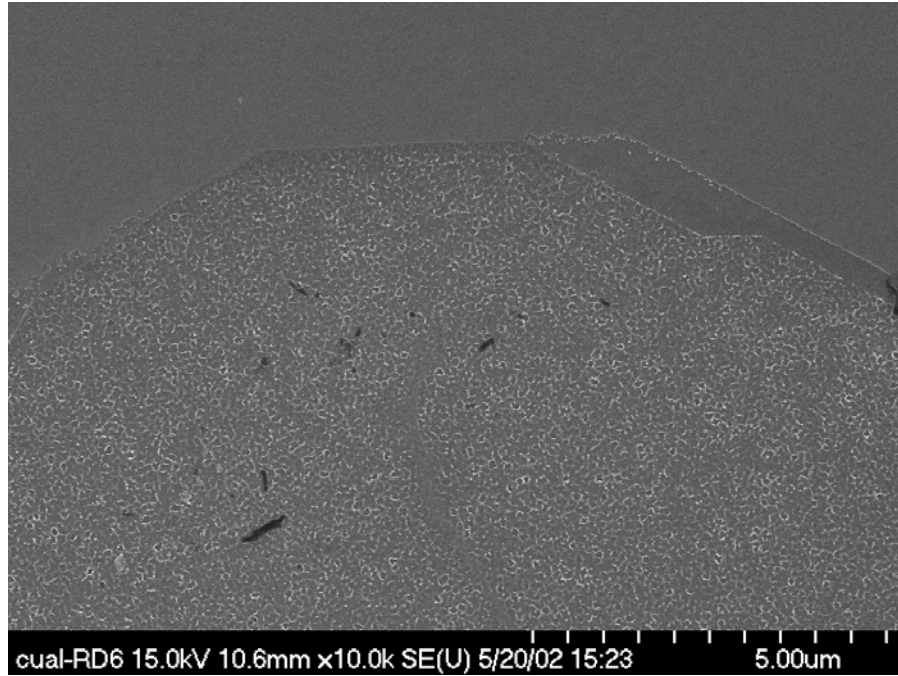
Figure 2.25. Plan view SEM image of the interface between 4H-SiC (etched, bottom) and 6H-SiC (planar, top) showing the crystallographic dependence of the etching when both polytypes are present in the same planar region.
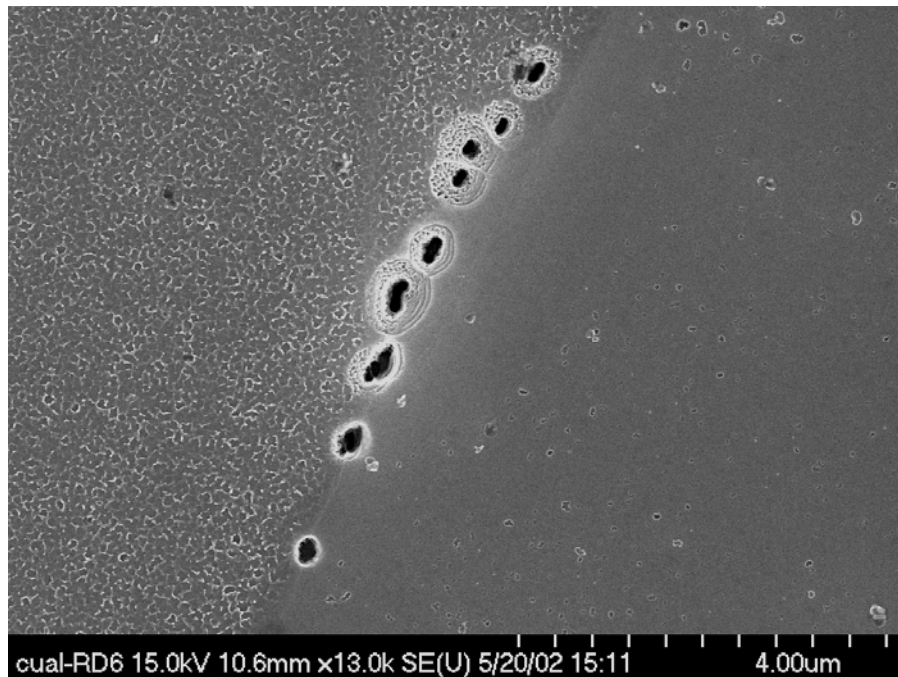
Figure 2.26. Plan view SEM image of micropipes at the interface between 4H-SiC (etched, left) and 6H-SiC (planar, right).
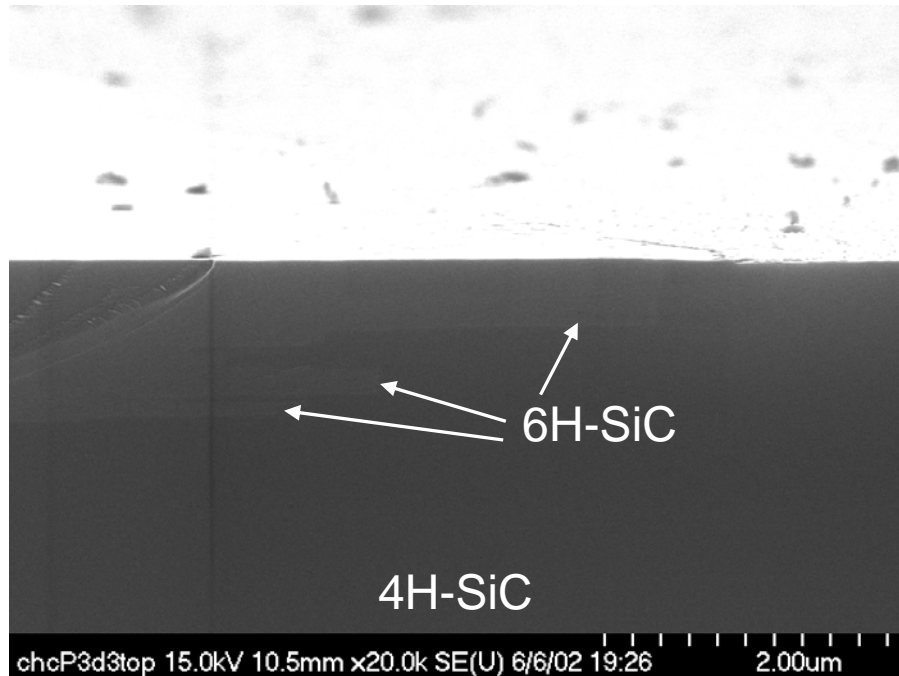
Figure 2.27. Cross-sectional SEM view of the 4H-SiC (right, etched) undercutting the 6H-SiC (left, planar) within the bulk of the wafer.

Like the 6H-SiC, porous 4H-SiC often showed interesting morphologies in the direct vicinity of micropipes that terminated on the free surface. One example is the highly porous structure surrounding a micropipe, which then has an abrupt transition to a less porous structure (Figs. 2.28 and 2.29). This once again points to the disruption of the lattice structure (which is certainly disturbed near a micropipe) playing a key role in the formation of porous structures in SiC.

2.3.1.3 p-doped 4H-SiC

The p-doped 4H-SiC wafer was exposed to both the dilute and concentrated HF etchant for a variety of times, and etching was attempted on both the polished Si side as well as the polished C side. However, no etching of the wafer was ever witnessed. The etchant only accentuated the scratches and introduced a few pits on the surface (Figs. 2.30 and 2.31).

2.3.1.4 Semi-insulating 6H-SiC

A small piece of semi-insulating 6H-SiC was obtained from a collaborator (Dr. Steve Saddow) and exposed to the dilute HF electroless etchant. Etching of semi-insulating material is particularly

34

attractive, since anodic etching techniques cannot be used with a semi-insulating wafer. However, after exposure to the electroless etchants, only limited pitting was observed, and no porous morphology formed (Fig 2.32).

2.3.1.5 General Conclusions: Electroless Etching and Morphology

Analysis of the band diagram at the interface between crystalline SiC and Pt metal provides context in which to interpret the relationship of electroless etching and morphology in n-doped SiC, and why semi-insulating and p-doped wafers do not etch under the electroless etching conditions. This behavior can be understood with reference to the band diagram in Fig. 2.33. The left hand side of the figure illustrates the commonly encountered case of Schottky barrier formation at a metal/n-SiC interface. The barrier is formed by the energy difference between the Fermi level in the metal and the first available state in SiC, which is located at the conduction band edge. Similarly there is a barrier for hole injection in p-type SiC, as shown on the right hand side of Fig. 2.33. Clearly band bending occurs in a direction opposite to that necessary for etching for both the semi-insulating and p-doped SiC, and this explains why electroless etchants were unable to make these wafers porous. The magnitude of the barrier for hole injection could be lessened by utilizing a metal with a larger work function (difference between the vacuum level, E_0, and the Fermi level). Unfortunately, Pt already has one of the largest work functions available, and it is clearly desirable due to its catalytic activity.

When using $HF:K_2S_2O_8$ etchant, the porous morphology obtained is highly dependent upon the crystallographic quality of the starting SiC wafer. Defects such as dislocations and micropipes, in particular, become highly decorated during etching, and current technology still produces wafers of relatively high ($\sim 10^6$ cm^{-2}) screw dislocation density.[2,50] Another example of the role of defects is presented in Fig. 2.34. This cross-sectional SEM image is obtained from a wafer that has been cleaved through a micropipe, which is seen on the right side of the image, in contrast to the bulk of the wafer on the left side of the image. On the internal micropipe wall, rows of small (~50 nm) etch pits are clearly aligned perpendicular to the longitudinal axis of the micropipe. The alignment of these pits suggests that they are due to dislocations, since dislocations often align relative to a crystalline axis in order to reduce
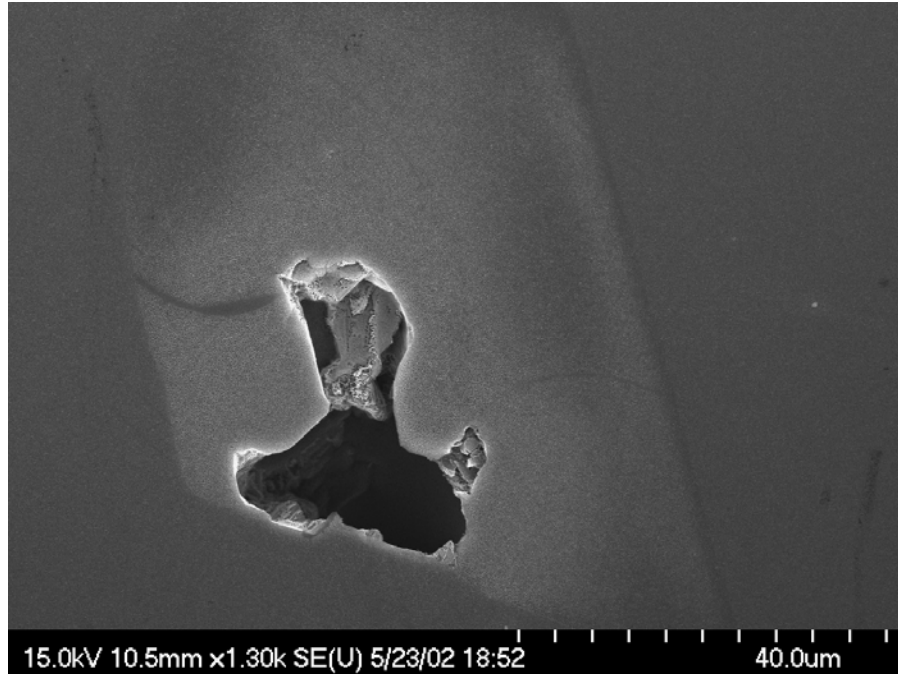
Figure 2.28. Plan view SEM image of a large defect and the region of increased porosity (lighter regions) in the immediate vicinity of the defect.
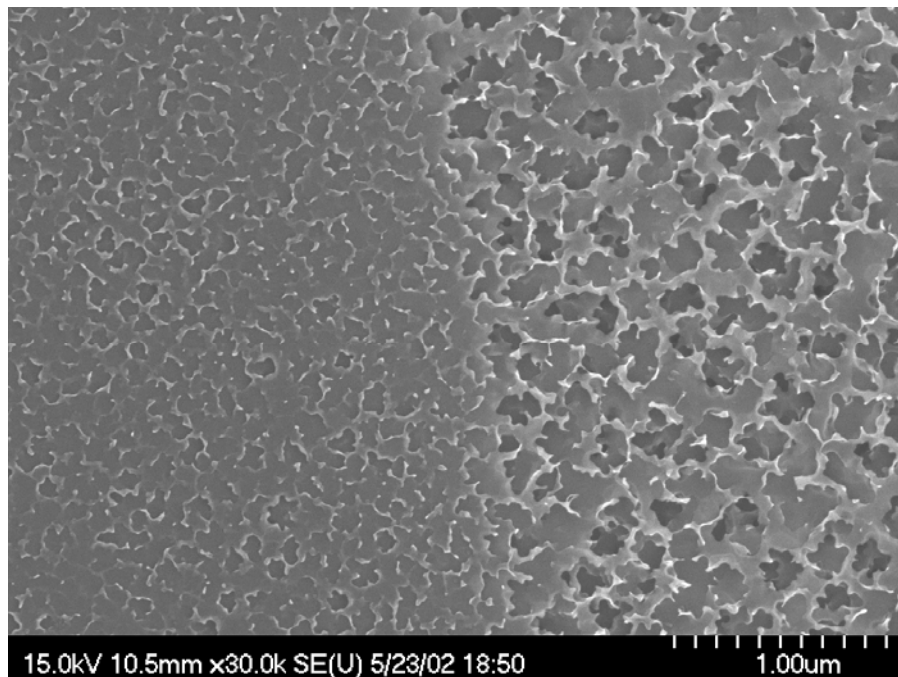
Figure 2.29. Plan view SEM image of the wafer in Fig. 2.28. This close-up image shows the sharp interface between the relatively weakly etched regions (dark in Fig. 2.28) next to the more strongly etched regions (light in Fig. 2.28).
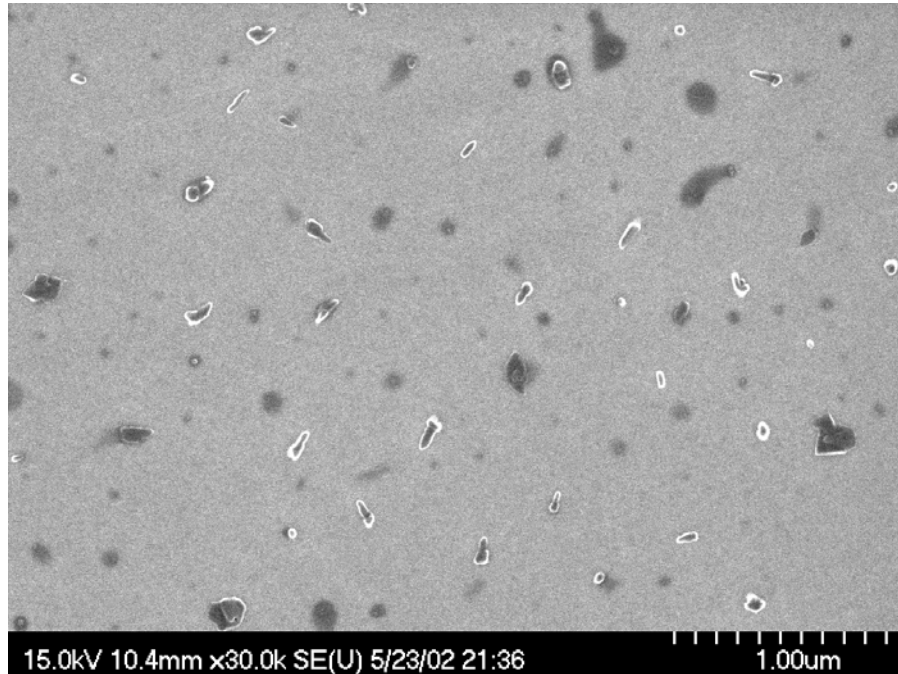
Figure 2.30. Plan view SEM image of p-doped 4H-SiC (polished silicon side) that has been exposed to the dilute HF etchant for 60 min.
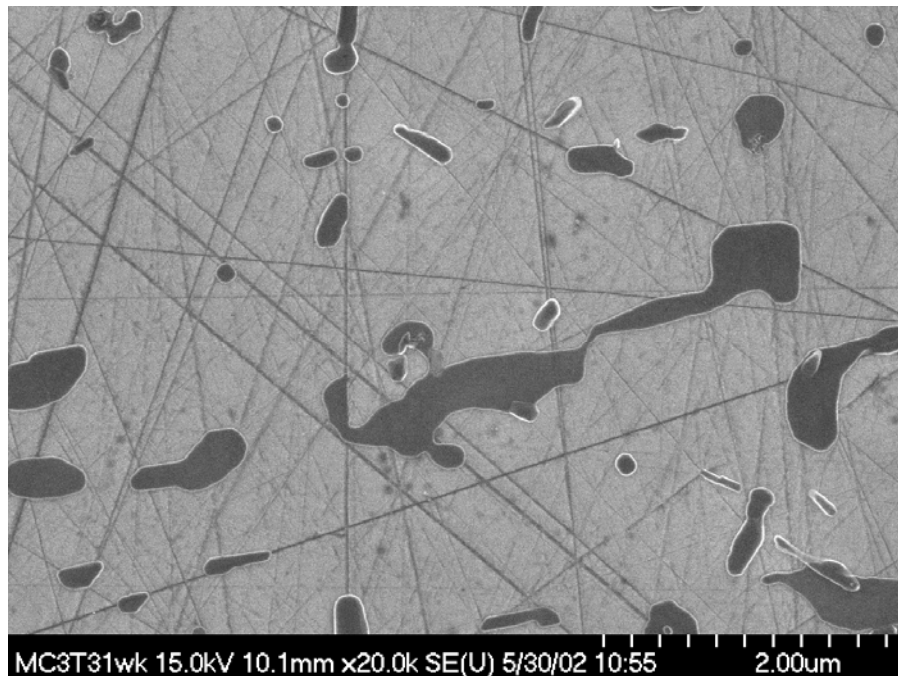
Figure 2.31. Plan view SEM image of p-doped 4H-SiC (polished carbon side) that has been exposed to the dilute HF etchant for 60 min.
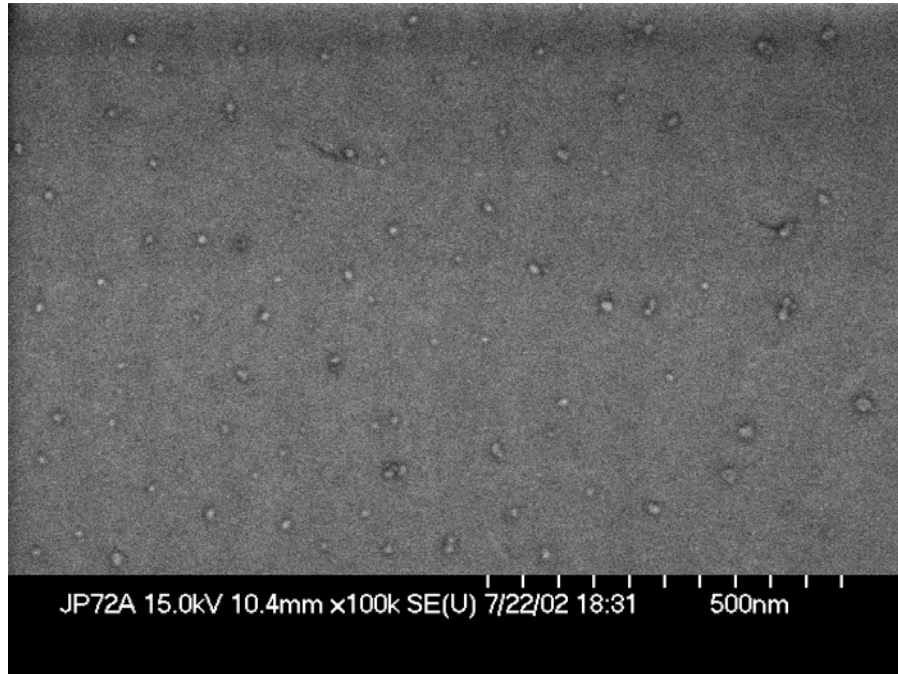
Figure 2.32. Plan view SEM image of semi-insulating 6H-SiC that has been exposed to the dilute HF etchant for 60 min.

overall stress. Published results are inconclusive about the presence of dislocations near micropipes; studies show both the presence of dislocations near micropipes[57,58] as well as dislocation-free 6H morphology preserved even at the micropipe surface.[59] Alternatively, the etch pits in the micropipe could form selectively on certain growth planes that spiral around the micropipe,[58,60,61] although it is unknown why the etch pits would align only on certain growth planes. Regardless of the specific mechanism responsible for the alignment, the locations of the etch pits are not random and are inherently linked to the crystallographic nature of the SiC substrate.

2.3.2 Anodically Etched SiC

Numerous pieces of the 6H-SiC wafer were anodically etched, in order to study the effect of etching parameters such as the etchant concentration, etch voltage, and etch current. Representative examples of different properties were observed from the etch conditions listed in Table 2.1. All of the pieces listed in Table 2.1 were etched for 40 min.
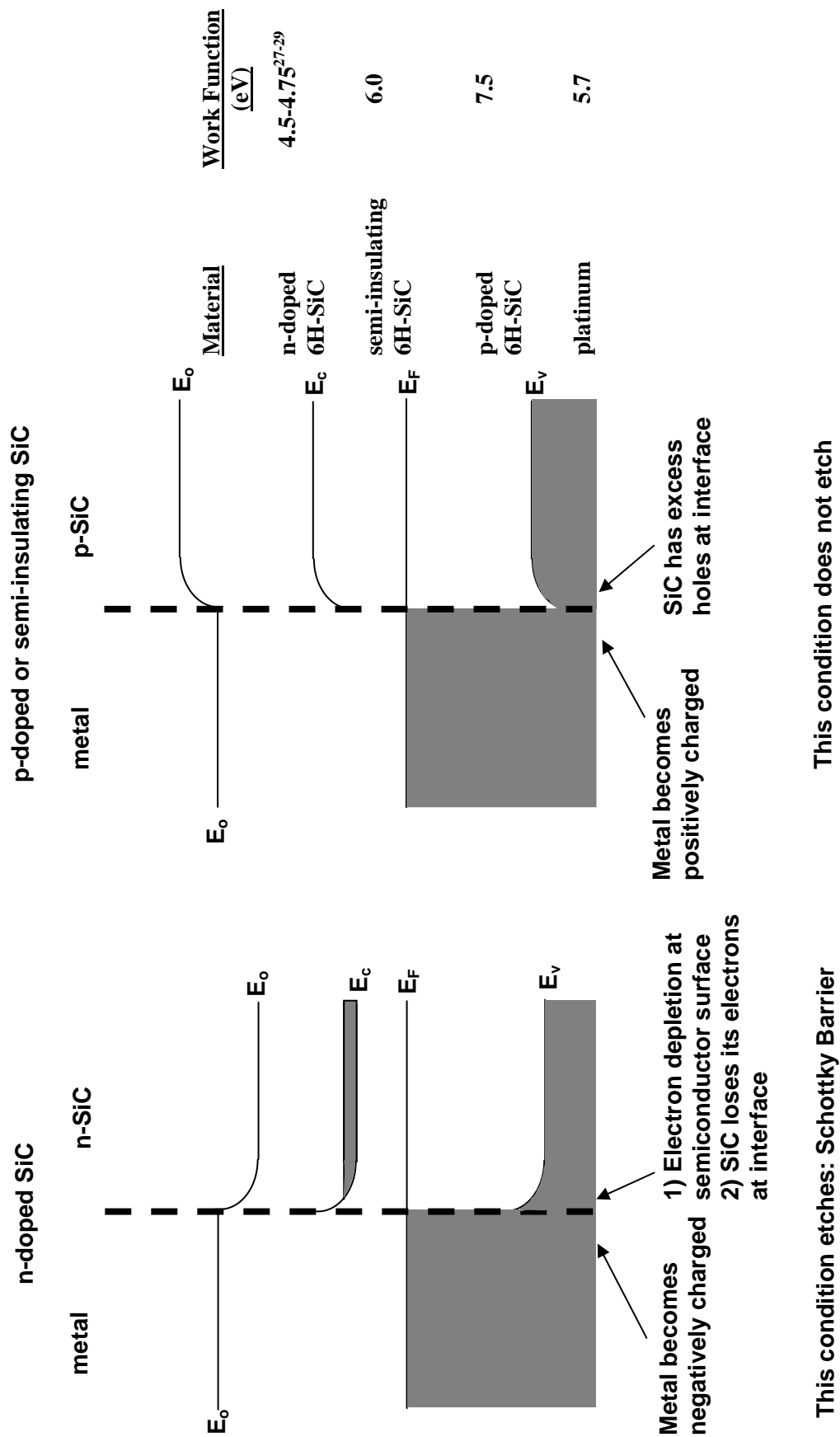
Figure 2.33. Band diagrams of Pt metal/SiC interfaces.
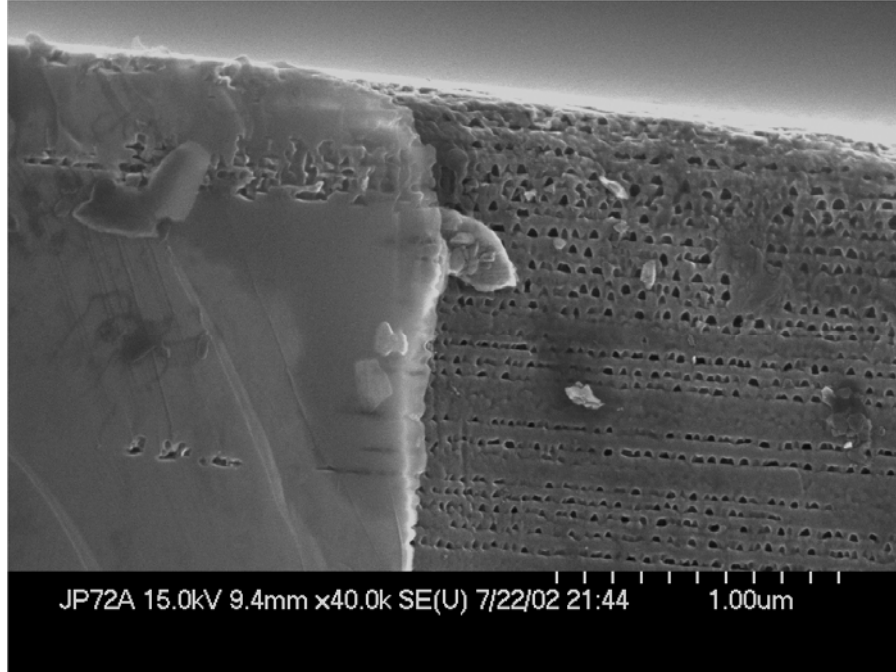
Figure 2.34. Cross-sectional SEM image of a PSiC sample cleaved through a micropipe (right side) and the surrounding bulk wafer (left side). Etch pits are observed at high density on the internal micropipe wall, aligned perpendicular to its longitudinal axis. The pits are much more sparse in the bulk portion of the wafer.

Table 2.1. PSiC Etching Conditions

Sample #	Etch Voltage (V)	Etch Current (mA/cm^2)	Porous Layer Thickness (μm)
1	3	80	3
2	4	40	4
3	4	35	2
4	5	35	7
5	4	20	10
6	3	10	3

The top surface of each anodically etched PSiC wafer is composed of nanofingers of SiC arranged in random fashion (Fig. 2.35). In cross-section, the PSiC layers consistently show a propensity for triangular pitting. In most instances, the triangular etch pits do not follow a regular pattern, and, therefore, a highly branched structure results (Figs. 2.36 and 2.37). The PSiC nanocrystallites have an average diameter of approximately 25 nm, regardless of the forward bias (3-5 V) or current density (10-

80 mA/cm^2) used to etch each wafer. The morphology is striking in that the size of the pores seen in cross-section is relatively monodisperse.

In one PSiC sample (sample #4), the triangular etch pits were observed to orient regularly upon planes parallel to the top free surface of the wafer (Fig. 2.38). This pitting structure is reminiscent of the triangular etch pits seen within the micropipe in PSiC produced via electroless etching (Fig. 2.34). Sample #4 was prepared from the same wafer as the other PSiC samples discussed in this work, so the cause of this particular morphology is unknown.

2.4 BET Surface Area Analysis

The high surface area characteristic of porous materials is one of the drivers for their application in sensing platforms. Surface areas for several PSiC samples formed via electroless etching were measured via BET isotherms to be ~150 m^2/cm^3, which is comparable to the surface areas obtained in anodically etched PSi.[62] All of the anodically etched pieces in this work were limited to 10 μm deep or less. Considering that all etched pieces were ~5 x 5 mm in size or less, no single piece of anodically etched material had a substantial amount of total surface area for accurate adsorption measurements. For this reason, accurate surface area analysis via BET isotherms was never obtained for any of the anodically etched pieces produced in this work.

2.5 Conclusions

Electroless etching of SiC in HF and S$_2$O$_8^{2-}$ is competent to form PSiC, although reproducible formation of deep porous structures remains an unsolved issue. The spatial extent of porosity in PSiC is dependent on the polytype and on the crystallographic perfection of the wafer. Furthermore, for 6H-SiC the resulting morphology depends on the etchant concentrations. Surface areas on the order of 150 m^2/cm^3 can be produced easily, and in 6H-SiC an extensively interconnected network of pores can be achieved to significant depths (> 100 μm). These factors argue for the efficient transport of reactants and products within the interconnected network and imply that these materials are suitable for use as chemical and physical sensors.
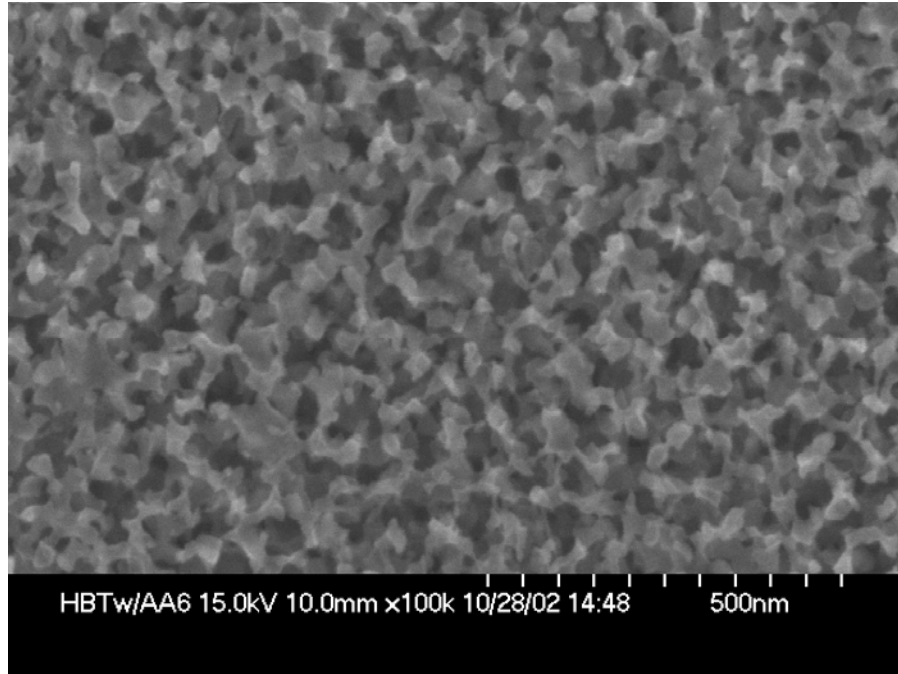
Figure 2.35. Plan view SEM image of PSiC prepared from n-type 6H-SiC by anodic etching for 40 min.
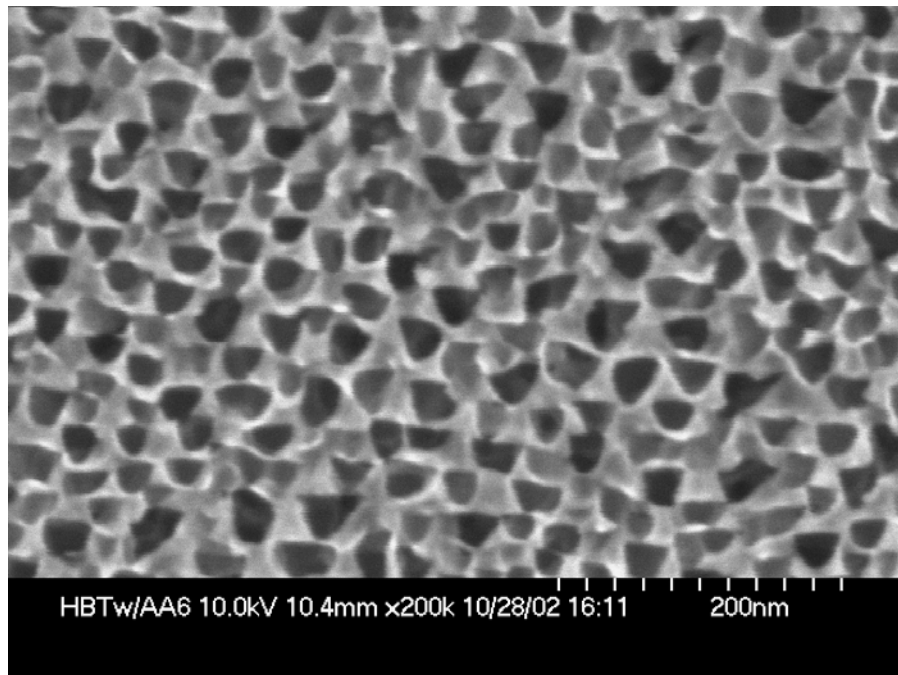
Figure 2.36. Cross-sectional SEM image of PSiC prepared from n-type 6H-SiC by anodic etching for 40 min.
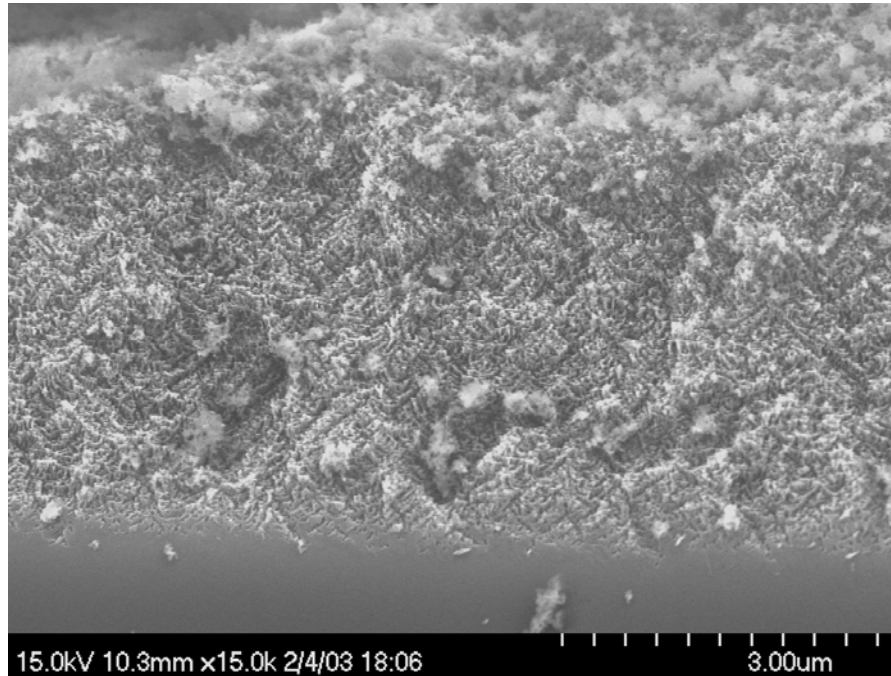
Figure 2.37. Cross-sectional SEM image of PSiC prepared from n-type 6H-SiC by anodic etching for 40 min.
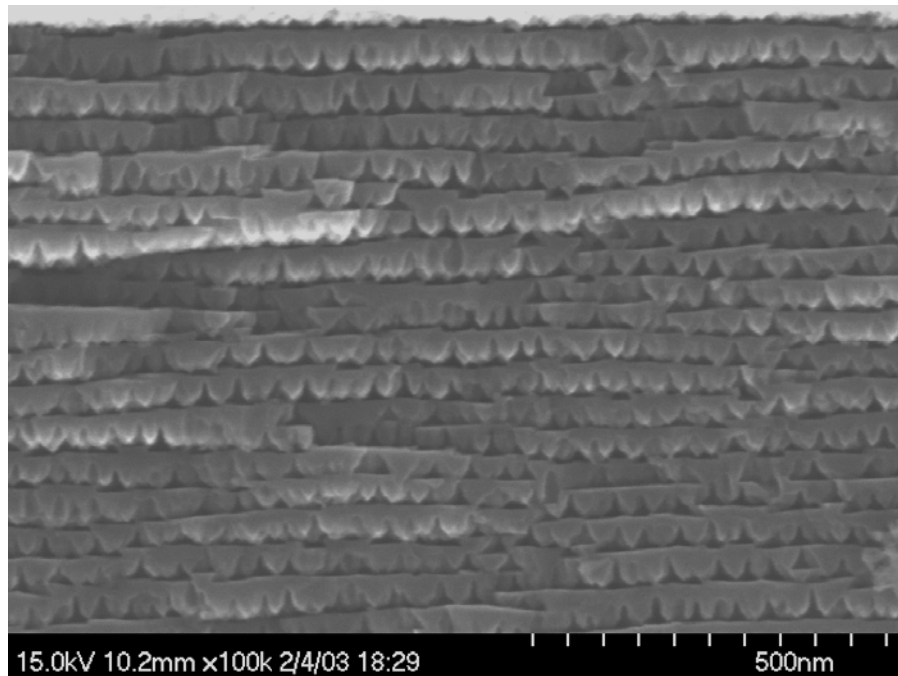
Figure 2.38. Cross-sectional SEM image of PSiC prepared from n-type 6H-SiC by anodic etching for 40 min.

Anodic etching of SiC yielded morphologies similar to electroless etching. However, greater control of the depth of porous etching is possible with anodic etching. For this reason, anodic etching was used in the production of PSiC samples tested for their sensing capabilities (Chapter 4).

2.6 References

(1)   Saddow, S. E.; Mynbaeva, M.; Smith, M. C. D.; Smirnov, A. N.; Dimitriev, V. *Appl. Surf. Sci.* **2001**, *184*, 72.

(2)   Mynbaeva, M.; Saddow, S. E.; Melnychuk, G.; Nikitina, I.; Scheglov, M.; Sitnikova, A.; Kuznetsov, N.; Mynbaev, K.; Dmitriev, V. *Appl. Phys. Lett.* **2001**, 117.

(3)   Spanier, J. E.; Dunne, G. T.; Rowland, L. B.; Herman, I. P. *Appl. Phys. Lett.* **2000**, *76*, 3879.

(4)   Mynbaeva, M.; Saddow, S. E.; Melnychuk, G.; Nikitina, I.; Scheglov, M.; Sitnikova, A.; Kuznetsov, N.; Mynbaev, K.; Dmitriev, V. *Mat. Res. Soc. Symp. Proc.* **2000**, *587*, O8.6.1.

(5)   Soldatenkov, F. Y.; Ulin, V. P.; Yakovenko, A. A.; Fedorova, O. M.; Konnikov, S. G.; Korolkov, V. I. *Tech. Phys. Lett.* **1999**, *25*, 852.

(6)   Rost, C.; Sieber, I.; Fischer, C.; Lux-Steiner, M. C.; Konenkamp, R. *Mat. Sci. Engng. B* **2000**, *B69-70*, 570.

(7)   Gao, J.; Gao, T.; Sailor, M. J. *Appl. Phys. Lett.* **2000**, *77*, 901.

(8)   George, M. A.; Ayoub, M. A.; Ila, D.; Larkin, D. J. *Mat. Res. Soc. Symp. Proc.* **1999**, *572*, 123.

(9)   Ben-Chorin, M.; Kux, A.; Schechter, I. *Appl. Phys. Lett.* **1994**, *64*, 481.

(10)   Letant, S. E.; Content, S.; Tan, T. T.; Zenhausern, F.; Sailor, M. J. *Sens. Act. B* **2000**, *69*, 193.

(11)   Zangooie, S.; Bjorklund, R.; Arwin, H. *Sens. Act. B* **1997**, *43*, 168.

(12)   Dezauzier, C.; Becourt, N.; Arnaud, G.; Contreras, S.; Ponthenier, J. L.; Camassel, J.; Robert, J. L.; Pascual, J.; Jaussaud, C. *Sens. Act. A* **1995**, *46-47*, 71.

(13)   Propst, E. K.; Kohl, P. A. *J. Electrochem. Soc.* **1994**, *141*, 1006.

(14)   Rieger, M. M.; Kohl, P. A. *J. Electrochem. Soc.* **1995**, *142*, 1490.

(15)   Dimova-Malinovska, D.; Sendova-Vassileva, M.; Tzenov, N.; Kamenova, M. *Thin Solid Films* **1997**, *297*, 9.

(16)   Bardwell, J. A.; Webb, J. B.; Tang, H.; Fraser, J.; Moisa, S. *J. Appl. Phys.* **2001**, *89*, 4142.

(17)   Shor, J. S.; Kurtz, A. D. *J. Electrochem. Soc.* **1994**, *141*, 778.

(18)   Shor, J. S.; Osgood, R. M. *J. Electrochem. Soc.* **1993**, *140*, L123.

(19)   Shor, J. S.; Zhang, X. G.; Osgood, R. M. *J. Electrochem. Soc.* **1992**, *139*, 1213.

(20)   Shor, J. S.; Osgood, R. M.; Kurtz, A. D. *Appl. Phys. Lett.* **1992**, *60*, 1001.

(21)   Li, X.; Bohn, P. W. *Appl. Phys. Lett.* **2000**, *77*, 2572.

(22)   Li, X.; Kim, Y.; Bohn, P. W.; Adesida, I. *Appl. Phys. Lett.* **2002**, *80*, 980.

(23)   Diaz, D. J.; Williamson, T. L.; Adesida, I.; Bohn, P. W.; Molnar, R. J. *J. Vac. Sci. Technol. B* **2002**, *20*, 2375.

(24)   Chattopadhyay, S.; Li, X.; Bohn, P. W. *J. Appl. Phys.* **2002**, *91*, 6134.

(25)   Shor, J. S.; Grimberg, I.; Weiss, B.; Kurtz, A. *Appl. Phys. Lett.* **1993**, *62*, 2836.

(26)   Shor, J. S.; Bemis, L.; Kurtz, A. D.; Grimberg, I.; Weiss, B. Z.; MacMillan, M. F.; Choyke, W. J. *J. Appl. Phys.* **1994**, *76*, 4045.

(27)   Matsumoto, T.; Takahashi, J.; Tamaki, T.; Futagi, T.; Mimura, H.; Kanemitsu, Y. *Appl. Phys. Lett.* **1994**, *64*, 226.

(28)   Petrova-Koch, V.; Sreseli, O.; Polisski, G.; Kovalev, D.; Muschik, T.; Koch, F. *Thin Solid Films* **1995**, *255*, 107.

(29)   Konstantinov, A. O.; Henry, A.; Harris, C. I.; Janzen, E. *Appl. Phys. Lett.* **1995**, *66*, 2250.

(30)   Jessensky, O.; Muller, F.; Gosele, U. *Thin Solid Films* **1997**, *297*, 224.

(31)   Parkhutik, V. P.; Namavar, F.; Andrade, E. *Thin Solid Films* **1997**, *297*, 229.

(32)   Danishevskii, A. M.; Zamoryanskaya, M. V.; Sitnikova, A. A.; Shuman, V. B.; Suvorova, A. A. *Semicond. Sci. Technol.* **1998**, *13*, 1111.

(33)   Shin, W.; Hikosaka, T.; Seo, W.; Ahn, H. S.; Sawaki, N.; Koumoto, K. *J. Electrochem. Soc.* **1998**, *145*, 2456.

(34)   Zangooie, S.; Woollam, J. A.; Arwin, H. *J. Mater. Res.* **2000**, *15*, 1860.

(35)   Kim, S.; Spanier, J. E.; Herman, I. P. *Jpn. J. Appl. Phys.* **2000**, *39*, 5875.

(36)   Hassen, F.; M'Ghaieth, R.; Maaref, H.; Madar, R. *Mat. Sci. Engng. C* **2001**, *15*, 113.

(37)   Sagar, A.; Lee, C. D.; Feenstra, R. M.; Inoki, C. K.; Kuan, T. S. *J. Appl. Phys.* **2002**, *92*, 4070.

(38)   Shuman, V. B.; Ratnikov, V. V.; Savkina, N. S. *Tech. Phys. Lett.* **2002**, *28*, 414.

(39)   Takazawa, A.; Tamura, T.; Yamada, M. *Jpn. J. Appl. Phys.* **1993**, *32*, 3148.

(40)   van de Lagemaat, J.; Plakman, M.; Vanmaekelbergh, D.; Kelly, J. J. *Appl. Phys. Lett.* **1996**, *69*, 2246.

(41)   Spanier, J. E.; Cargill III, G. S.; Herman, I. P.; Kim, S.; Goldstein, D. R.; Kurtz, A. D.; Weiss, B. Z. *Mat. Res. Soc. Symp. Proc.* **1997**, *452*, 491.

(42)   Sorokin, L. M.; Savkina, N. S.; Shuman, V. B.; Lebedev, A. A.; Mosina, G. N.; Hutchison, G. *Tech. Phys. Lett.* **2002**, *28*, 935.

(43)   Soloviev, S.; Das, T.; Sudarshan, T. S. *Electrochem. Solid-State Lett.* **2003**, *6*, G22.

(44) Savkina, N. S.; Sorokin, L. M.; Hutchison, J. L.; Sloan, J.; Tregubova, A. S.; Mosina, G. N.; Shuman, V. B.; Ratnikov, V. V. *Appl. Surf. Sci.* **2001**, *184*, 252.

(45) Monguchi, T.; Fujioka, H.; Uragami, T.; Ohuchi, H.; Ono, K.; Baba, Y.; Oshima, M. *J. Electrochem. Soc.* **2000**, *147*, 741.

(46) Adamson, A. W. *Physical Chemistry of Surfaces*; 5th ed.; John Wiley and Sons, Inc.: New York, 1990.

(47) Gomer, R.; Tryson, G. *J. Chem. Phys.* **1977**, *66*, 4413.

(48) Diaz, D., personal communication.

(49) Zangooie, S.; Persson, P. O. A.; Hilfiker, J. N.; Hultman, L.; Arwin, H. *J. Appl. Phys.* **2000**, *87*, 8497.

(50) Savkina, N. S.; Ratnikov, V. V.; Shuman, V. B. *Semiconductors* **2001**, *35*, 153.

(51) Alok, D.; Bhatnagar, M.; Nakanishi, H.; Baliga, B. J.; Chang, Y.; Davis, R. F. *Inst. Phys. Conf. Ser.* **1993**, *137*, 585.

(52) Manotas, S.; Agullo-Rueda, F.; Moreno, J. D.; Ben-Hander, F.; Martinez-Duart, J. M. *Thin Solid Films* **2001**, *401*, 306.

(53) Chamard, V.; Dolino, G. *J. Appl. Phys.* **2001**, *89*, 174.

(54) Andrianov, A. V.; Polisski, G.; Morgan, J.; Koch, F. *J. Lumin.* **1999**, *80*, 193.

(55) Chamard, V.; Pichat, C.; Dolino, G. *Eur. Phys. J. B* **2001**, *21*, 185.

(56) Milita, S.; Servidori, M.; Maccagnani, P.; Cembali, F.; Pozzi, P.; Dori, L. *J. Electrochem. Soc.* **2001**, *148*, G447.

(57) Giocondi, J.; Rohrer, G. S.; Skowronski, M.; Balakrishna, V.; Augustine, G.; Hobgood, H. M.; Hopkins, R. H. *J. Cryst. Growth* **1997**, *181*, 351.

(58) Syvajarvi, M.; Yakimova, R.; Janzen, E. *J. Electrochem. Soc.* **2000**, *147*, 3519.

(59) Heindl, J.; Strunk, H. P.; Heydemann, V. D.; Pensl, G. *Phys. Status Solidi A* **1997**, *162*, 251.

(60) Mahajan, S. *Appl. Phys. Lett.* **2002**, *80*, 4321.

(61) Harris, G. L. *Properties of Silicon Carbide*, 1995.

(62) Snow, P. A.; Squire, E. K.; Russell, P. S. J.; Canham, L. T. *J. Appl. Phys.* **1999**, *86*, 1781.

CHAPTER 3

SPECTROSCOPIC CHARACTERIZATION

3.1 Introduction

In addition to sensors and substrates for epitaxial growth, another application that has received widespread attention is the possibility of using porous semiconductors as light emitting diodes (LEDs). Research into porous semiconductors grew exponentially after the seminal discovery by Canham that porous silicon is capable of light emission at photon energies in excess of the bulk bandgap.[1] The blue-shifted emission from PSi is apparently tunable via manipulation of the etching conditions.[2-5] The intensity of the light emission from PSi is often reported to be as much as 500 times more intense than emission from crystalline Si.[6,7]

Quantum confinement effects are one plausible explanation for the blue-shifted emission. In an indirect bandgap semiconductor, bandgap transitions are dipole forbidden due to translational symmetry. However, when a small nanocrystallite is formed, a superposition of eigenstates with a distribution of **k** values is necessary to physically localize the wavefunction inside the nanocrystal. In turn, physical localization breaks the translational symmetry, allowing for the mixing of eigenstates with different **k** values. As a result, the combination of a relaxation of the momentum selection rules as well as distortions of the local band structure can allow for direct bandgap transitions in nanocrystallites of indirect gap Si. However, researchers have encountered difficulties in producing a PSi LED. Particularly, emission from the shorter (blue) wavelengths has proven to be unstable and still relatively weak.

The successes with silicon naturally led investigators to question whether comparably enhanced properties could be coaxed from porous analogs of wide bandgap materials, such as silicon carbide and gallium nitride. Because silicon carbide is an indirect bandgap material, the luminescence of SiC LEDs is very low (quantum efficiency only $\sim10^{-4}$), an efficiency unsuitable in applications such as LED displays. However, if PSiC could be developed to exhibit properties similar to those of porous silicon, a bright UV LED could be realized.[8-11]

In addition to exploring the possibility of producing UV LEDs, spectroscopic studies provide a tool to characterize the porous nanostructure. Cathodoluminescence and photoluminescence spectra of PSiC were collected in this work in order to look for a possible blue-shift in emission due either to quantum confinement effects or to the formation of new emissive surface states upon etching. The exact peak location for the bandgap of SiC shifts slightly from wafer to wafer due to differences in doping; for the samples examined in this work, the peak cathodoluminescence (CL) bandgap emission occurred at 426 nm (6H-SiC) or 392 nm (4H-SiC).

Few observations of CL emission from PSiC layers have been reported, and reported observations of UV emission have been inconsistent. Shor et. al.[12,13] reported a UV CL emission peak at 335 nm, which was assigned to the native oxide or possibly quantum confinement effects. Danishevskii et. al.[14] reported evidence of increased CL emission centered at 468 nm, but no UV emission.

PL emission from crystalline SiC has been well documented in the literature. Depending upon the doping concentrations, a broad peak appearing between 580-620 nm has been attributed to a combination of N^--B^+ recombination and "defect" luminescence.[15-17] When aluminum impurities are present in the wafer, a broad peak centered near 470 nm may be seen and is assigned to N^--Al^+ recombination.[15]

A variety of photoluminescence results have been published for anodically etched PSiC. There are several reports in the literature of an increase in photoluminescence intensity in the 460-500 nm region of the spectrum upon formation of PSiC.[15-23] Increased emission in this wavelength range has been reported for both porous material prepared from both 4H and 6H polytypes of SiC; PL emission does not appear to be polytype dependent when the SiC is made porous by anodic etching. In contrast, a few authors report that formation of PSiC results in relatively small or no shift in the PL of the wide visible band attributed to defects and N^--B^+ recombination.[17,24,25] No published research has indicated PL emission in the ultraviolet region (blue of the bandgap emission). The bandgap emission itself is difficult to see in PL experiments due to the indirect nature of the bandgap in SiC.

The origin of the large blue shift in the visible photoluminescence of PSiC with respect to bulk SiC is not yet firmly established. Two categories of mechanisms, categorized as extrinsic or intrinsic in nature, have been invoked to explain this PL.

There are many proposed extrinsic changes that may occur in PSiC to cause blue-shifted PL emission. For example, changes in the Raman spectra led Danishevskii et. al. to report the formation of 3C-SiC (the cubic polytype) nanocrystallites within the hexagonal matrix of the wafer.[26] Parkhutik et. al. theorize the formation of Si nanocrystallites within the SiC matrix.[27]

A different train of thought involves the formation of some type of surface hydride species or some other change to the surface of the SiC crystal. Researchers who have witnessed altered PL emission characteristics upon oxidation or hydrogenation of the PSiC surface often propose this argument. Surface state impurities proposed as causes of blue-shifted PL include species such as hydrogenated amorphous silicon carbide.[8] The passivation of dangling bonds has also been theorized as the cause of blue PL, since dangling bonds can serve as nonradiative recombination centers (localized states) in the bandgap.[28] Some researchers claim that etching results in an increase of C-H terminations on the surface[24,29,30] or Si-H terminations on the surface.[31] Finally, some researchers have proposed that etching causes an increase of defects on the surface, and these defects serve as recombination centers for new PL.[18,25,26,32,33]

However, the blue-shifted PL may also be due to an intrinsic change: the development of topographically altered structures which can support quantum confinement effects. Distortion of the local band structure could lead to the relaxation of momentum selection rules, thereby allowing direct transitions in the semiconductor material and, hence, an increase in emission efficiency. The apparent tunability of the wavelength of maximum PL emission with varying etching conditions points to a quantum confinement effect explanation. However, to exhibit quantum confinement, the widths of the nanocrystallites must be significantly less than the dimensions of the free exciton. The free exciton is ~50 Å in Si;[3] the free exciton size for SiC was not located in the literature, but reports in the literature indicate that spherical nanocrystallites in PSiC must also have diameters <50 Å to show significant increases in

bandgap emission.[3,5,13,34-37] These small dimensions were not observed in some of the samples that displayed blue-shifted PL in the literature.[21]

Evidence for a quantum confinement effect in PSiC can be revealed by Raman scattering measurements, as well. Formation of a porous nanostructure leads to broadening and shifting of Raman bands, because the translational lattice symmetry is relaxed, and coupling of phonon states with different **k** values occurs. Previous work[2,37-42] has shown that phonon confinement effects cause the longitudinal optic (LO) mode of PSi to broaden asymmetrically to the low-frequency side and red-shift as nanostructures are formed. Since the morphology investigations reported in Chapter 2 clearly show evidence of nanostructure formation, Raman investigations were conducted in an attempt to quantify the degree of porosity non-destructively. However, Raman data must be interpreted carefully, as other factors such as changes in the doping levels[43,44] and residual stress in the crystal[45-48] can also lead to distortion of the Raman bands. HXRD studies, detailed in Chapter 2, provide evidence that the porous layers formed in this work are under tensile stress, and this stress can distort and shift the Raman bands, if the stress is great enough.

3.2 Cathodoluminescence Spectra

Cathodoluminescence spectra were obtained at beam energies of 1 to 20 keV with a Zeiss DSM 960 SEM utilizing an Oxford Instruments MonoCL monochromator and photomultiplier tube detector (Amherst Scientific).

3.2.1 Electrolessly Etched SiC

CL spectra obtained from porous material produced from both 6H-SiC and 4H-SiC do not show any blue-shift of the bandgap luminescence nor any other changes in the visible portions of the spectra (Figs. 3.1 and 3.2). 6H-SiC spectra were dominated by the bandgap emission at 426 nm and a broad peak near 600 nm due to donor-acceptor recombination. 4H-SiC spectra exhibited a sharp bandgap peak at 392 nm and a broad donor-acceptor recombination peak centered near 480 nm.

Figure 3.1. Cathodoluminescence spectra of unetched 6H-SiC (dashed line) and PSiC prepared from n-type 6H-SiC via electroless etching in dilute HF etchant for 60 min (solid line).

Figure 3.2. Cathodoluminescence spectra of unetched 4H-SiC (dashed line) and PSiC prepared from n-type 4H-SiC via electroless etching in dilute HF etchant for 60 min (solid line).

3.2.2 Anodically Etched SiC

CL spectra of anodically etched PSiC samples produced in this work consistently show peak emission blue of the bandgap emission at 426 nm (Fig. 3.3). CL emission spectra exhibited wavelengths of maximum emission which varied between 355 and 400 nm. Higher etching current densities yielded bluer emission, in agreement with results published elsewhere.[13] The increase in UV CL intensity seems to be accompanied by loss of emission intensity at 590 nm (the peak widely attributed to donor-acceptor $(N^{-}\text{-}B^{+})$ recombination and defects). In addition, the UV peak can become so intense that it entirely masks any bandgap CL emission, *cf.* spectra of samples #4 and #5 in Fig. 3.3.

Special care was taken to examine the UV emission evident in Fig. 3.3, since the observation of significant emission intensity at 300 nm is surprising. In particular spectra were collected several times with a variety of slit widths between the sample and monochromator and the monochromator and photodetector. Even for the smallest collection slit widths (10 µm), the UV emission remained measurable (although weak) at 300 nm.

CL spectra were obtained at 1, 5, 10, 15, and 20 keV in order to observe any difference in the spectra as a function of depth within the wafer. Utilizing the work of Kanaya and Okayama,[49,50] we can predict that accelerating voltages of 1-20 keV correspond to total sampling depths of 0.24-3.6 µm, with maximum emission coming from depths of 0.007-1.1 µm within the porous layer.[51,52] However, no shifts in the CL spectra were observed for the different voltages; the weaker excitation voltages resulted simply in weaker signals. This indicates that the UV CL emission is not restricted to the top surface layer of the porous network.

3.3 Photoluminescence Spectra

Photoluminescence spectra were excited at $\lambda = 325.0$ nm (HeCd laser). A single grating (150 groove/mm) was used in the spectrograph stage for wide spectral coverage, and the filter stage of the spectrometer was not used.

Many reports in the literature quantify increases in PL emission intensity (up to 500 times greater than the emission from crystalline SiC) upon the formation of PSiC. However, it is likely that much of this increased intensity is due to increased outcoupling efficiency attributable to the rough surface formed by etching, and any inherent increases in PL intensity due to the porous network are difficult to isolate. In fact, in this work for the 325 nm laser, the unetched PL data was actually obtained from the back side of the wafer, since it was not polished and therefore yielded a stronger signal. No difference was observed between PL emission from the front and back surfaces except for the increase in intensity from the back surface. In this work, no comparisons of PL emission intensity will be made between samples.

3.3.1 Electrolessly Etched SiC

In contrast to PL results in the literature for anodically etched PSiC, the electrolessly etched PSiC produced in this work never shows maximum PL emission in the 460-500 nm range. However, all spectra of PSiC show increased PL emission below 500 nm. In some samples (Fig. 3.4, *top*) this increased emission is pronounced with an unresolved emission band peaking in the 440-460 nm region. Changes in the PL of the broad visible band are observed, too. As shown in Fig. 3.4 the wavelength of maximum emission in PL blue-shifts 8-20 nm in the porous material.

3.3.2 Anodically Etched SiC

The PL spectra collected from anodically etched PSiC shows wide variation in the wavelength of maximum emission (Fig. 3.5). However, in contrast to the CL spectra, maximum PL emission is always sub-bandgap in energy. Maximum PL emission occurs anywhere from 550 nm (near the N^--B^+ recombination peak) to 430 nm (near bandgap emission). Low power density (15 mW/mm^2) was utilized to collect the spectra, ensuring that the high energy peaks really are due to PL and not bandgap emission. No apparent relation between anodization voltage/current and resulting PL emission was observed, in contrast to some results in the literature.[18,23]

Because the emission in this spectral region is below the bandgap energy, the most likely source of luminescence is band-tail states,[22] the blue shift upon etching signifying a shift in the distribution of such states. When the power of the excitation laser was decreased, the maximum PL emission from
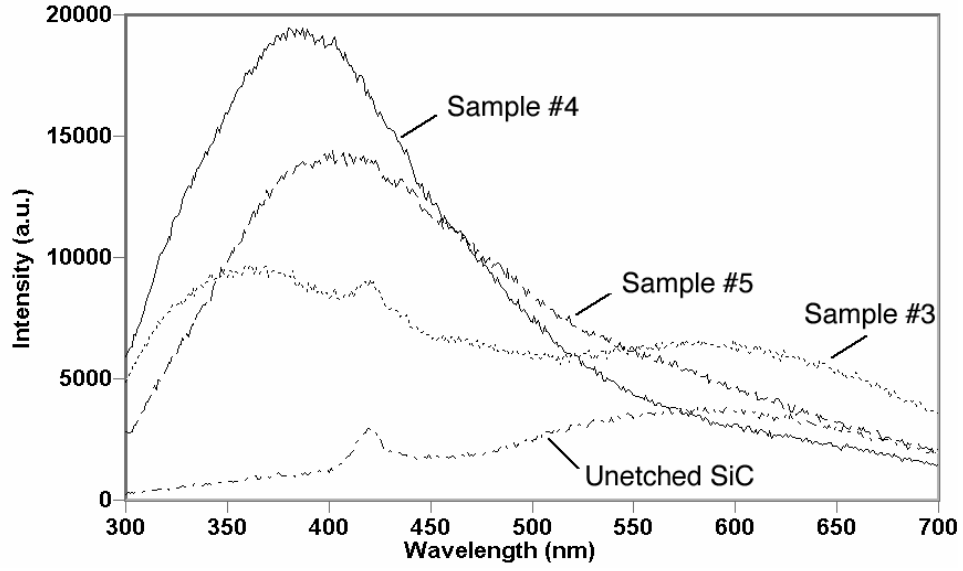
Figure 3.3. Cathodoluminescence spectra of unetched 6H-SiC and three different pieces of PSiC prepared from n-type 6H-SiC by anodic etching for 40 min. Sample numbers correspond to the notation given in Table 2.1 of Chapter 2.
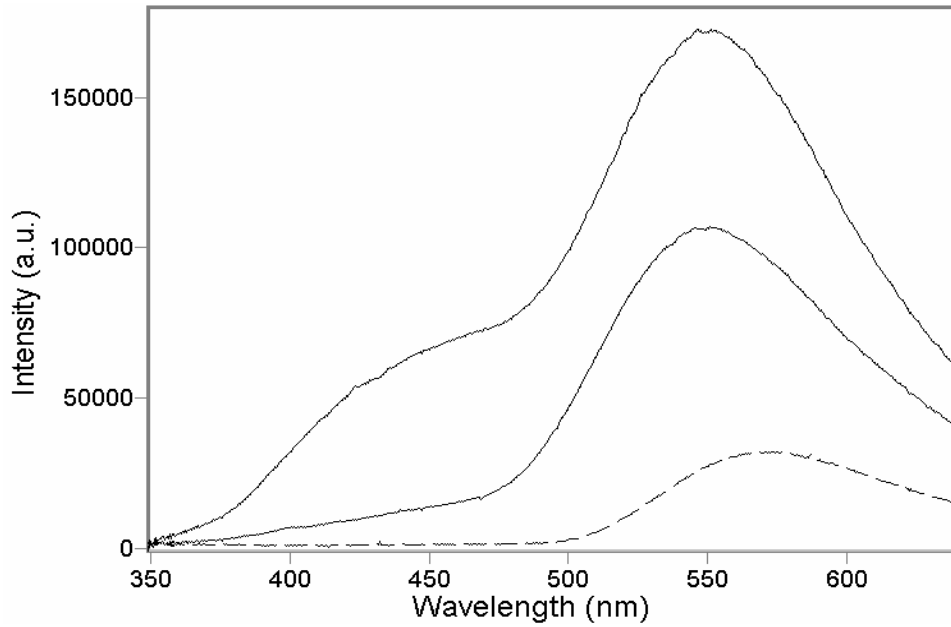
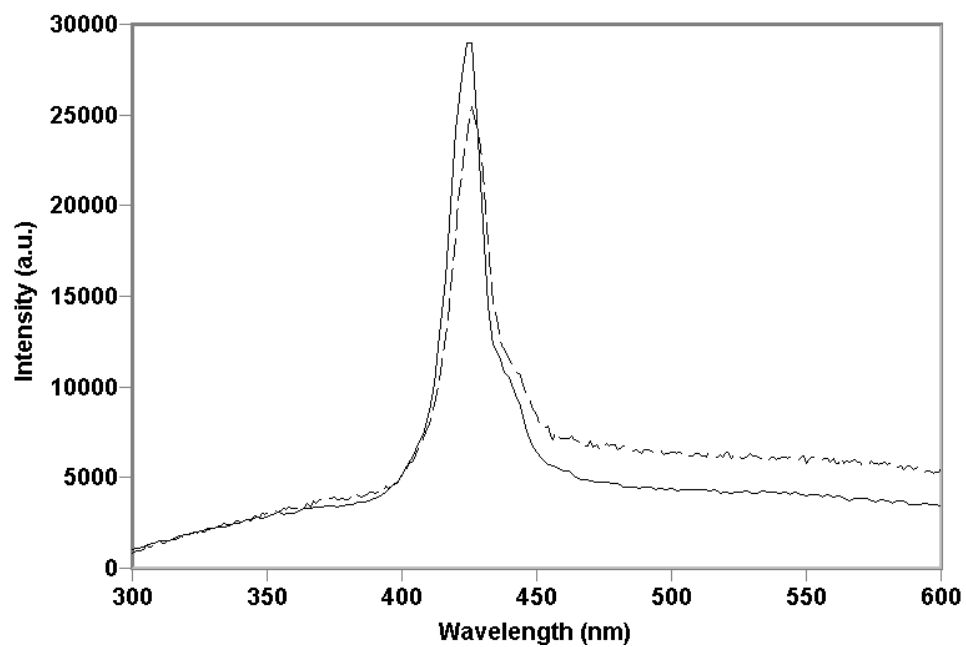Figure 3.4. Photoluminescence spectra of unetched 6H-SiC (dashed line) and two pieces of PSiC prepared from n-type 6H-SiC via electroless etching in dilute HF etchant for 60 min.
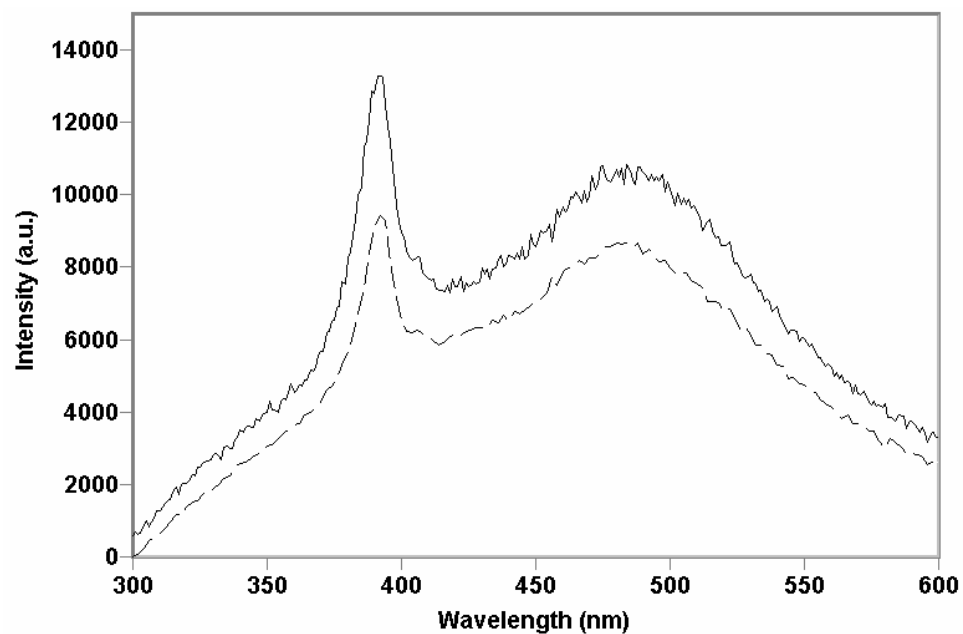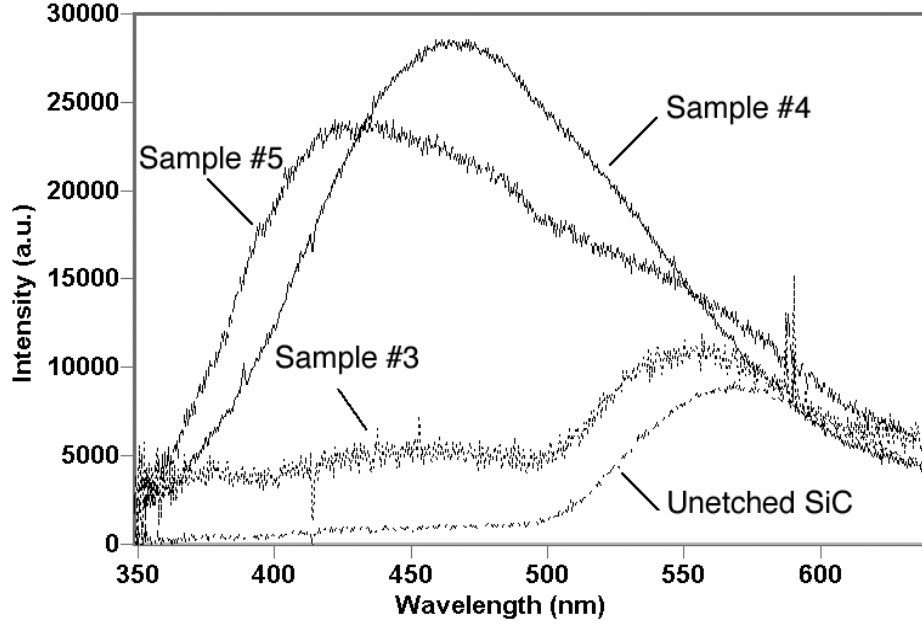
Figure 3.5. Photoluminescence spectra of unetched 6H-SiC and three different samples of PSiC prepared from n-type 6H-SiC via anodic etching for 40 min. Sample numbers correspond to the notation given in Table 2.1 of Chapter 2.

sample #3 was found to blue shift. This strongly suggests that the maximum PL emission for this piece of PSiC arises from donor-acceptor recombination.[53,54] However, the wavelength of maximum emission from sample #4 does not shift as the power of the excitation laser beam is varied. One possible conclusion is that the spectrum from sample #4 is dominated by defect emission.

The PL data collected with 325 nm excitation give broad emission, which tail into the UV, but they do not show the UV-dominated emission seen in the CL spectra. The differences in the PL and CL spectra are probably not a result of different probe depths, because the CL and PL sample similar volumes (3.6 μm deep in CL vs. 4.3 μm deep in PL). This suggests that the high energy electrons and photons used in CL and PL respectively access different emissive states. For example, the UV emission witnessed in CL may be some type of defect state that is accessed by the 20 kV electrons utilized in CL, but the state cannot be accessed by the 4 eV photons used to collect the PL spectra.

3.4 Raman Spectra

Raman spectra were excited at three different wavelengths. Initially, spectra were excited with sub-bandgap radiation (Ar$^+$ laser, $\lambda = 457.9$ nm) and collected on a single monochromator (Spex 500M, 1200 groove/mm grating) equipped with a liquid N_2 cooled charge coupled device (CCD) camera (Photometrics Ltd.). A holographic notch filter (Kaiser) was used to remove scattered laser line from the Raman scattered radiation (Fig. 3.6). This wavelength was used to map the polytype of the 4H-SiC wafer as well as initially characterize the porous layers.

Later, Raman spectra were excited with a HeCd laser operating at 441.6 nm as well as a different HeCd laser emitting at 325.0 nm. The sub-bandgap 441.6 nm excitation samples the entire wafer thickness,[55] so data from these experiments reflect the properties of the PSiC film as well as the crystalline SiC substrate. Laser excitation at 325.0 nm (above bandgap energy) was utilized in order to probe the near-surface region of the wafer preferentially, as this wavelength has a probe depth of ~4.3 μm.[56] These Raman spectra were collected with a triple spectrometer (Spex 1877, 0.6 m) with two 2400 groove/mm gratings in the filter stage, a 2400 groove/mm grating in the spectrograph stage, and a UV-sensitive CCD camera (Roper Scientific) (Fig. 3.7). In SiC, the A_1 LO mode at 966 cm^{-1} is a polar mode in C_{6v} symmetry and, thus, couples very strongly to the macroscopic electric field accompanying the LO phonon, distorting its intensity relative to the TO modes when above-bandgap excitation is used.[47,57,58] It is the LO mode, then, that was primarily monitored for changes indicative of quantum confinement effects.

3.4.1 Electrolessly Etched SiC

Initially spectra were excited at 457.9 nm, and this wavelength provides a strong signal from the PSiC wafer. The spectra are dominated by the expected optic branch phonons allowed in backscattering along the z-axis (A_1 LO and E_2 TO) (Figs. 3.8 and 3.9). Because the laser energy is sub-bandgap, the signal originates from the crystalline SiC substrate as well as the much thinner PSiC layer, making the spectra of the etched and unetched samples indistinguishable.
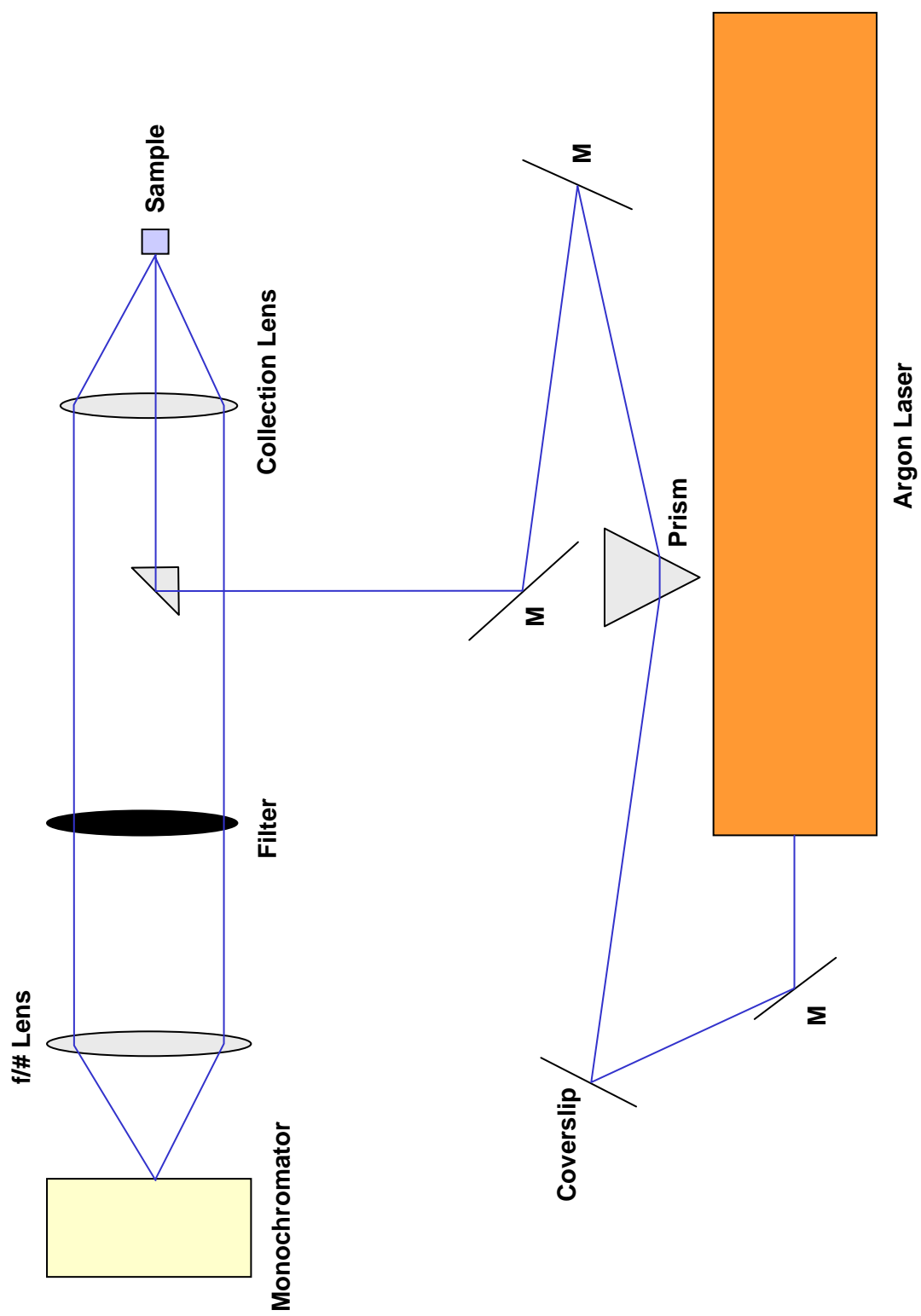
Figure 3.6. Experimental arrangement for visible Raman collection at 457.9 nm.
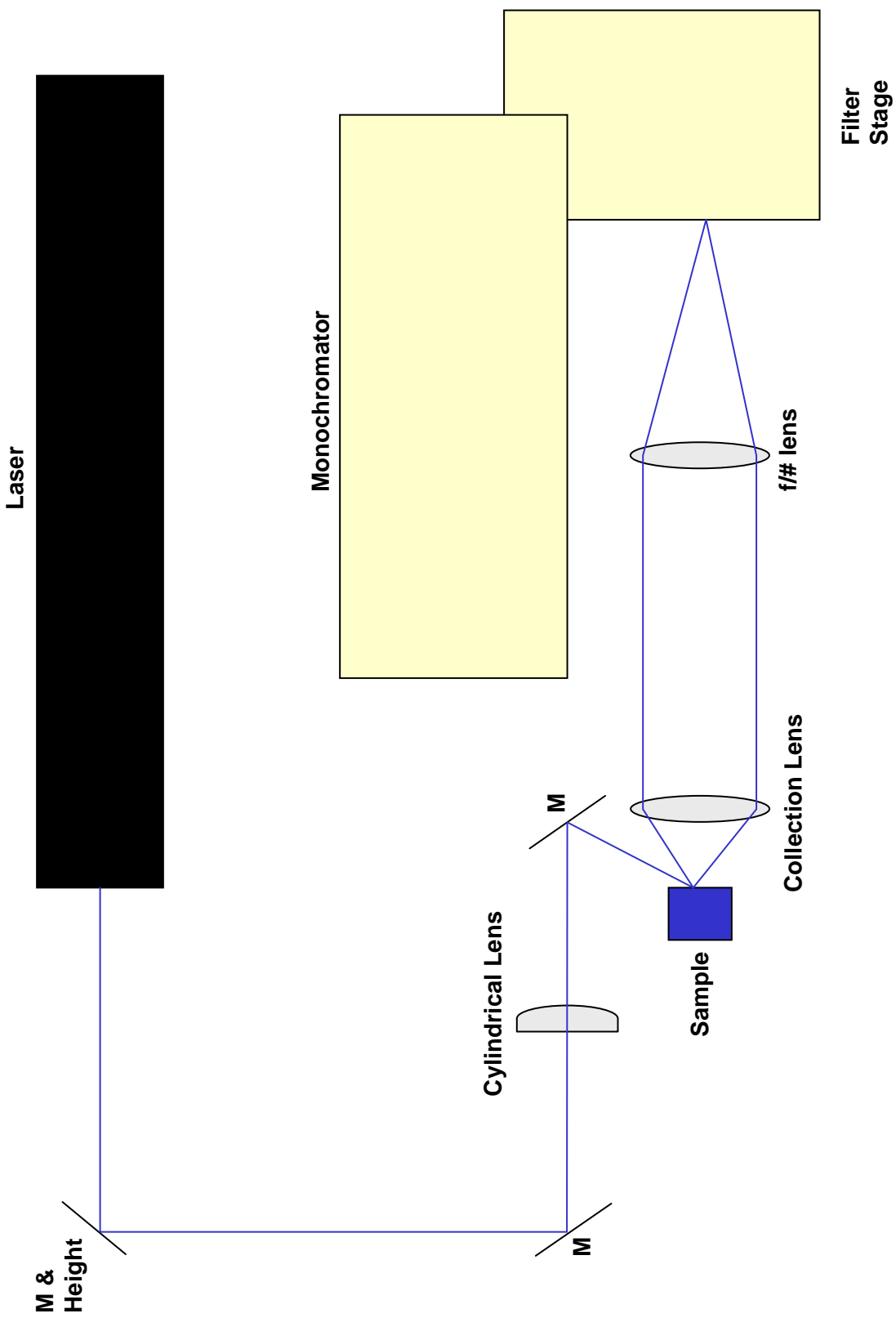
Figure 3.7. Experimental arrangement for UV Raman and PL collection.

Laser

Monochromator

Filter
Stage

f/# lens

Collection Lens

M

Cylindrical Lens

Sample

M

M &
Height
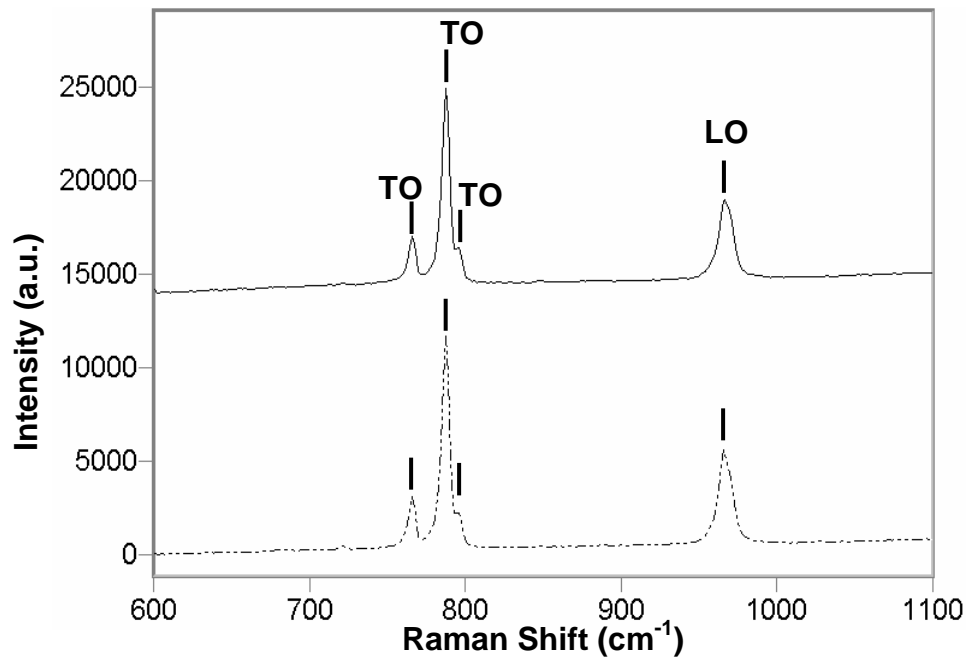
Figure 3.8. Unpolarized Raman spectra of etched (top, solid) and unetched (bottom, dashed) 6H-SiC in the backscattering configuration excited at 457.9 nm.
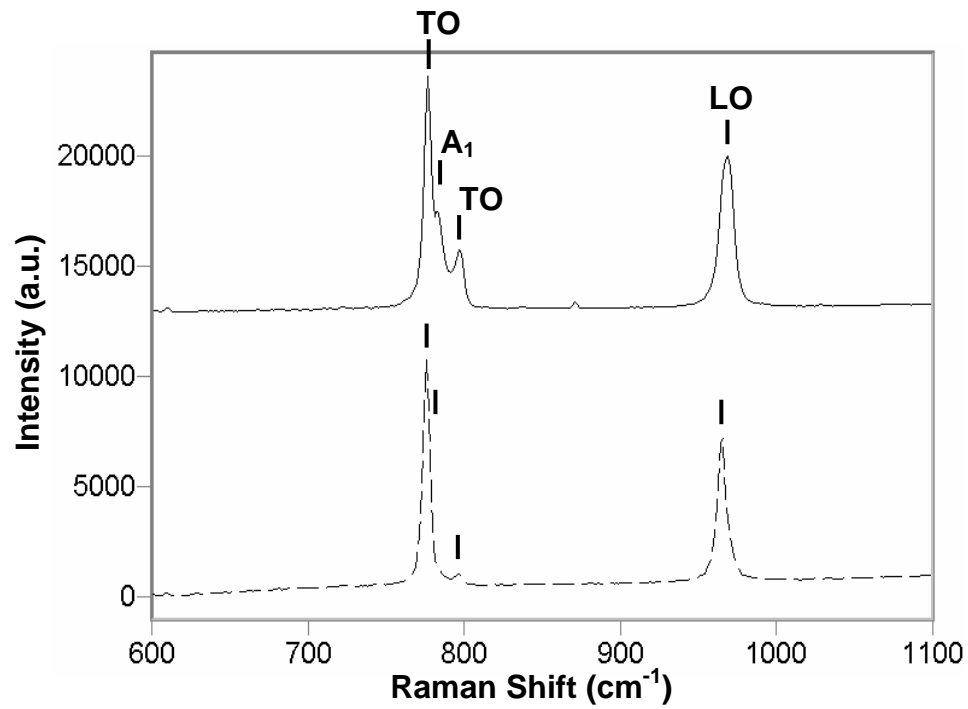
Figure 3.9. Unpolarized Raman spectra of etched (top, solid) and unetched (bottom, dashed) 4H-SiC in the backscattering configuration excited at 457.9 nm.

The 457.9 nm excitation was useful for determining the polytype in the nominally 4H-SiC wafer. CL measurements had shown that some portions of the 4H-SiC wafer exhibited bandgap values indicative of the 6H polytype. Therefore, Raman spectra were collected at 75 different points over the surface of the 2" wafer in order to map the different polytypes within the wafer. Raman mapping showed that a majority of the wafer was 4H, although significant portions of 6H material existed (Fig. 3.10). The interfaces between the 4H and 6H regions often showed characteristics of each polytype when examined via Raman spectroscopy (Fig. 3.11). The 6H wafer was also mapped and found to be all 6H in polytype.

It is interesting that the Raman modes in Fig. 3.11 show peak locations between that of pure 4H and pure 6H character, given the definite interface seen between the two polytypes in cross-sectional SEM (Fig 2.27). The Raman results clearly indicate a strained interface that would not be apparent from the SEM images alone.

Subsequent to the 457.9 nm Raman studies, an improved optical system was constructed within our laboratory. Initially, Raman spectra were again collected with sub-bandgap excitation (441.6 nm, HeCd laser) in order to analyze the spectra with improved resolution. However, once again no broadening of the modes was witnessed for the porous SiC samples.

To circumvent problems with penetration depth, Raman data were then collected with 325.0 nm excitation, a photon energy significantly above the 300 K bandgap energy. This above-bandgap laser line probes a much smaller volume of the PSiC at the expense of lower signal strength. However, even with 325.0 nm excitation, the LO mode was not found to shift or broaden with the development of porosity. The lack of change in the LO lineshape with etching means that either phonon confinement effects are inherently small in electrolessly etched PSiC, or the fraction of unit cells sampled for which confinement effects are important is small. Additionally these results point to the extreme stability of PSiC, and indicate that the porous layer does not introduce significant strain.

Unfortunately, while collecting Raman data with the 325 nm laser only, a "band" always appears near 854 cm^{-1}. The cause of this band is unknown, since it does not equate to any mode in our polytypes of SiC (or a multiple of a mode). It also does not correspond to any expected unwanted emission from the
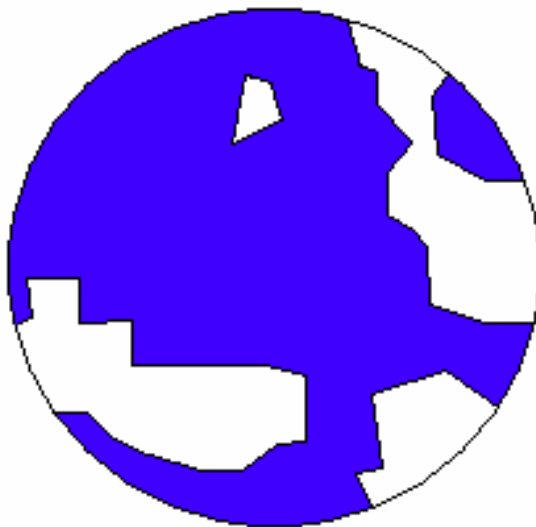
Figure 3.10. Polytype map of the 2" diameter wafer that was purchased as pure 4H-SiC. The blue regions were found to be 4H-SiC; the white regions were found to be 6H-SiC.
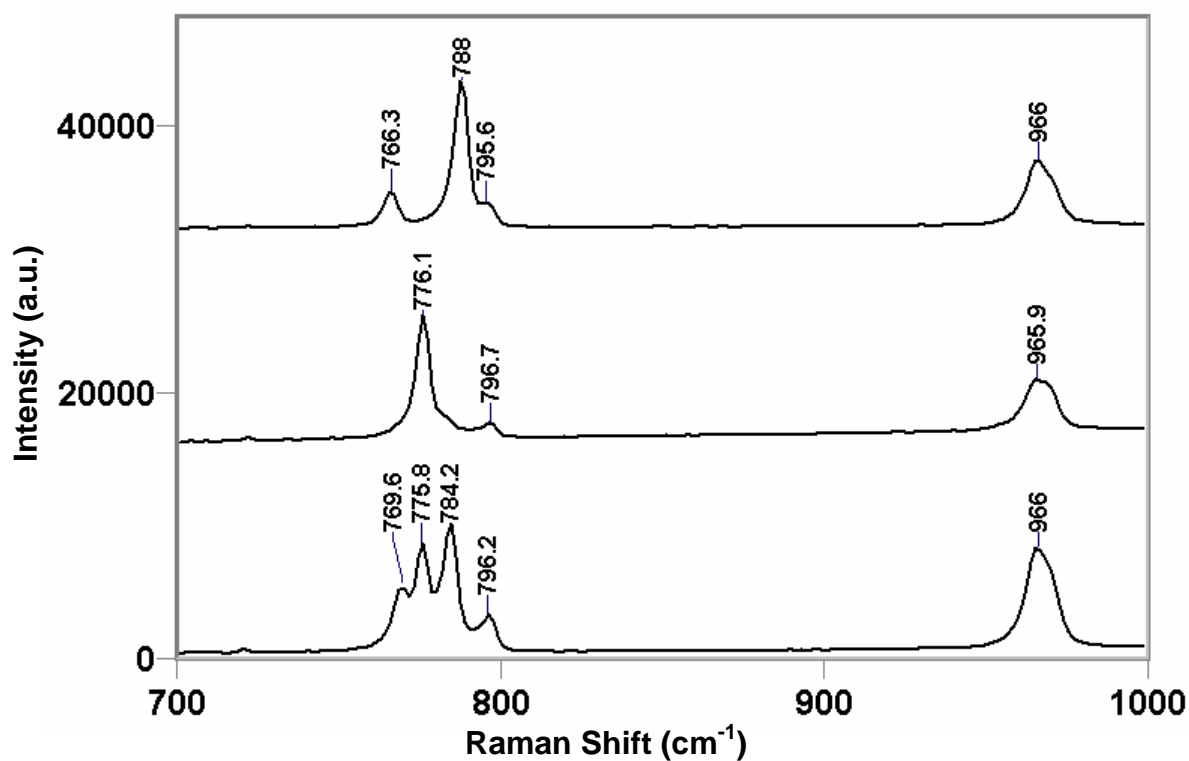
Figure 3.11. Unpolarized Raman spectra of pure 6H-SiC (top), pure 4H-SiC (middle), and a wafer that has both polytypes present (bottom). The spectra were excited at 457.9 nm and collected in the backscattering configuration.

HeCd laser, and the use of two prisms in the optical system did not remove this line. The 854 cm^{-1} band could originate from the 15R polytype of SiC, but this explanation seems improbable, since no other evidence for the 15R polytype was observed. The 854 cm^{-1} band is most likely a spectral artifact from the 1200 groove/mm gratings, and therefore unfortunately appears in all 325 nm Raman spectra presented in this work.

3.4.2 Anodically Etched SiC

Raman spectra collected with 441.6 nm excitation (sub-bandgap) were unchanged between the crystalline SiC substrate and the anodically etched PSiC layers. However, Raman spectra collected with 325 nm excitation (above bandgap) showed broadening of the longitudinal optic (LO) mode to lower wavenumbers; the degree of broadening varied greatly between samples (Fig. 3.12). The peak in the LO Raman band in PSiC showed little (< 3 cm^{-1}) or no shifting to lower wavenumbers.

Similar broadening has been reported by other authors in PSiC[18,26] and attributed to confinement effects. One model used to describe Raman lineshapes[38,39] is

$$I(\omega) \propto \int_0^1 \frac{e^{\frac{-q^2 L^2}{4a^2}}}{[\omega - \omega(q)]^2 + \left(\frac{\Gamma_o}{2}\right)^2} \, d^3q. \tag{3.1}$$

The model in Eq. 3.1 assumes spherical nanocrystallites of diameter L. In Eq. 3.1, ω is the Raman frequency, q is the Brillouin zone dimension ($2\pi/a$, where $a = 1.5117$ nm for 6H-SiC), and Γ_o is the line width of the crystalline material. $\omega(q)$ is the phonon dispersion relation, for which we used

$$\omega^2(q) = 657,500 + 270,000 \cos\left(\frac{\pi q}{2}\right). \tag{3.2}$$

This phonon dispersion relation was chosen after fitting the phonon dispersion curve for all of the SiC polytypes to a best-fit function (Fig. 3.13).[47,58-64]

A Mathematica program was written by Dr. Lindesay at Howard University in order to fit the model given in Eq. 3.1 to the experimental data (see Appendix A). Fitting Eq. 3.1 to our Raman spectra

predicts nanocrystallite diameters ranging from 6-25 nm. However, the theoretical line shapes do not fit the experimental data well (Fig. 3.14). Eq. 3.1 predicts that broadening of the LO mode should be accompanied by a significant shift in the peak location of the LO mode to lower wavenumbers. However, as seen in Fig. 3.12, significant broadening of the LO mode is accompanied by only relatively small shifts to lower wavenumbers.

Therefore, a bimodal fit was implemented in an attempt to account for the sampling of some large crystallites (effectively bulk SiC) as well as nanocrystallites of some small, average diameter. Again, the experimental LO mode is too broad to be effectively represented by only a bimodal distribution of nanocrystalline sizes (Fig. 3.15). In actuality, of course, the PSiC layers are probably composed of a continuum of nanocrystallite sizes, and the Raman spectra would be best fit by a wide distribution of sizes, if, in fact, phonon confinement is the cause of the LO mode broadening. However, even when including nanocrystallite dimensions on the order of just a few atoms in diameter, the quantum confinement equation cannot properly model the wide broadening seen in the experimental Raman spectra.

Another possible explanation for the broadening of the Raman LO mode in polar materials, such as PSiC, is the emergence of surface Fröhlich modes. Literature reports of PSiC LO mode broadening [26] very similar to the results found in this work have been attributed to the longitudinal-transverse splitting of a Fröhlich mode.[65] Fröhlich-type modes have been reported in porous GaN;[57] in addition, LO mode broadening attributed to surface phonons has been found in GaP microcrystals[66] and porous GaP.[67] Finally, infrared reflectance spectra of PSiC films also show indications of surface phonon modes.[68]

The Raman spectra in this work were fit to a bimodal Gaussian distribution consisting of the bulk SiC LO phonon plus a peak due to the surface Fröhlich modes. Following the model of Sarua et. al.,[65] the broadening of the LO mode in PSiC was assumed to be due to the combinatorial effect of extraordinary LO modes, longitudinal Fröhlich modes, and transverse Fröhlich modes. The intensities from these three types of modes were weighted for the orientation of the incident laser beam used in this work. The results of this model must be used with caution; in our case, the model yields information of a qualitative nature
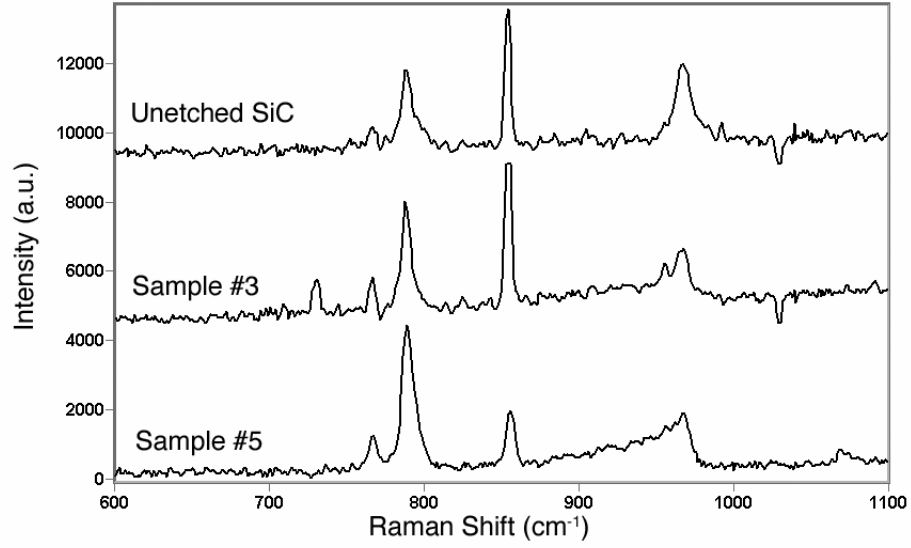
Figure 3.12. Unpolarized Raman spectra (collected at 325.0 nm) of unetched 6H-SiC (top) and two pieces of PSiC prepared via anodic etching for 40 min. The spectra were excited at 325.0 nm and collected in the backscattering configuration.
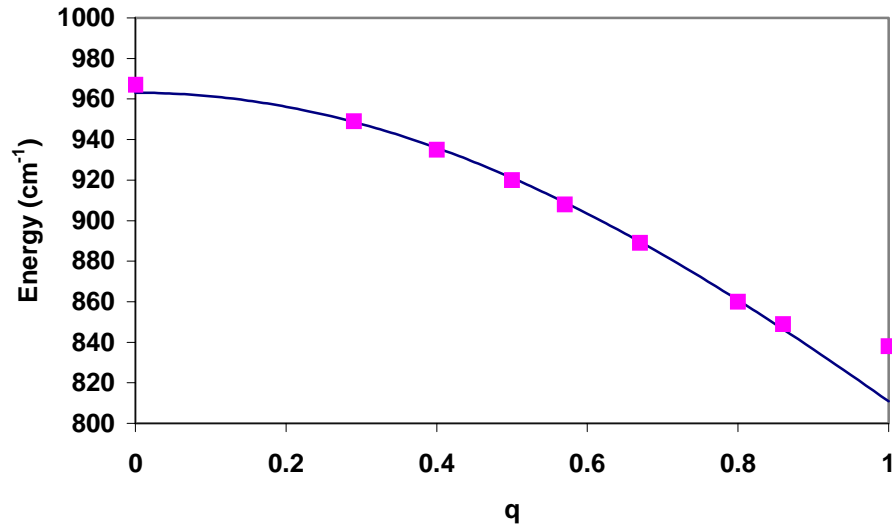
Figure 3.13. Dispersion curve in the ΓL direction for SiC showing the experimentally determined LO modes found in the literature (points) and the best fit line in accordance with Eq. 3.2.
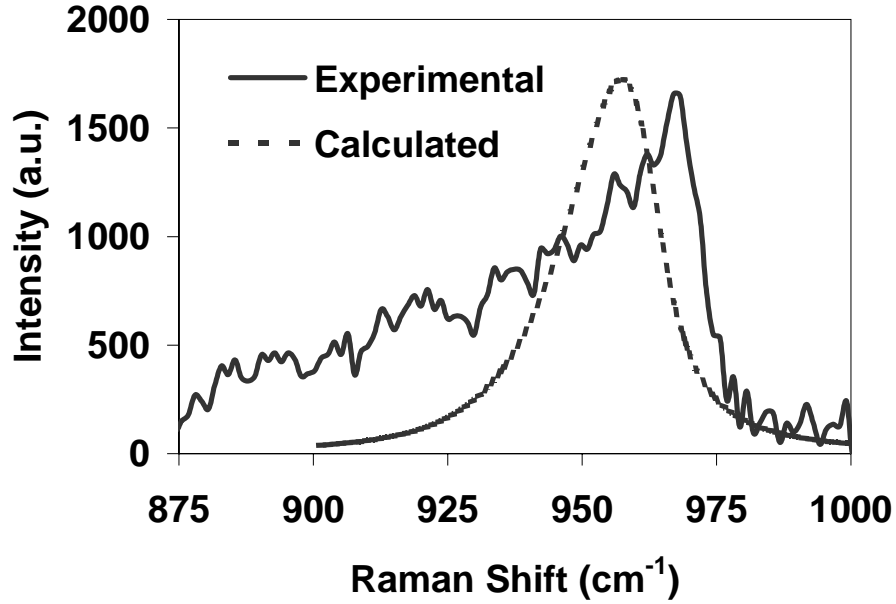
Figure 3.14. Quantum confinement model fit (dashed) compared to the experimentally-determined LO mode (solid) for an anodically etched piece of 6H-SiC (sample #5).
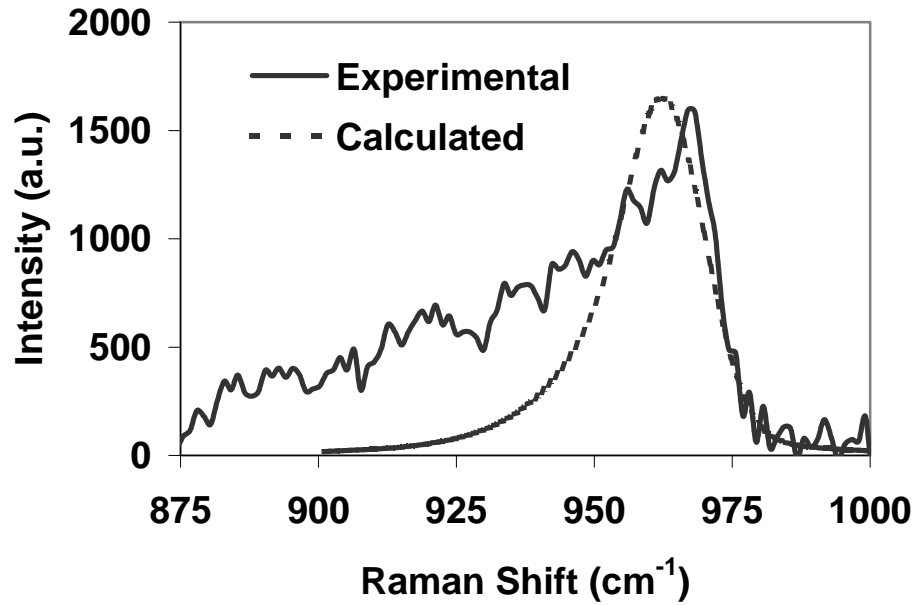
Figure 3.15. Experimentally-determined LO mode (solid) for an anodically etched piece of 6H-SiC (sample #5) compared to the theoretical curve combining a Gaussian curve for crystalline 6H-SiC combined with a quantum confinement peak (dashed).

at best. The properties of Fröhlich modes strongly depend upon the morphology (symmetry, structural geometry, effective size, etc.) and on the properties of the constituents. The model assumes the porous material is columnar in structure; however, as our SEM images show, our porous material is not as columnar as, for example, porous GaN. In addition, this model uses an effective medium approximation, which is not strictly valid for our spectra, since the wavelength of the laser is only moderately greater than the dimensions of the porous material. As a result, we can expect that our Raman spectra include the effects of strong diffuse scattering, accompanied by a broadening of spectral lines and violation of the symmetry selection rules.

Following the model of Sarua et. al.,[65] the total Fröhlich mode was assumed to be composed of three distinct components: a longitudinal Fröhlich character, a transverse Fröhlich character, and extraordinary LO modes. The longitudinal Fröhlich and extraordinary LO modes have symmetry along the c-axis of the crystal; the transverse Fröhlich mode is in the plane of the crystal. Therefore, first the angle of incidence of our excitation beam had to be measured to deduce the relative contribution of each mode; it was assumed that the three modes listed above would have equal intensity contributions to the total Fröhlich mode before weighting for orientation. For our geometry the longitudinal Fröhlich and extraordinary LO modes were given weights of 42.9% each, and the transverse Fröhlich mode was given a weight of 14.2%.

The dielectric constant of the semiconducting skeleton was calculated for 700 cm^{-1} < ω < 1000 cm^{-1} according to

$$\varepsilon(\omega) = \varepsilon_\infty \left(1 + \frac{\omega_{LO}^2 - \omega_{TO}^2}{\omega_{TO}^2 - \omega^2} \right).$$

(3.3)

ε_∞ was assigned a value of 8.422 for our excitation wavelength;[56] ω_{LO} and ω_{TO} are the experimentally determined longitudinal optic mode and transverse optic mode, respectively. Eq. 3.3 assumes vanishingly small phonon damping. The plot of Eq. 3.3 for anodically etched sample #5 is shown in Fig. 3.16. For this sample, the TO phonon at 788.9 cm^{-1} and the LO phonon at 964.9 cm^{-1} can be seen, represented by a pole (TO phonon) and a zero (LO phonon).

Next, $\varepsilon_{\parallel}$, the dielectric function component parallel to the pores, was calculated according to

$$\varepsilon_{\parallel}(\omega) = c\varepsilon(\omega) + (1-c)\varepsilon_o. \tag{3.4}$$

c is the fraction of crystalline skeleton remaining after etching. The use of Eq. 3.4 to determine an appropriate value for c will be discussed below. ε_o is the dielectric constant of air (1.00), since air fills the pores during our measurements. Eq. 3.4 yields a plot given in Fig. 3.17. In plots of $\varepsilon(\omega)$, the poles correspond to modes of transverse character, and the zeros correspond to longitudinal modes. Therefore, in Fig. 3.17, one sees a TO mode at 788.9 cm^{-1} and a zero at 948 cm^{-1} which for this plot corresponds to extraordinary LO phonons.

Finally, $\varepsilon_{\perp}$, the electric field component perpendicular to the pore direction, was calculated via

$$\varepsilon_{\perp}(\omega) = \varepsilon(\omega)\frac{(2-c)\varepsilon_o + c\varepsilon(\omega)}{c\varepsilon_o + (2-c)\varepsilon(\omega)}. \tag{3.5}$$

Eq. 3.5 yields two poles and two zeros, as shown in Fig. 3.18. The pole at 788.9 cm^{-1} corresponds to the TO phonon mode; the zero at 923 cm^{-1} corresponds to the longitudinal Fröhlich excitation; the pole at 958 cm^{-1} is the transverse Fröhlich excitation; and finally, the zero at 964.9 cm^{-1} is the LO phonon mode.

The experimental Raman spectrum was fit with two Gaussian peaks, one Gaussian representing the crystalline SiC and the other Gaussian peak the cumulative Fröhlich mode contribution. The wavenumber for the Gaussian peak representing the cumulative Fröhlich mode contribution was noted. Then, the value for c in Eq. 3.4 and Eq. 3.5 was chosen such that the weighted contributions from the extraordinary LO phonon mode peak (Eq. 3.4), the longitudinal Fröhlich excitation peak (Eq. 3.5), and the transverse Fröhlich excitation peak (Eq. 3.5) added together matched the Gaussian peak value found to represent the cumulative Fröhlich mode contribution.

An appropriate standard deviation was determined for the three individual Fröhlich mode Gaussian peaks. In Fig. 3.19, σ was assigned a value of 50 to properly reflect the broad Fröhlich mode of the experimental data. The three individual Gaussian peak contributions were added together and
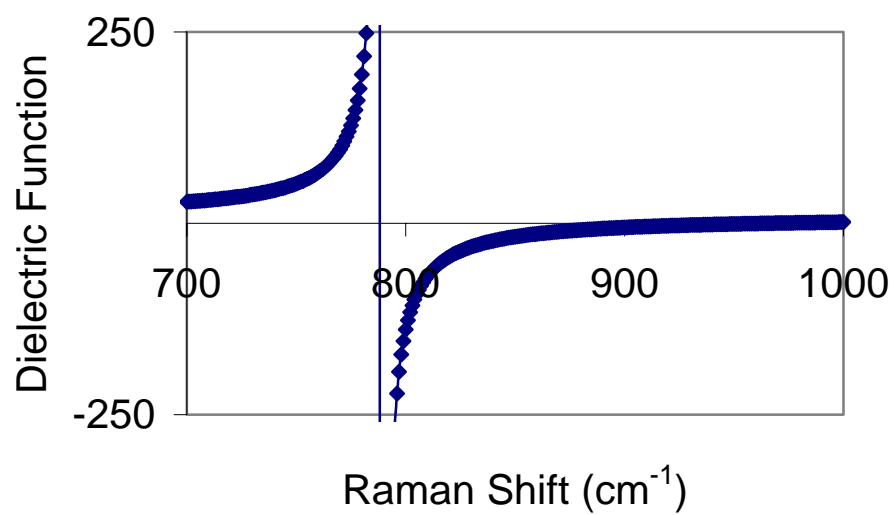
Figure 3.16. Plot of Eq. 3.3 for sample #5.
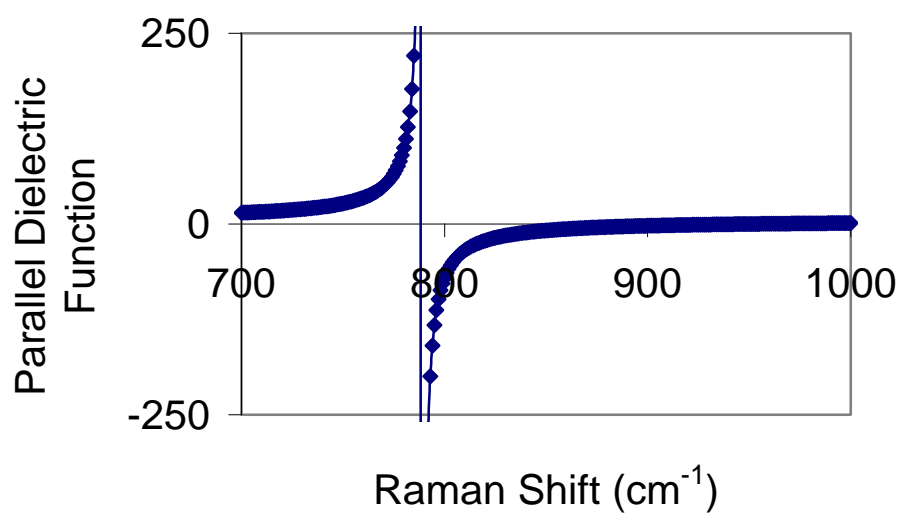
Figure 3.17. Plot of Eq. 3.4 for sample #5.
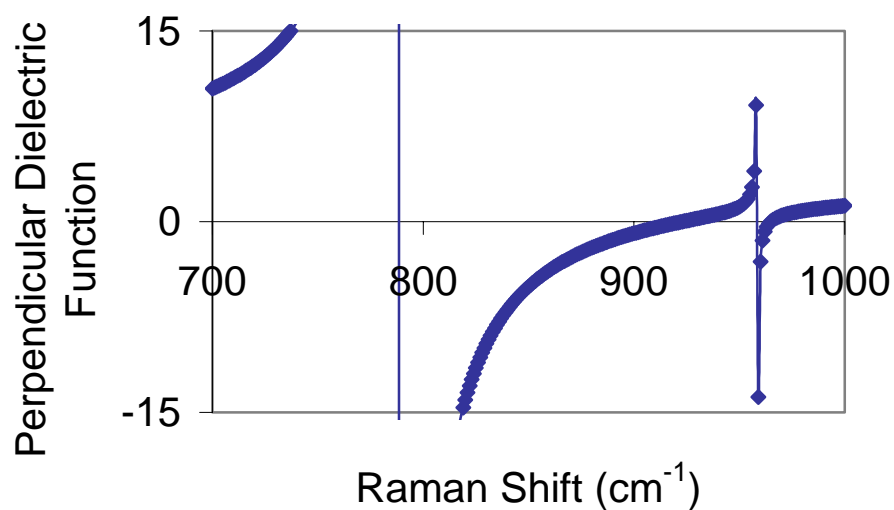
Figure 3.18. Plot of Eq. 3.5 for sample #5.
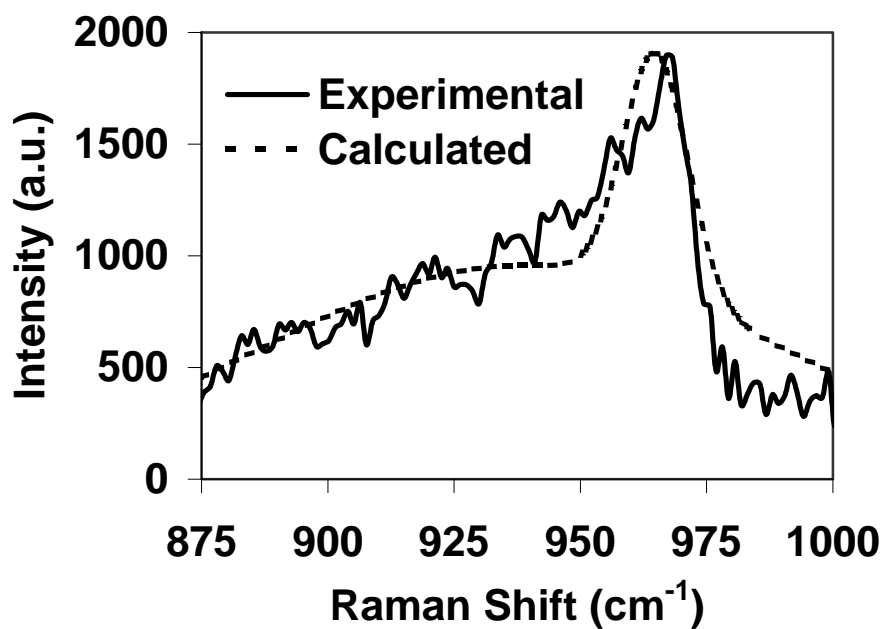
Figure 3.19. Experimentally-determined LO mode for a sample of anodically-etched PSiC (solid) compared to the theoretical curve composed of Fröhlich mode interactions combined with a Gaussian for crystalline 6H-SiC (dashed). Data is for sample #5.

combined with a Gaussian peak for the crystalline SiC to form a calculated Raman spectrum for our PSiC samples (Fig. 3.19). Fröhlich mode fitting parameters are shown in Table 3.1.

In general, good fits were obtained from the bimodal Gaussian distribution, and Fröhlich modes appear to be the leading cause of the LO mode broadening witnessed in this work. However, for the best Gaussian fits, standard deviations of 50 or greater had to be used for the Fröhlich modes.

Table 3.1. Fröhlich Mode Fitting Parameters

Sample #	Fröhlich Mode Peak (cm^{-1})	Width (cm^{-1})
1	949.9	71
2	934.9	56
3	955.4	79
4	939.4	45
5	941.9	57
6	938.7	51

3.5 Conclusions

PSiC produced via the electroless etching technique does not show significant changes in the Raman spectrum or cathodoluminescent emission. However, spectroscopic evidence of the morphological changes in the near-surface region is observed in the blue-shift of sub-bandgap photoluminescent emission. Taken as a whole, these observations do not bode well as far as producing PSiC LEDs.

The spectroscopic behavior of the anodically etched PSiC differed greatly from the electroless material. Correlation between the Raman, PL, and CL behavior is evident in the anodically etched material. The PSiC wafers that yield the greatest broadening of the Raman LO mode also yield the largest blue shifts in the peak PL emission. This is similar to what has been reported for porous GaP.[69] In addition, these pieces emit the most intense CL signal, but the peak CL in these pieces is relatively red compared to the other porous samples. The increase in UV CL emission appears to be accompanied by a loss of emission in the peak at 590 nm (donor-acceptor recombination), indicating a possible shift by electrons from one form of excited energy state to another.

A few results in this work are consistent with a quantum confinement explanation for the trends in CL/PL/Raman behavior. First, CL peaks that are bluer than bandgap indicate the possibility of quantum wells. Also, the variability in the wavelength of maximum CL emission points to a tunability that could be dependent upon nanocrystallite size. In addition, the broadest Raman LO modes (possibly an indication of phonon quantum confinement) correspond to the samples that are dominated by UV CL emission, with a loss of bandgap and donor-acceptor recombination peaks in the CL spectra.

However, other results in this work argue against quantum confinement. First, in all samples, the Raman LO mode is still dominated by a peak that is unmoved from its position in crystalline SiC. This indicates that the great majority of the PSiC layer is composed of crystallites too large to exhibit a quantum confinement effect. Also, fitting of the Raman spectra indicate a Fröhlich mode effect that cannot be represented well by mathematical descriptions of phonon quantum confinement. Next, the Raman spectra fits yielding the smallest nanocrystallite sizes actually correspond to the pieces with the smallest blue shifts in CL emission. In addition, PL spectra never indicate a UV peak as was seen in CL measurements. Finally, SEM images do not seem to indicate the formation of numerous nanocrystallites that are actually small enough to produce quantum confinement effects. Taken as a whole, the spectroscopic results (especially the fitting of Raman broadening with Fröhlich mode models) indicate that features of the anodically etched porous surface (such as surface effects/species or defects) are most likely responsible for the UV cathodoluminescent emission witnessed in this work.

Unlike PSi the Raman, PL, and CL spectra of PSiC are stable indefinitely upon storage in the laboratory ambient, suggesting electrolessly etched PSiC is more robust than PSi and therefore more suitable for applications in hostile environments. For this reason, the chemical and temperature sensing capabilities of PSiC were examined in the remainder of this work.

3.6 References

(1)   Canham, L. T. *Appl. Phys. Lett.* **1990**, *57*, 1046.

(2)   Chattopadhyay, S.; Li, X.; Bohn, P. W. *J. Appl. Phys.* **2002**, *91*, 6134.

(3)   Lockwood, D. J.; Aers, G. C.; Allard, L. B.; Bryskiewicz, B.; Charbonneau, S.; Houghton, D. C.; McCaffrey, J. P.; Wang, A. *Can. J. Phys.* **1992**, *70*, 1184.

(4)   Hamilton, B. *Semicond. Sci. Technol.* **1995**, *10*, 1187.

(5)   Zhang, Q.; Bayliss, S. C. *J. Appl. Phys.* **1996**, *79*, 1351.

(6)   Fauchet, P. M.; Tsybeskov, L.; Peng, C.; Duttagupta, S. P.; von Behren, J.; Kostoulas, Y.; Vandyshev, J. M. V.; Hirschman, K. D. *IEEE J. Quantum Electron.* **1995**, *1*, 1126.

(7)   Hirschman, K. D.; Tsybeskov, L.; Duttagupta, S. P.; Fauchet, P. M. *Nature* **1996**, *384*, 338.

(8)   Mimura, H.; Matsumoto, T.; Kanemitsu, Y. *Appl. Phys. Lett.* **1994**, *65*, 3350.

(9)   Li, N.; Wu, X.; Liao, L.; Bao, X. *Nucl. Instrum. Methods B* **1998**, *142*, 308.

(10)   Mimura, H.; Matsumoto, T.; Kanemitsu, Y. *J. Non-Cryst. Solids* **1996**, *198-200*, 961.

(11)   Mimura, H.; Matsumoto, T.; Kanemitsu, Y. *Solid State Electron.* **1996**, *40*, 501.

(12)   Shor, J. S.; Bemis, L.; Kurtz, A. D.; Macmilan, M.; Choyke, W. J.; Grimberg, I.; Weiss, B. Z. *Inst. Phys. Conf. Ser.* **1993**, *137*, 193.

(13)   Shor, J. S.; Bemis, L.; Kurtz, A. D.; Grimberg, I.; Weiss, B. Z.; MacMillan, M. F.; Choyke, W. J. *J. Appl. Phys.* **1994**, *76*, 4045.

(14)   Danishevskii, A. M.; Zamoryanskaya, M. V.; Sitnikova, A. A.; Shuman, V. B.; Suvorova, A. A. *Semicond. Sci. Technol.* **1998**, *13*, 1111.

(15)   Petrova-Koch, V.; Sreseli, O.; Polisski, G.; Kovalev, D.; Muschik, T.; Koch, F. *Thin Solid Films* **1995**, *255*, 107.

(16)   Danishevskii, A. M.; Shuman, V. B.; Guk, E. G.; Rogachev, A. Y. *Semiconductors* **1997**, *31*, 354.

(17)   Shin, W.; Hikosaka, T.; Seo, W.; Ahn, H. S.; Sawaki, N.; Koumoto, K. *J. Electrochem. Soc.* **1998**, *145*, 2456.

(18)   Matsumoto, T.; Takahashi, J.; Tamaki, T.; Futagi, T.; Mimura, H.; Kanemitsu, Y. *Appl. Phys. Lett.* **1994**, *64*, 226.

(19)   Konstantinov, A. O.; Henry, A.; Harris, C. I.; Janzen, E. *Appl. Phys. Lett.* **1995**, *66*, 2250.

(20)   Spanier, J. E.; Cargill III, G. S.; Herman, I. P.; Kim, S.; Goldstein, D. R.; Kurtz, A. D.; Weiss, B. Z. *Mat. Res. Soc. Symp. Proc.* **1997**, *452*, 491.

(21)   Jessensky, O.; Muller, F.; Gosele, U. *Thin Solid Films* **1997**, *297*, 224.

(22)   Kim, S.; Spanier, J. E.; Herman, I. P. *Jpn. J. Appl. Phys.* **2000**, *39*, 5875.

(23)   Matsumoto, T.; Tamaki, T.; Futagi, T.; Mimura, H.; Kanemitsu, Y. *Mat. Res. Soc. Symp. Proc.* **1993**, *298*, 355.

(24)   Hassen, F.; M'Ghaieth, R.; Maaref, H.; Madar, R. *Mat. Sci. Engng. C* **2001**, *15*, 113.

(25)   Chen, Z. M.; Ma, J. P.; Yu, M. B.; Wang, J. N.; Ge, W. K.; Woo, P. W. *Mat. Sci. Engng. B* **2000**, *75*, 180.

(26)   Danishevskii, A. M.; Shuman, V. B.; Rogachev, A. Y.; Ivanov, P. A. *Semiconductors* **1995**, *29*, 1106.

(27)   Parkhutik, V. P.; Namavar, F.; Andrade, E. *Thin Solid Films* **1997**, *297*, 229.

(28)   Propst, E. K.; Kohl, P. A. *J. Electrochem. Soc.* **1994**, *141*, 1006.

(29)   Shin, W.; Seo, W.; Takai, O.; Koumoto, K. *J. Electron. Mater.* **1998**, *27*, 304.

(30)   Shin, W.; Murayama, N.; Seo, W.; Koumoto, K. *J. Korean Phys. Soc.* **1999**, *35*, S92.

(31)   Monguchi, T.; Fujioka, H.; Ono, K.; Oshima, M.; Serikawa, T.; Hayashi, T.; Horiuchi, K.; Yamashita, S.; Yoshii, K.; Baba, Y. *J. Electrochem. Soc.* **1998**, *145*, 2241.

(32)   Konstantinov, A. O.; Harris, C. I.; Janzen, E. *Appl. Phys. Lett.* **1994**, *65*, 2699.

(33)   Wang, J. N.; Chen, Z. M.; Woo, P. W.; Ge, W. K.; Wang, Y. Q.; Yu, M. B. *Appl. Phys. Lett.* **1999**, *74*, 923.

(34)   Deak, P.; Hajnal, Z.; Stutzmann, M.; Fuchs, H. D. *Thin Solid Films* **1995**, *255*, 241.

(35)   Delerue, C.; Lannoo, M.; Allan, G. *J. Lumin.* **1993**, *57*, 249.

(36)   Martin, E.; Delerue, C.; Allan, G.; Lannoo, M. *Phys. Rev. B* **1994**, *50*, 18258.

(37)   von Behren, J.; van Buuren, T.; Zacharias, M.; Chimowitz, E. H.; Fauchet, P. M. *Solid State Commun.* **1998**, *105*, 317.

(38)   Campbell, I. H.; Fauchet, P. M. *Solid State Commun.* **1986**, *58*, 739.

(39)   Richter, H.; Wang, Z. P.; Ley, L. *Solid State Commun.* **1981**, *39*, 625.

(40)   Gregora, I.; Champagnon, B.; Saviot, L.; Monin, Y. *Thin Solid Films* **1995**, *255*, 139.

(41)   Sui, Z.; Leong, P. P.; Herman, I. P.; Higashi, G. S.; Temkin, H. *Appl. Phys. Lett.* **1992**, *60*, 2086.

(42)   Xu, D.; Guo, G.; Gui, L.; Tang, Y.; Zhang, B. R.; Qin, G. G. *J. Phys. Chem. B* **1999**, *103*, 5468.

(43)   Burton, J. C.; Sun, L.; Pophristic, M.; Lukacs, S. J.; Long, F. H.; Feng, Z. C.; Ferguson, I. T. *J. Appl. Phys.* **1998**, *84*, 6268.

(44)   Vicente, P.; David, D.; Camassel, J. *Mat. Sci. Engng. B* **2001**, *B80*, 348.

(45)   Davydov, V. Y.; Averkiev, N. S.; Goncharuk, I. N.; Nelson, D. K.; Nikitina, I. P.; Polkovnikov, A. S.; Smirnov, A. N.; Jacobson, M. A.; Semchinova, O. K. *J. Appl. Phys.* **1997**, *82*, 5097.

(46)   Falkovsky, L. A.; Bluet, J. M.; Camassel, J. *Phys. Rev. B* **1998**, *57*, 11283.

(47)   Nakashima, S.; Harima, H. *Phys. Stat. Sol. A* **1997**, *162*, 39.

(48)   Salvador, G.; Sherman, W. F. *J. Mol. Struct.* **1991**, *247*, 373.

(49)   Kanaya, K.; Okayama, S. *J. Phys. D: Appl. Phys.* **1972**, *5*, 43.

(50)   Yacobi, B. G.; Holt, D. B. *Cathodoluminescence Microscopy of Inorganic Solids*; Plenum Press: New York, 1990.

(51)   Toth, M.; Phillips, M. R. *Scanning* **1998**, *20,* 425.

(52)   Fleischer, K.; Toth, M.; Phillips, M. R.; Zou, J.; Li, G.; Chua, S. J. *Appl. Phys. Lett.* **1999**, *74*, 1114.

(53)   Bebb, H. B.; Williams, E. W. "Photoluminescence I: Theory." In *Semiconductors and Semimetals, Volume 8*; Willardson, R. K., Beer, A. C., Eds.; Academic Press: New York, 1972, p 319-320.

(54)   Chamarro, M.; Gourdon, C.; Lavallard, P. *J. Lumin.* **1996**, *70*, 222.

(55)   Philipp, H. R. *Phys. Rev.* **1958**, *111*, 440.

(56)   Sridhara, S. G.; Eperjesi, T. J.; Devaty, R. P.; Choyke, W. J. *Mat. Sci. Engng. B* **1999**, *61-62*, 229.

(57)   Tiginyanu, I. M.; Sarua, A.; Irmer, G.; Monecke, J.; Hubbard, S. M.; Pavlidis, D.; Valiaev, V. *Phys. Rev. B* **2001**, *64*, 233317.

(58)   Feldman, D. W.; Parker, J. H.; Choyke, W. J.; Patrick, L. *Phys. Rev.* **1968**, *170*, 698.

(59)   Dorner, B.; Schober, H.; Wonhas, A.; Schmitt, M.; Strauch, D. *Eur. Phys. J. B* **1998**, *5*, 839.

(60)   Feldman, D. W.; Parker, J. H.; Choyke, W. J.; Patrick, L. *Phys. Rev.* **1968**, *173*, 787.

(61)   Hofmann, M.; Zywietz, A.; Karch, K.; Bechstedt, F. *Phys. Rev. B* **1994**, *50*, 13401.

(62)   Karch, K.; Pavone, P.; Windle, W.; Schutt, O.; Strauch, D. *Phys. Rev. B* **1994**, *50*, 17054.

(63)   Nakashima, S.; Katahama, H.; Nakakura, Y.; Mitsuishi, A. *Phys. Rev. B* **1986**, *33*, 5721.

(64)   Tomita, T.; Saito, S.; Baba, M.; Hundhausen, M.; Suemoto, T.; Nakashima, S. *Phys. Rev. B* **2000**, *62*, 12896.

(65)   Sarua, A.; Monecke, J.; Irmer, G.; Tiginyanu, I. M.; Gartner, G.; Hartnagel, H. L. *J. Phys.: Condens. Matter* **2001**, *13*, 6687.

(66)   Hayashi, S.; Kanamori, H. *Phys. Rev. B* **1982**, *26*, 7079.

(67)   Tiginyanu, I. M.; Irmer, G.; Monecke, J.; Hartnagel, H. L. *Phys. Rev. B* **1997**, *55*, 6739.

(68)   Spanier, J. E.; Herman, I. P. *Phys. Rev. B* **2000**, *61*, 10437.

(69)   Kuriyama, K.; Ushiyama, K.; Ohbora, K.; Miyamoto, Y.; Takeda, S. *Phys. Rev. B* **1998**, *58*, 1103.

CHAPTER 4

CHEMICAL AND TEMPERATURE SENSING

4.1 Introduction

One primary method of monitoring an engine's performance is by measuring the percentage of H_2 in the exhaust flow. Therefore, in recent years, NASA Glenn Research Center has led an effort to develop sensors that can detect H_2 concentrations at high temperatures. However, the demands upon the sensors are far greater than current capabilities. The sensor must be able to operate within a wide range of temperatures. It must have a low detection limit (< 100 ppm H_2), yet exhibit a wide dynamic range so that the sensor can also operate in environments approaching 100% H_2. The sensor must have both a quick response time as well as a rapid return to baseline signal upon removing H_2 from the gas flow. The sensor must be functional in both inert and oxygen-rich environments. Finally, the sensor must show specificity and be able to quantify the H_2 concentration amongst an environment of other (possibly caustic) gases.

The large specific surface area coupled with deep porosity and the need for efficient transport mechanisms to shuttle reactants and products between the solid-liquid interface and the locus of etching bode well for the use of PSiC in high sensitivity gas-sensing applications. The large surface area correlates directly with sensitivity, and the observation of a highly interconnected network of pores in the bulk argues for efficient molecular transport to the interior of the crystal. In this research, control of the etch depth was never established using electroless etching, so PSiC films of with predictable porous layer depths were never achieved via electroless etching. Therefore, for the sensing studies that follow, anodically etched PSiC samples were used in all experiments, because porous layers of desired thickness, as well as a more planar porous-nonporous interface, could be produced.

There are several methods of actually measuring changes in the environment (ambient gas identities, gas concentrations, temperature, pressure) with porous materials. Ellipsometry has been used to detect changes in the average refractive index of porous layers due to analyte adsorption.[1-4] A

reduction in photoluminescence intensity has also been utilized to detect molecular constituents.[5-10] In addition, interferometry has been used to detect different chemicals and biological compounds with PSi sensors.[11-18] Finally, many studies have been conducted measuring changes in conductivity to sense chemicals in porous silicon,[19-25] crystalline silicon carbide,[26,27] and porous silicon carbide.[28,29] Interferometry and conductivity measurements were chosen as the modes of detection in this research, since work with PSi reported in the literature has shown these detection methods to exhibit promising sensitivity, fast recovery to baseline, high dynamic ranges, small minimum detection limits, reversibility, fast time response, and limited selectivity.

Experiments were designed to take advantage of the inherent capabilities and advantages of SiC described in Chapter 1. Many applications exist for a sensor that can detect certain chemicals in a hostile (high temperature, caustic) environment. Applications that could benefit from improved sensing ability exist in the automotive industry, wafer processing, and in monitoring materials aging in nuclear reactors. The experiments detailed below were chosen to mimic conditions that may be encountered within a liquid fuel rocket engine, although simulating a rocket nozzle environment in a laboratory is obviously very difficult. Neither the extreme temperatures nor unstable exhaust species (such as atomic hydrogen, methyl radicals, etc.) within a rocket nozzle can be recreated easily.

In a rocket engine, both the concentrations of the exhaust gases as well as the temperature of the exhaust flow can be expected to fluctuate. Any one method of detection in itself will probably be insufficient to deconvolute the confounded effects of concentration and temperature changes. In addition, due to selectivity and cross-sensitivity, individual sensors are limited in the amount of information that they can provide in environments that contain multiple chemical species. Therefore, in this research, both interferometry and conductivity measurements were attempted with the goal of simultaneously detecting rocket exhaust species with molecular specificity as well as the chamber temperature. In the future, for any operational detection system, it is envisioned that a large array of different porous sensors would have to be constructed and probed in more than one way in order to simultaneously identify the various gas species present, their concentrations, and the temperature of the gas flow.

4.2 Interferometry

4.2.1 Background

Interferometry relies upon constructive and destructive interference of reflections from two surfaces. If a PSiC layer can be formed that has a small feature size compared to the detection optical wavelength, thin film interference will occur from light reflected at the air/PSiC and PSiC/SiC interfaces. The resulting spectrum will show Fabry-Perot interference fringes. The maxima in the fringes occur at wavelengths satisfying the relation:

$$m \cdot \lambda = 2 \cdot n \cdot l \,. \tag{4.1}$$

In Eq. 4.1, m is the spectral order (an integer), λ is the wavelength of the fringe maximum, n is the average refractive index of the film, and l is the thickness of the porous film. When a gas adsorbs to the walls of the porous film, the average refractive index of the PSiC layer changes, resulting in a shift of the Fabry-Perot fringes (*cf*. Fig. 1.1). The change in n can be attributed to two different effects. First, n is expected to increase due to a higher refractive index species displacing air from the nanopores. Simultaneously, the adsorption/absorption of the analyte may change the distribution of carriers within the semiconducting skeleton, thereby altering n for the porous layer. Utilizing Eq. 4.1, the shift in the fringe maximum can be used to quantify the amount of analyte in the gas stream flowing past the porous layer, as long as some of the gas adsorbs to the walls of the nanopores in the porous semiconductor.

The precise refractive index of any given PSiC layer is a function of the detailed structure and porosity and so varies from sample-to-sample, even for samples prepared under nominally identical conditions. Initially, an approximate value of the refractive index is needed, though, in order to form appropriate porous layer thicknesses for the interferometry studies. Petrova-Koch et. al. have reported n = 2.2±0.1 for their PSiC samples.[30] From ellipsometry measurements, Choyke has found that the best fit for n is simply linear between 0% and 100% porosity at 632.8 nm (n=2.63 to n=1).[31] These values were used to estimate an optimum initial PSiC layer thickness of approximately 3 μm for interferometry studies.

Because the exact thickness of an etched porous layer is not known immediately after etching (until the sample is cleaved and examined via SEM), the change in the porous films due to gas adsorption is usually quantified in terms of nl, the effective optical thickness (EOT). At the conclusion of the interferometry and conductivity studies, porous layers can be cleaved to measure the exact porous layer thickness via SEM. Once l is known, a value for the average refractive index of the film in nitrogen and the different adsorbate gases can be deduced.

In the literature, interferometry of PSi layers has been utilized to detect species such as hydrocarbons, alcohols, HF, CO, H_2O, O_2, and biological compounds. In this research, adsorbates were chosen that are anticipated to be found in the exhaust of liquid fuel rocket engines. Unfortunately, many of the gases in rocket engines have indices of refraction very close to air/nitrogen (Table 4.1). As a result, for these species, changes in n for the porous layer must be due solely to changes in the carrier concentration distribution in the semiconductor skeleton, since the refractive index of the pores will not change significantly when the adsorbate has nearly the same refractive index as air/nitrogen. Furthermore, a large dipole moment is required in order to perturb the charge distribution in the semiconducting skeleton and be detected.

Table 4.1 Index of Refraction for Several Gases of Interest

Species	Index of Refraction	Dipole Moment (D)
SiC	2.6 at 632.8 nm; 2.7 at 467 nm	
Air	1.0002926	
Nitrogen	1.000300	0
H_2	1.000132	0
CO	1.000340	0.112
CO_2	1.00045	0
Ethanol	1.36	1.69
Kerosene	1.442	~0
Acetone	1.357	2.88
Trimethylamine	1.400	0.612

4.2.2 Experimental

The PSiC samples were placed in a custom made flow cell that allowed for flow of nitrogen diluent and various adsorbate gases through the cell at controlled flow rates and concentrations. Individual mass flow controllers controlled the nitrogen and adsorbate gases. Adsorbate vapors were generated by bubbling a stream of nitrogen through analytes existing as liquids at 300 K, while pure CO was obtained from a compressed gas cylinder. The total flow rate was varied between 20-1000 sccm. Simultaneously the PSiC sample could be heated from 25 °C to 600 °C.

Reflection spectra were obtained using the experimental arrangement shown in Fig. 4.1. The beam from a tungsten lamp was collimated and then focused to a small spot (500 μm diameter) on the PSiC surface. The reflected light entered a spectrometer (Jobin Yvon CP200, entrance slit of 50 μm). The light was detected by a liquid nitrogen cooled CCD camera (Photometrics CH210).

It was soon discovered that only a small range of porous layer thicknesses would serve these experiments. If the porous layer became too thin, then the interferometric fringes were spaced too far apart, allowing only one or two fringes to be monitored within the 250 nm window of the monochromator. However, if the porous layers were made too thick, scattering losses limited the intensity of light reaching the porous–nonporous interface that was back-reflected out to the detector. So, for the thick porous layers, the collected reflections simply mimicked the source spectrum, and no fringes were observed. Optimum porous layers were found to have thicknesses of 3-4 μm. In addition, relatively low current densities during etching yielded the best success in producing Fabry-Perot fringes, possibly because the pore size was small enough to retain optical reflectivity of the PSiC surface.

CO is a common rocket fuel exhaust gas, and therefore it was examined first, even though success with CO was not anticipated due to its low refractive index and dipole moment. Other rocket fuel exhaust gases with similarly low refractive indices (such as hydrogen, oxygen, carbon dioxide, and small hydrocarbons) were not investigated. In addition to CO, two other common rocket fuels (kerosene and ethanol, a representative alcohol) were initially examined via interferometry. Finally, due to the lack of

success with these vapors (denoted below), acetone and trimethylamine were bubbled through the test cell, too.

4.2.3 Results and Discussion

Several samples of PSiC were produced via anodic etching that yielded well-resolved Fabry-Perot fringes in their reflection spectra. The reflection spectrum for the PSiC layer in pure nitrogen was compared to the spectra of the layer in different analytes, as shown for example in Fig. 4.2.

Unfortunately, none of the chemicals used in this work could ever be detected with PSiC layers via interferometry. PSiC layers with a native oxide layer, as well as samples that had been HF dipped or RCA cleaned (Table 4.2), were examined in these studies. CO (0-17%), ethanol (0-7%), acetone (0-17%), kerosene (0-0.25%), and trimethylamine (0-40%) were all investigated, but no shifts of the Fabry-Perot peaks were ever witnessed at room temperature or temperatures up to 500 ^{o}C.

<div align="center">Table 4.2 RCA Cleaning Protocol</div>

1. Dip in 1:1:5 (vol) NH_4OH : 30% H_2O_2 : H_2O at 70 ^{o}C for 5 min

2. Rinse in DI H_2O

3. Dip in 5 wt% HF for 5 min

4. Rinse in DI H_2O

5. Dip in 1:1:6 (vol) 37 wt% HCl : H_2O_2 : H_2O at 70 ^{o}C for 5 min

6. Rinse in DI H_2O

4.2.4 Conclusions

Interferometry does not appear to be a viable detection method for the analytes of interest with PSiC layers. Even for the relatively wide range of analyte properties examined in this work, no shifts of the Fabry-Perot fringes were ever witnessed.
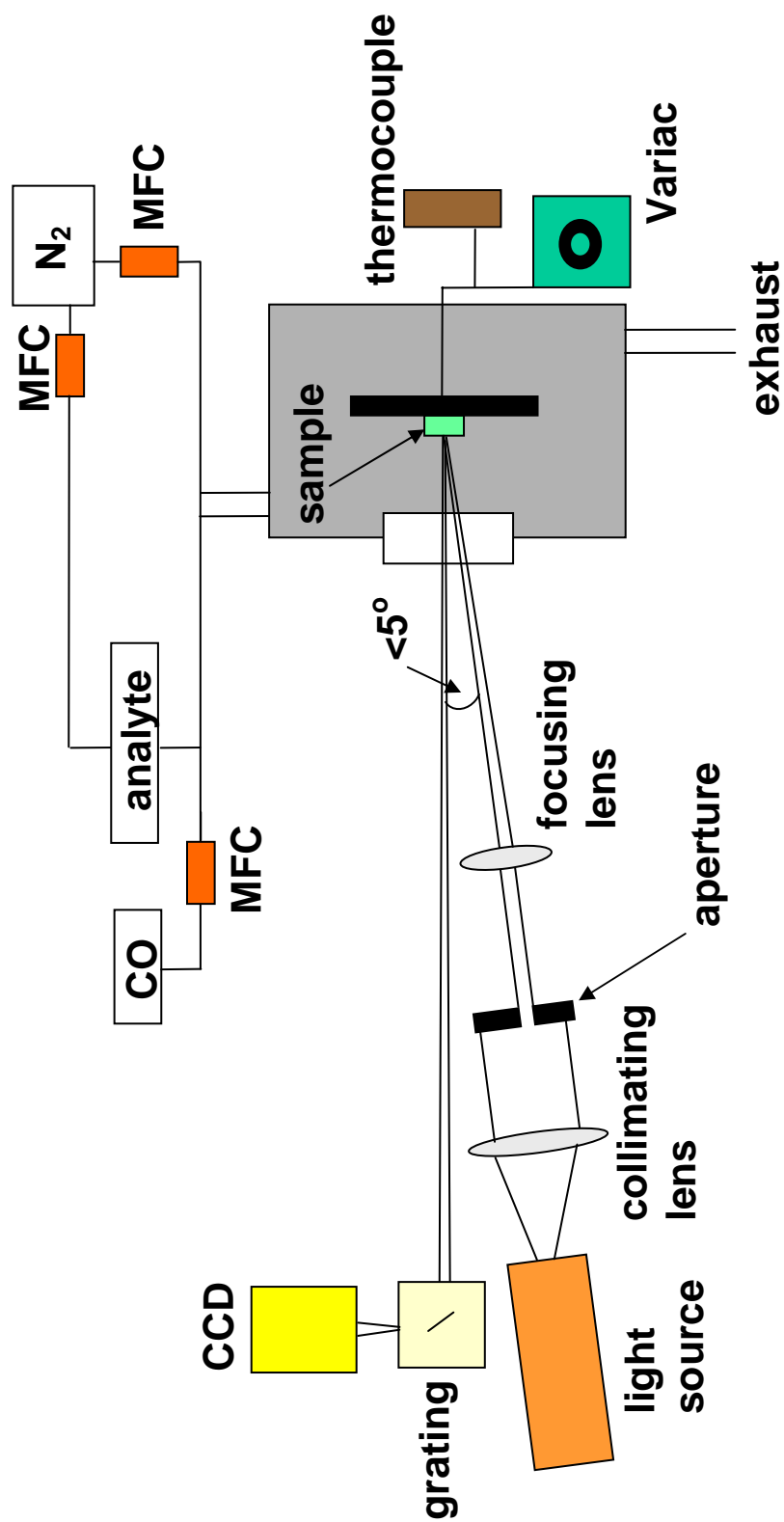
Figure 4.1. Experimental set-up for interferometry collection. The "analyte" was either ethanol, acetone, kerosene, or trimethylamine.
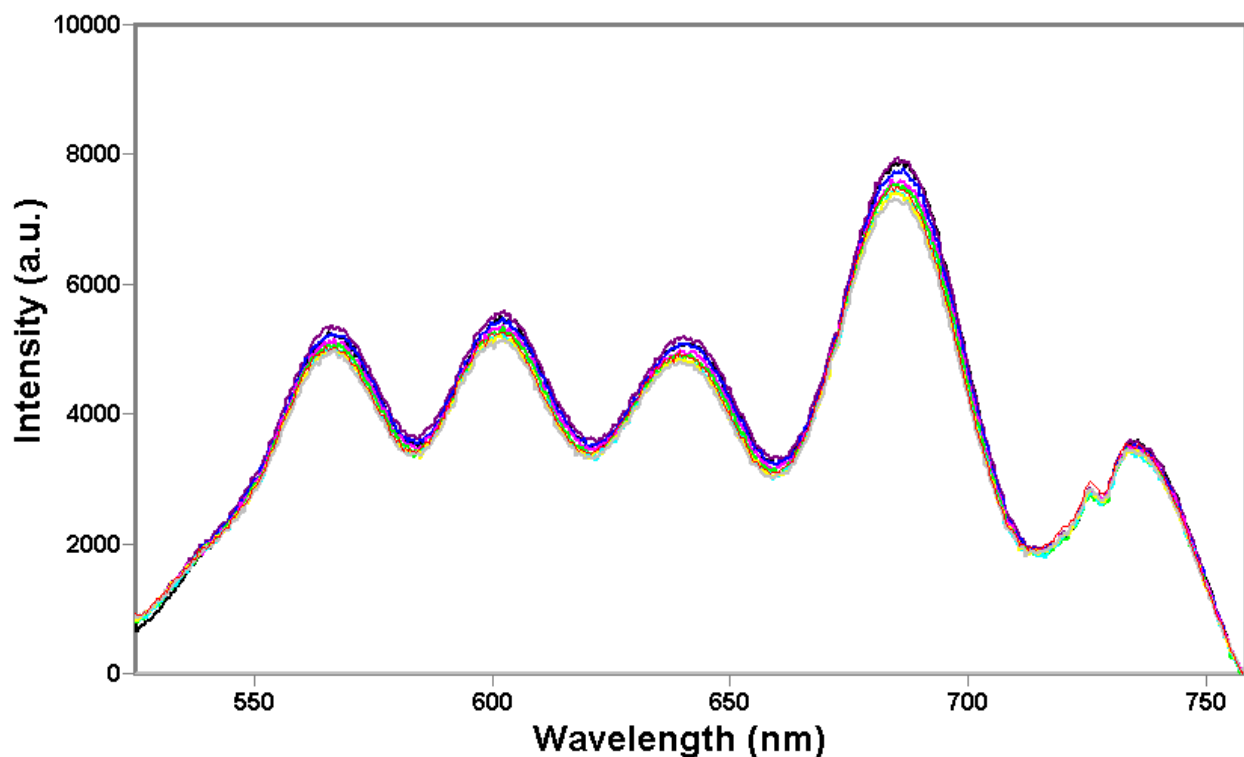
Figure 4.2. Fabry-Perot fringes from a PSiC layer exposed to 0-17% acetone. Notice the lack of any shifting of the Fabry-Perot fringes, as was observed for all of the analyte species investigated in this work.

4.3 Conductivity Measurements

4.3.1 Background

When a gaseous species absorbs or adsorbs to a porous semiconductor surface, the conductivity of the porous region often changes (usually an increase in conductivity is measured). There are several possible explanations for the increased conductivity, and the explanations depend upon the identity of the adsorbate involved. In some cases, adsorbates can redistribute charge in the nanocrystallites, reducing charge carrier depletion at the free surface. In addition, at high enough temperatures, the conductivity may increase due to absorption of the adsorbate into the crystal lattice, altering the lattice composition and, thus, the conductivity. Adsorbed species such as hydrogen[32] can also passivate dangling bonds (which can act as charge traps) on the SiC surface. Next, for certain vapors (at high enough concentrations), the adsorbate can condense into a liquid in the pores and carry current in addition to the current within the SiC matrix. If the adsorbate does not condense, it can at least lower barriers for carrier

hopping between nanocrystallites that are in close proximity. Finally, the relationship between conductivity and applied voltage is a function of the adsorbate concentration as well as its dipole moment, so these dependencies, which are molecularly specific, work together to determine the output signal.

There are several reports in the literature detailing hydrogen sensing via SiC devices. All of these devices exploit the H-induced change in barrier height at the metal-SiC interface which in turn shifts the I/V characteristic, thereby changing the measured conductivity. Published results denote a wide range of concentrations that can be sensed, reaching from the single digit ppm to tens of percent of hydrogen gas, although no single structure covers the entire composition range.[33-35] In general, these devices exhibit rapid response to the presence of hydrogen in the gas flow, usually responding on the order of a few seconds.

However, a variety of technological hurdles remain in order to develop a viable hydrogen sensor using SiC. Most of the devices in the literature work in a fairly tight range of temperatures. Lower limits on operating temperature are dictated by the need for hydrogen to dissociate on the activated metal, be absorbed, and diffuse through the metal gate. Upper temperature limits are often dictated by the formation of oxides or other deleterious effects to the activated metal gate material. Few devices are reported to work at room temperature;[35] some reports have shown response at 100 ^{o}C.[36] Upper limits of operability are typically in the 500-600 ^{o}C range. Obviously, a wide range of operating temperatures is desirable.

The crystallographic quality of the metal gate material (usually Pt or Pd) is also an important parameter governing the response of hydrogen sensing devices.[37-44] Both sensitivity and selectivity are highly dependent upon the morphology of the gate metal. Hydrogen and some hydrogen-containing compounds (small hydrocarbons) can usually be sensed regardless of the thickness and morphology of the gate metal. However, whether other species, such as CO, NO_2, and O_2, contribute to the sensing signal is very dependent upon the gate morphology and thickness. These chemicals require near-direct contact with the SiC surface in order to be detected, so the degree of coverage and "cracks" in the gate metal determine the sensitivity to these non-hydrogen containing compounds. Therefore, exactly which

chemicals are detected, as well as their individual sensitivities by the device, are all affected by the thickness and quality of the metal gate layer.[45,46] Furthermore, Pd gates may be restricted to relatively low temperatures ($< 400\ ^{o}C$) due to the formation of palladium oxides at higher temperatures.[34] In addition, prolonged heating at 425 ^{o}C of Pd/SiC Schottky diode structures have been shown to change the sensor properties and decrease sensor response, partially due to the formation of palladium silicides Pd_xSi (x=1, 2, 3, 4) at the interfacial region.[39,40] Finally, prolonged exposure to elevated temperatures can lead to the formation of PdO and SiO_x compounds on the top surface of the gate metal. Even a thin layer of these compounds appears to have significant impact on the catalytic properties of the surface, forming a surface passivation layer that reduces the sensitivity to gas adsorption.[39]

Just as the processing conditions of the gate metal can determine sensor properties, selectivity and sensitivity can similarly be dictated by how the gate oxide is processed in MISiC devices. Differences in the deposition of SnO_2 gate films have been shown to affect the sensor response, even if the geometry of the film is the same.[41] Particularly, tight control of the thickness and stoichiometry of the SnO_2 film are required. Furthermore, drift in the properties of SnO_2 films with long-term heating due to grain boundary annealing has been noted.[47] The performance of capacitors utilizing SiO_2 insulating layers have shown similar dependence on processing conditions, especially annealing.[43]

Many of the devices in the literature that can detect small (ppm) concentrations of hydrogen saturate at relatively low concentrations of hydrogen, too. Kim et. al.[36,48] report a SiC Schottky diode that can detect less than 160 ppm H_2, yet the device saturates at approximately 600 ppm H_2 (Fig. 4.3). Similar saturation levels have been found with alternative, thicker gate insulators.[44] An attractive possibility is that porous devices may exhibit a much larger range of detectable hydrogen concentrations.

The metal gates used in the Schottky diode devices behave quite differently depending on whether the gas mixture is oxygen-rich or oxygen-lean.[33,37,46,49] Therefore, these devices often yield different results for the same concentration of hydrogen, depending on whether the amount of oxygen in the total flow is greater or less than the amount of hydrogen being detected. Careful monitoring of the O_2 concentration appears to be a necessary component of using Schottky diode sensors to detect H_2.

The devices detailed in the literature have relatively slow, and sometimes incomplete, recovery to baseline signal conditions. For very limited ($< 0.1\%$) hydrogen exposure, Schottky diode devices have been shown to recover to baseline conditions within a few tens of seconds.[36] After further hydrogen exposure, hydrogen and oxygen must be balanced in order to prevent baseline drift. If the device was originally exposed to any oxygen, then the sensors can be "rezeroed" via periodic exposure to oxygen between hydrogen sensing applications (Fig. 4.4).[45,49] Alternatively, a device can be outgassed before use in a pure nitrogen environment in order to desorb all oxygen from the device, then baseline drift is avoided as long as the device is never exposed to oxygen. Initial outgassing of the device to remove oxygen can take hours, though.[45] Even after outgassing all oxygen from the device, signal drift can be observed as a result of incomplete hydrogen desorption from the device (Fig. 4.5).[50] In some cases (when the exposure to high temperature is long enough), the drift in the baseline is unrecoverable. Diodes made of Pd on SiC have shown background drift due in part to reactions between the Pd and the SiC;[40,42] some method of stabilizing the Pd/SiC interface must be found in order to avoid this type of baseline signal drift. Like the Schottky devices, MISiC devices have shown similar problems of baseline drift.[34] These problems currently prohibit NASA from utilizing these sensors in the numerous uses in which the sensor must be able to survive exposure to 100% hydrogen without damage or change in calibration.[51]

Finally, devices that detect hydrogen often have similar responses to other gases. Methane,[36] propane,[37,45,49] butane,[45] ethylene,[42,45] propylene,[42,49] CF_4,[35] NH_3,[46] CO,[45,46,49] and NO_2[45] have all been detected by solid state SiC devices. Obviously, in a mixture of gases, all of the individual contributions of these components would have to be isolated and measured separately. Therefore, the additive response of single devices does not bode well for applications in which a single gas of interest in a mixture needs to be monitored. Rather, fabrication of an array of uniquely responding sensors is the most likely solution.

In order to measure changes in conductivity within porous layers, ohmic contacts to the porous morphology need to be formed. Ohmic contacts are much easier to make when the SiC wafer is heavily n-doped. Because our initial wafers had relatively low doping levels (less than 3×10^{18} cm^{-3}), a new
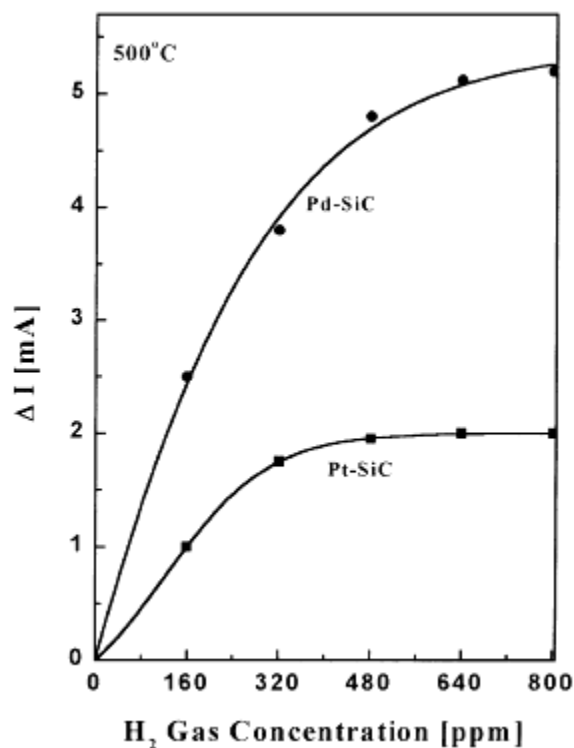
Figure 4.3.[36] Example of data from a PSiC Schottky diode showing low detection limits for H_2 coupled with relatively low saturation points.
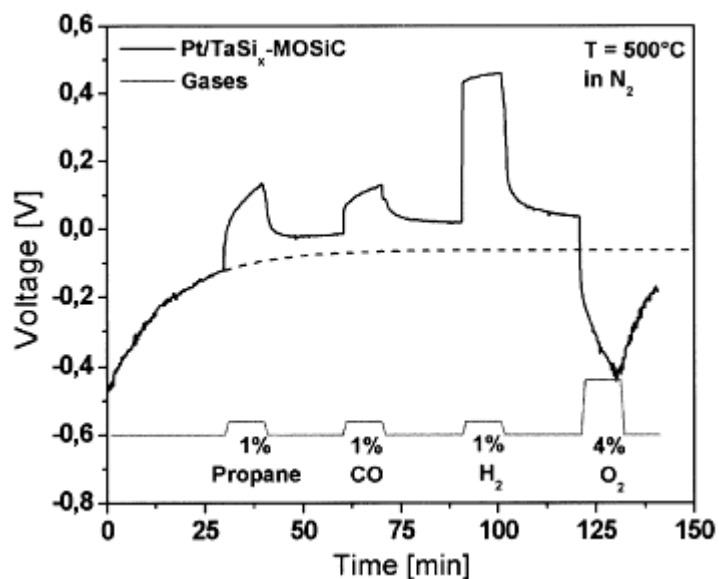
Figure 4.4.[46] Data showing drift in the baseline conditions for a Pt-TaSi-SiC Schottky diode sensor operating at 500 $^{\circ}$C. The sensor drift is believed to be due to slow desorption of surface oxygen ions from the sensor during the exposure to the N_2 background atmosphere.
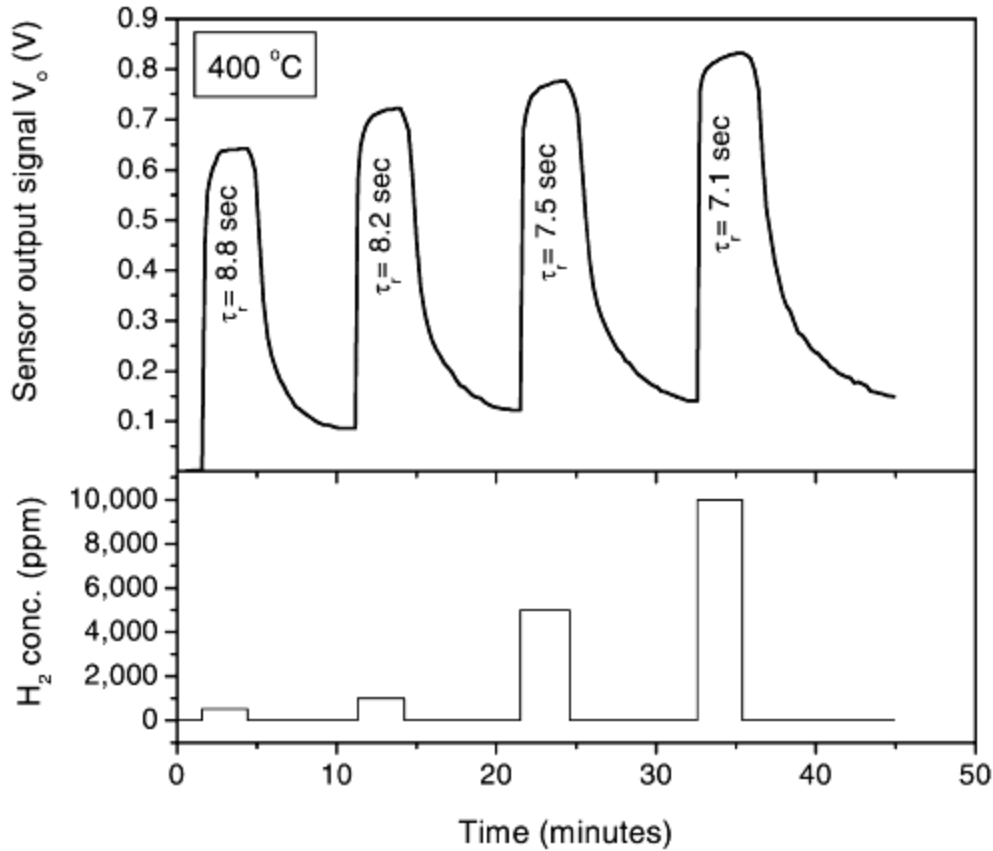
Figure 4.5.[51] Response of a Pd/SiC Schottky sensor to H_2 at 400 $^{\circ}$C. Notice the rising baseline condition with repeated H_2 exposure.

wafer was ordered with a higher n-doping level (8×10^{18} cm^{-3}). The conductivity tests detailed below were conducted with this highly n-doped 6H-SiC wafer.

The literature details numerous studies addressing which contact materials form the most stable, ohmic contacts to SiC.[52-65] However, the most simple and relatively reliable ohmic contacts are formed by depositing nickel on the SiC surface.[66-70] These contacts have shown excellent thermal stability up to 500 $^{\circ}$C.[52,66] For nickel to form an ohmic contact with the SiC, nickel silicide (Ni_2Si) must form. Therefore, an annealing step at temperatures of about 800-900 $^{\circ}$C or greater is necessary. However, because the silicon in the SiC is consumed in the formation of the silicide, excess carbon accumulates at the contact/SiC interface. This carbon then has a tendency to migrate to the free surface (and form

graphite nanocrystallites) and leave microvoids at the contact/SiC interface.[71-75] These microvoids do not

appear to be detrimental to contact performance at temperatures below 500 $^\circ$C for hundreds of hours.[66]

Another promising method of producing ohmic contacts to SiC is detailed in a series of papers by

Pecz et. al.[71-74] They deposit alternating layers of Ni and Si in the correct proportion to form Ni_2Si, and

therefore no silicon in the SiC wafer must be consumed to form the ohmic contact. Pecz and coworkers

have found one effective architecture to be Si(15 nm)/Ni(16.4 nm)/Si(30 nm)/Ni (32.8 nm)/Si(30

nm)/Ni(32.8 nm)/SiC. Upon annealing, small specific contact resistances (~1 x 10^{-5} Ω cm^2) along with

excellent adhesion and relatively low microvoid volumes were observed.

Of course, most of the work reporting ohmic contacts to SiC has utilized only crystalline SiC;

very little work has been performed to establish ohmic contacts to a porous layer. Shields et. al.[28,29] have

produced contacts with PSiC that display fairly ohmic behavior; Wu et. al.[76] have also made electrical

contact to n-doped and p-doped PSiC, although the quality of the contact was not evaluated during their

photodetecting studies. Slightly more work has been performed investigating ohmic contacts to PSi,[21,77-79]

but the nature of ohmic contacts to Si is much different than contacts to SiC, and the electrical properties

are quite different.

Specific contact resistance is a property used to characterize a contact as ohmic or Schottky.

"Ohmic" contacts are generally expected to have specific contact resistances of ~1 x 10^{-5} Ω cm^2 or less.

There are several methods of measuring the specific contact resistance. Kuphal's modified 4-point probe

technique uses structures which are easy to fabricate but is relatively inaccurate, as this method does not

account for current crowding at the contact edge.[80] The circular transfer length method (TLM) requires

tedious mathematical analysis that can be inaccurate. The method of Cox and Strack[81] is unique in that it

vertically measures the resistance, requiring four different sized circular contact pads on the top surface of

the wafer and a sheet of ohmic contact on the bottom surface of the wafer. The linear TLM was used in

this work, though, as this method allows for easy extraction of relatively small values of lateral contact

resistance. This geometry also limits the resistance measurements to the porous layers.

TLM involves measuring the total resistance between multiple contacts with unequal spacing between the contacts. Analysis of the data yields the sheet resistance, the contact resistance, and the specific contact resistance. In this work, TLM was first used to ensure that ohmic contacts could be deposited on our crystalline SiC wafers. These results were then compared to contacts deposited on porous layers to assess changes in the contact properties and the suitability of porous contacts for sensing studies.

An excellent review of TLM data interpretation is presented by Schroder.[82] In general the total resistance (R_T) is measured for various contact spacings, d, between the different contact pads. R_T is then plotted as a function of d. Analysis of the data reveals three pieces of data. First, the slope of the plot yields the sheet resistance (ρ_s), as

$$\rho_s = \frac{\Delta(R_T) \cdot Z}{\Delta(d)} \tag{4.2}$$

where Z is the contact width. Next, the contact resistance R_c can be calculated from the y-intercept, as

$$R_c = \frac{R_T}{2}. \tag{4.3}$$

Finally, the specific contact resistance ρ_c can be calculated from the x-intercept using

$$L_T = \sqrt{\frac{\rho_c}{\rho_s}} \tag{4.4}$$

in which L_T is the transfer length,

$$d = 2L_T. \tag{4.5}$$

As in the crystalline SiC hydrogen sensors discussed above, several options exist for the exact architecture of PSiC sensors. However, two basic unique sensing configurations can be used (Fig. 4.6). First, a capacitor type configuration can be constructed in which current flows vertically through the top porous (insulating) layer and then the crystalline substrate underneath. A grid contact can be formed on top of the PSiC layer, and a solid contact on the substrate's bottom. The grid contact pattern is beneficial because it produces a relatively large and even contact over the entire surface area, while allowing for

enough free surface area for analyte adsorption. Sensing is then accomplished by measuring the magnitude of current flow as a function of the applied bias.

Conversely, a horizontal (FET) configuration can be used. In this configuration, the porous layer becomes the "gate." The current through the device is measured as a function of applied potential between the "source" and "drain" contacts. However, the effectiveness of this architecture for a bulk SiC wafer is suspect, given the crystalline SiC substrate could short-circuit the device and provide a path for the current to bypass the porous region.

This research first investigated the formation of ohmic contacts to crystalline and then porous SiC. After reliable contacts could be made to PSiC with predictable specific resistances, tests were conducted to characterize the suitability of porous layers to measure different chemical environments via conductivity.
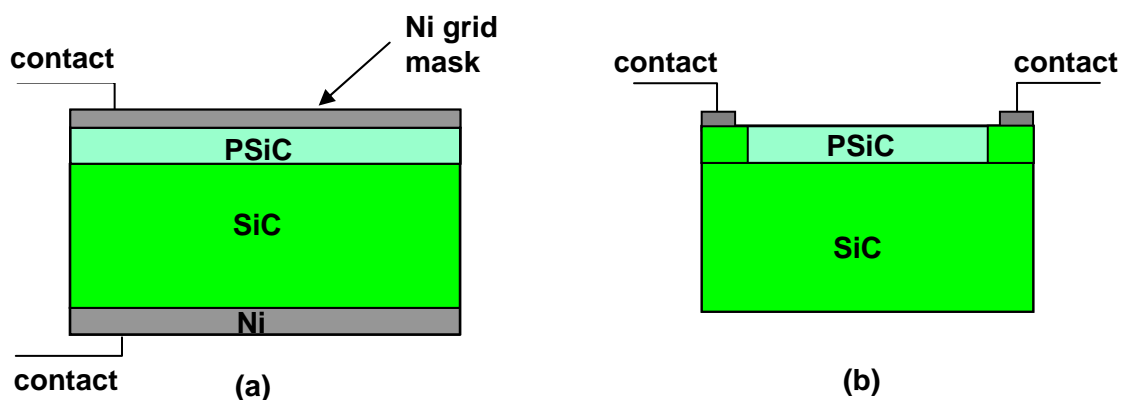
Figure 4.6. Two basic conductivity sensing configurations to measure the presence of adsorbate gases within a porous layer: (a) a capacitive device, and (b) a FET configuration.

4.3.2 Experimental

4.3.2.1 Specific Contact Resistance Measurements

Initially, TLM investigations were conducted to ensure ohmic contact could be made to both the crystalline as well as the porous SiC layers. Therefore, wafer samples suitable for TLM specific contact resistance measurements were fabricated. Many variations of sample preparation were studied (as discussed in section 4.3.3), but the general procedure is as follows. Before processing, the SiC sample

was dipped in HF and rinsed in water in order to remove any native oxide. The wafer was then ICP-RIE

etched in SF_6 (25 ^{o}C, 1.5 mtorr total pressure, 8.0 sccm SF_6, 2.0 sccm O_2, -200 V DC with a 4" diameter

plate, 800 W coil power, 3 min etch time) to remove the top 500 nm of the wafer and provide a clean SiC

surface. The sample was coated with 5214E photoresist (applied at 5000 rpm for 30 sec, resulting in ~1.5

μm thick photoresist) and subsequently baked at 110 ^{o}C for 35 sec. The wafer was then patterned via UV

lithography to form patterns of mesas 100 μm wide by 650 μm long. After UV exposure (approximately

400 watts for 20 sec), the wafer was developed (AZ327MIF or AZ300MIF for 1 min), rinsed in water,

and blown dry. The wafer was next ICP-RIE etched again to form mesas in the SiC approximately 1 μm

tall. These mesas were needed to isolate the TLM pads for conductivity measurements. Results in the

literature[83] have utilized mesas about 2.5 μm tall for TLM measurements of bulk 6H-SiC. Electrical

isolation of our mesas was ensured by measuring large resistances (off scale, in excess of 1 GΩ) between

pads on neighboring mesas.

After formation of the mesas, the remaining photoresist on top of the mesas was removed with

acetone followed by cleaning in isopropyl alcohol and water and finally blown dry. Next, the pattern for

the TLM pads had to be applied. The wafer was coated again with photoresist as described above. The

TLM pad pattern was applied via UV lithography as described above, except that now the exposure time

was only 8 sec, as an inverse pattern of the mask had to be formed. In this work, eight identically sized

pads (100 μm wide by 75 μm long) were deposited in a row, the pads separated by 2, 3, 4, 5, 6, 8, and 10

μm respectively. The photoresist was cured at 125 ^{o}C for 1 min. Next, the entire wafer was exposed to

ultraviolet irradiation (total dose of 375 mJ/cm^2 at 365 nm, or 6.8 mW/cm^2, 125 sec exposure time). The

photoresist was developed (AZ327MIF or AZ300MIF for ~3 min) and rinsed in water. Oxygen plasma

treatment (O_2 at 0.8 W/in^2 for 30 sec, 500 mtorr total pressure) ensued in order to clean any residual resist

from the wafer surface.

Several different metallization schemes were investigated. Nickel, titanium, and nichrome (80%

nickel and 20% chromium by weight) contact material were deposited via electron beam evaporation at

pressures below 8 x 10^{-7} torr. Ni, Ti, and NiCr were applied at deposition rates of approximately 0.2 nm/sec. Alternatively, contacts made of alternating Ni/Si layers or Ni/Al layers were deposited via argon sputtering at pressures below 3 x 10^{-6} torr. Gold was thermally evaporated onto the contacts at pressures below 8 x 10^{-7} torr at a rate of approximately 0.2 nm/sec. After metal deposition, lift off of excess metal occurred in an acetone dip for 1 min.

The annealing time and temperature has proven to be a critical parameter in the Schottky-to-ohmic contact transition,[80] and therefore various annealing conditions were investigated in the TLM portion of this work. Annealing temperatures between 800-1100 $^{\circ}$C and times from 0-20 min were performed in pure dry nitrogen.

4.3.2.2 Fabrication and Testing of Devices

All of the sensors fabricated for this test series were anodically etched in a similar manner. The wafers were etched for 60 min with a current of 4.5 mA. This consistently yielded a PSiC film approximately 4 μm thick in each sensor (as verified by SEM measurements at the conclusion of sensing studies).

During lift off of the excess metal, a short duration sonication was often needed in order to aid in the removal of the excess metal. This sonication did not damage the contacts made to crystalline SiC. However, it was found that sonication would often fracture the porous SiC film. Therefore, sonication was not used with porous wafers, and the success rate of forming isolated TLM pads on porous SiC was low (~2%). As a result, when making actual devices, a new (thicker) photoresist was tested and used.

The SiC sensor sample measuring 5 x 5 mm was first dipped in acetone, methanol, HF, and then water to initially clean the wafer. The sample was coated with AZ4330 photoresist (applied at 4000 rpm for 30 sec, resulting in ~5 μm thick photoresist) and subsequently baked at 100 $^{\circ}$C for 1 min. The sample was then patterned with a mask 4.8 x 4.8 mm in size, containing 24 squares 800 μm on a side (Fig. 4.7). The mask was illuminated at a total dose of 400 mJ/cm^2 at 365 nm. Next, the pattern was developed for approximately 90 sec using AZ400K developer diluted 1:4 in DI water. Oxygen plasma treatment

ensued, followed by metal deposition. Finally, liftoff in acetone was used (without any sonication) to remove the excess metal.

When making devices, bonding wire to the contacts was necessary. Originally, a Hybrid Model 572 Thermosonic Gold Wire Bonder with 0.001" diameter gold wire was used. However, bonding wire applied with this bonder often would not adhere well to the device, and often large craters formed in the contacts (Fig. 4.8). Therefore, 0.01" diameter gold wire was bonded to the sensing devices with silver conductive epoxy.

The devices were placed into a steel flow cell for conductivity tests. The porous device and a K-type thermocouple were suspended 1 mm from a strip of nichrome that was resistively heated to the desired temperature. Temperature was manipulated during the sensing studies in one of two ways. First,
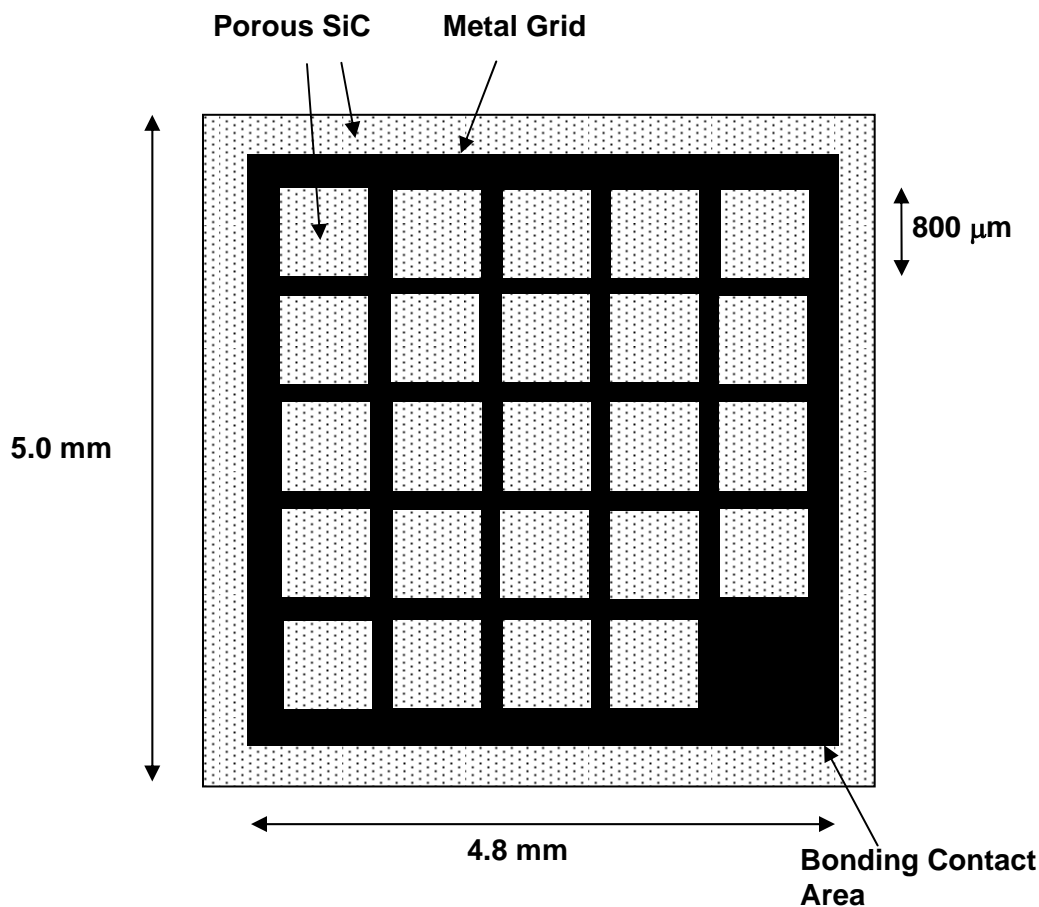

Figure 4.7. Masking pattern used for sensor fabrication. The black areas represent the metal contact (200 μm wide around the periphery and 100 μm wide in the interior).
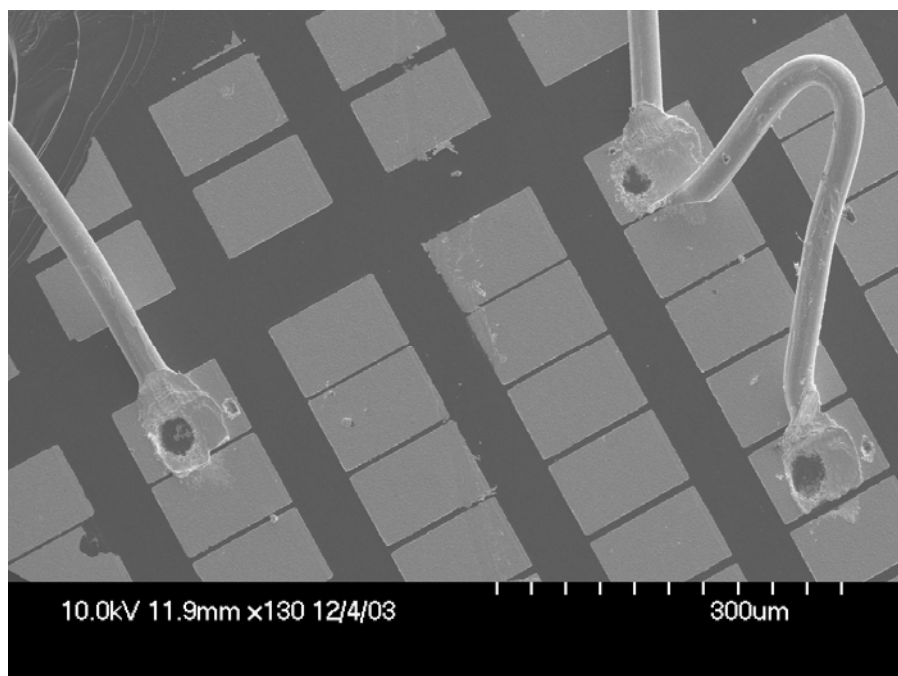
Figure 4.8. SEM images of three bonding sites performed with the Hybrid Model 572 Thermosonic Gold Wire Bonder. Notice the craters formed in the gold TLM pads. Because these craters could not easily be eliminated, and the 0.001" diameter bonding gold wire was not robust to manual handing, manual bonding with conductive epoxy and 0.01" diameter gold wire was chosen to make the sensing devices.

in constant temperature tests, the analyte gas was adjusted, and then the temperature of the nichrome heating strip was adjusted to keep the temperature of the porous device and thermocouple constant. Alternatively, in constant applied heat tests, once an original temperature was attained, further manipulations of the analyte gas flow were conducted with no change in the resistance through the nichrome heating strip, allowing the temperature of the porous device and thermocouple to rise during the test as the analyte concentration increased. In this mode of operation the suspended sensor experienced both conductive and convective heating from the gas flow.

Several variations of data collection were attempted. The data presented below were collected by sweeping the applied voltage across a set range and measuring the current at each voltage step. Then, the slope of the I/V plot was used to determine the resistance of the porous sensor for each gas flow and temperature condition. Several different voltage ranges were tested, including -2500 to 2500 mV (50 mV steps, 40 sec collection time), -500 to 500 mV (25 mV steps, 8 sec collection time), and -5 to 5 mV (1 mV

steps, 4 sec collection time). Results between these different voltage ranges were indistinguishable; therefore, for most of the data below, sweeps from -5 to 5 mV were used since this consumed the least amount of power (as would be desirable in a functioning sensor). Of course, data collection time could be reduced if one single voltage could be applied and the measurement made from that single resistance. However, it was found that single voltage measurements were considerably more noisy and inconclusive than the -5 to 5 mV voltage sweep. In addition, AC measurements of the resistance were made with an AC lock-in amplifier. In general, the data trends and magnitudes were identical to those found via the DC experiments. However, since once again the AC measurements were single point measurements, the data was considerably noisier. As a result, we can conclude that a majority of the scatter in the data for a single sensor is due to thermal noise, and *1/f* noise is probably negligible in these DC voltage sweeps.

Initial studies were performed to quantify the combinatorial effects on conductivity by an adsorbate gas simultaneous with temperature changes. Adsorbates tested in the conductometric experiments include N_2, H_2, ethanol, and acetone. The H_2, ethanol, and acetone were each diluted in N_2 to the desired concentration. The total flow rate was 100 sccm. The wafer temperature was varied between 25-500 ^{o}C.

4.3.3 Results and Discussion

4.3.3.1 Contact Formation

4.3.3.1.1 Crystalline SiC

Initially, pure Ni contacts (150 nm thick) were studied via TLM. As expected, the unannealed contacts were Schottky (Fig. 4.9). After annealing at 800-1100 ^{o}C for 30 sec-10 min, none of the nickel contacts adhered well to the crystalline SiC surface, as the TLM sampling probes easily caused the nickel to crumble and delaminate from the surface. Therefore, no current would flow between neighboring annealed contact pads.

Next, 150 nm thick Ni pads were capped with 50 nm of gold before annealing. The gold cap layer was applied to prevent any oxidation of the nickel contact. During TLM measurements, the gold

cap layer eliminated the crumbling of the contact, but delamination of the annealed contacts remained an issue.

Adhesion problems have been successfully alleviated in the literature by depositing a thin Ti layer first to the substrate. An added benefit of applying Ti to Ni contacts on SiC is that the Ti consumes some of the excess carbon to form TiC while maintaining good ohmic contact behavior.[70,83,84] Therefore, the next set of contacts were made of 50 Å Ti, 1500 Å Ni, and then a gold cap layer 500 Å thick. These contacts were structurally sound and did not delaminate from the SiC wafer. The unannealed contacts showed good adhesion to the underlying crystalline SiC substrate, although some discontinuities existed in the Ni layer (Fig. 4.10). Annealing at 900 $^{\circ}$C for 1 min or more resulted in improved contact homogeneity (Fig. 4.11). The unannealed contacts were Schottky, with results very similar to the pure nickel contact results shown in Fig. 4.9. After testing various annealing conditions (800-1100 $^{\circ}$C for 0-20 min), optimum conductivity was found to occur after annealing at 900 $^{\circ}$C for 10 min. Annealing times in excess of 10 min result in no reduction of the contact's resistance. An example of contact behavior as a function of annealing time is shown in Fig. 4.12. 10 min annealing times at 900 $^{\circ}$C resulted in ohmic contacts forming ~15% of the time. Figs. 4.13 and 4.14 present data collected from TLM pads for these contacts. This data yields a specific contact resistance of 1.3 x 10^{-5} Ω cm^2 for the crystalline SiC contacts.

Because the Ti/Ni/Au contacts were ohmic only ~15% of the time, several other metallization schemes were investigated as described below. However, none of the contacts described below exhibited a greater rate of success than the Ti/Ni/Au contacts, and eventually all devices were made with Ti/Ni/Au or Ti/NiCr(20% Cr)/Au contacts.

Following the work of Pecz et. al.[71-74] described in section 4.3.1, alternating Ni and Si layers were deposited via argon sputtering in the stoichiometric ratio to form Ni$_2$Si. Annealing at 1000 $^{\circ}$C for 3-10 min yielded contacts that were ohmic ~100% of the time, so these contacts were very promising. However, SEM analysis of the contact morphology indicated these contacts would be problematic to cap with gold. Gold capping is necessary to protect the contact from oxidation as well as allow for bonding. Argon sputter deposition resulted in poor adhesion of the unannealed contact materials to a rough surface,
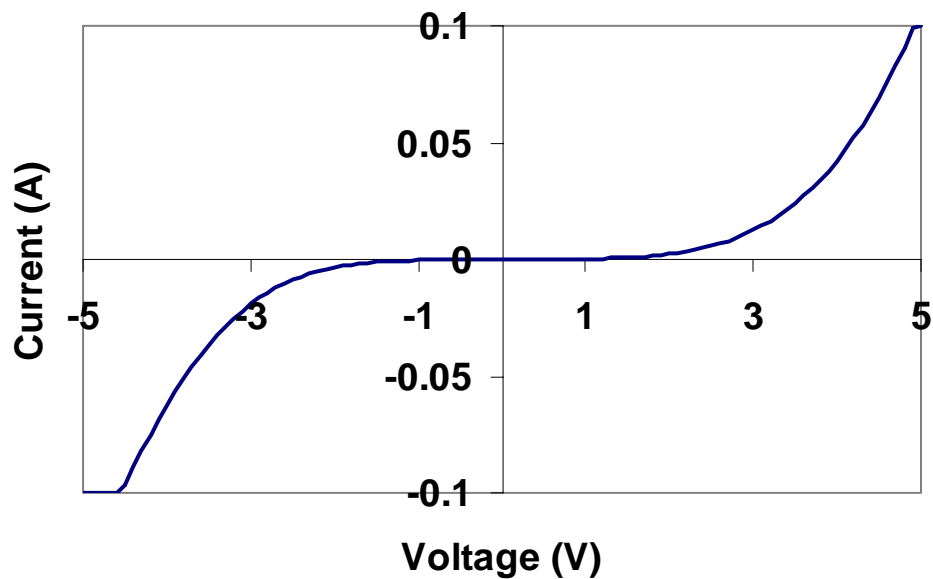
Figure 4.9. I/V curve of an unannealed 150 nm thick nickel contact to crystalline SiC, showing the expected Schottky character.
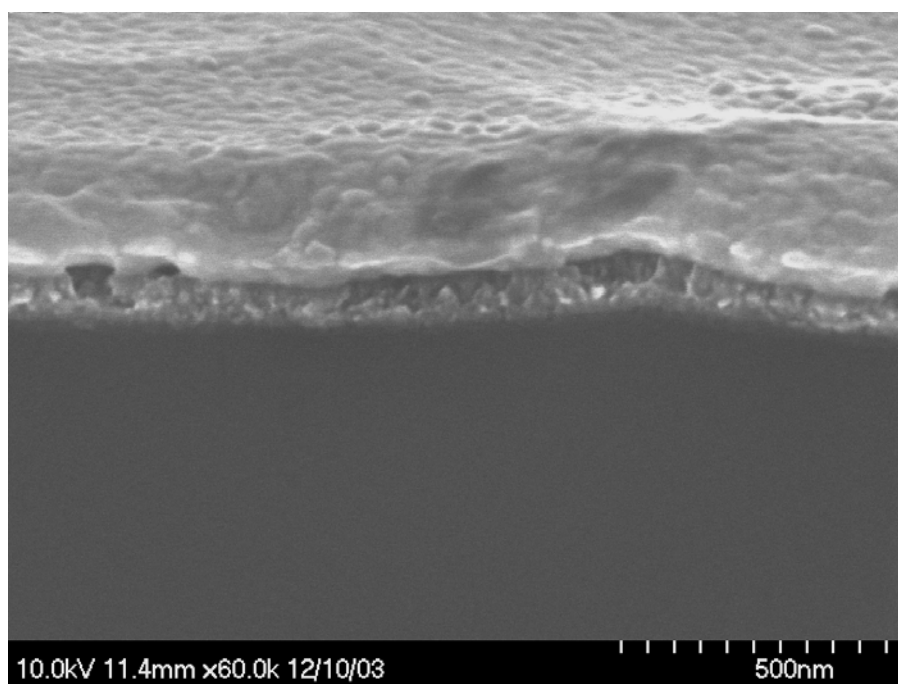

Figure 4.10. Cross-sectional SEM image of an unannealed contact composed of 50 Å Ti, 1500 Å Ni, and 500 Å Au. The substrate is crystalline SiC.
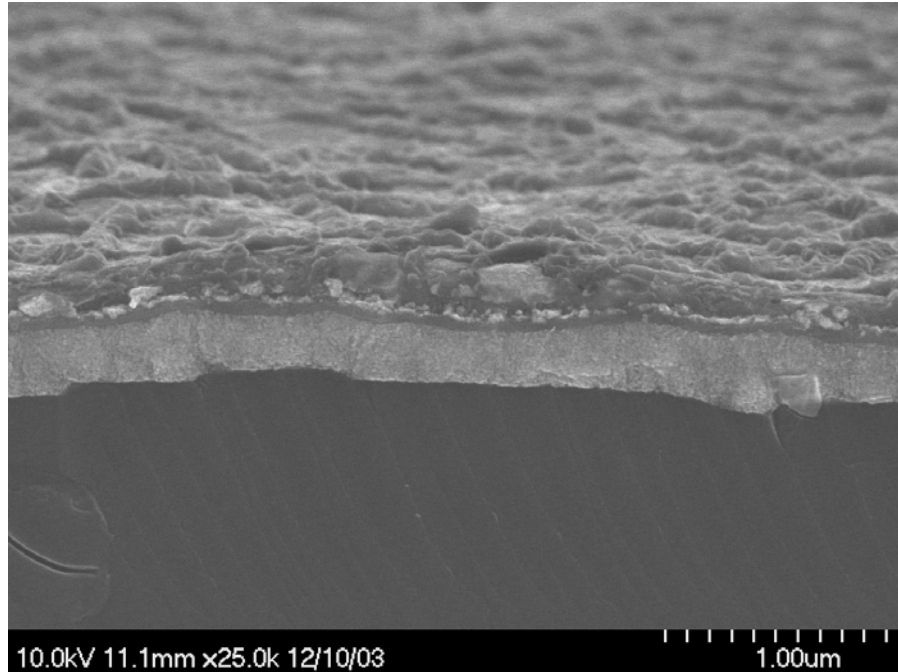
Figure 4.11. Cross-sectional SEM image of a contact composed of 50 Å Ti, 1500 Å Ni, and 500 Å Au, annealed at 900 ^{o}C for 1 min. The substrate is crystalline SiC.

as shown in Fig. 4.15. Annealing at 900-1000 ^{o}C resulted in improved adhesion to the SiC substrate; however, the contact material formed large voids during annealing. In Fig. 4.16, after just 20 sec of annealing, voids can be seen to form in the Ni and Si layers reacting to form Ni_2Si. In other samples, large sheet-like voids were formed during annealing (Fig. 4.17). Even longer annealing times resulted in contacts composed of many nanowires and large pockets (Fig. 4.18 and Fig. 4.19). When gold cap layers were thermally evaporated onto the Ni/Si layers prior to annealing at 1000 ^{o}C, the gold caps failed with only short annealing times. Within a few minutes of annealing, the gold cap layers would become discontinuous (Fig. 4.20). When the contacts were annealed for 10 min or more, the change in contact morphology caused nearly all of the gold cap layers to form small pools or completely delaminate from the contact. Alternatively, a protocol was investigated in which the Ni/Si layers were annealed to make ohmic contacts and then the gold cap layer was deposited. However, no better success rate was achieved. A significant (25% or more) portion of the gold cap layers would delaminate from the contacts during lift
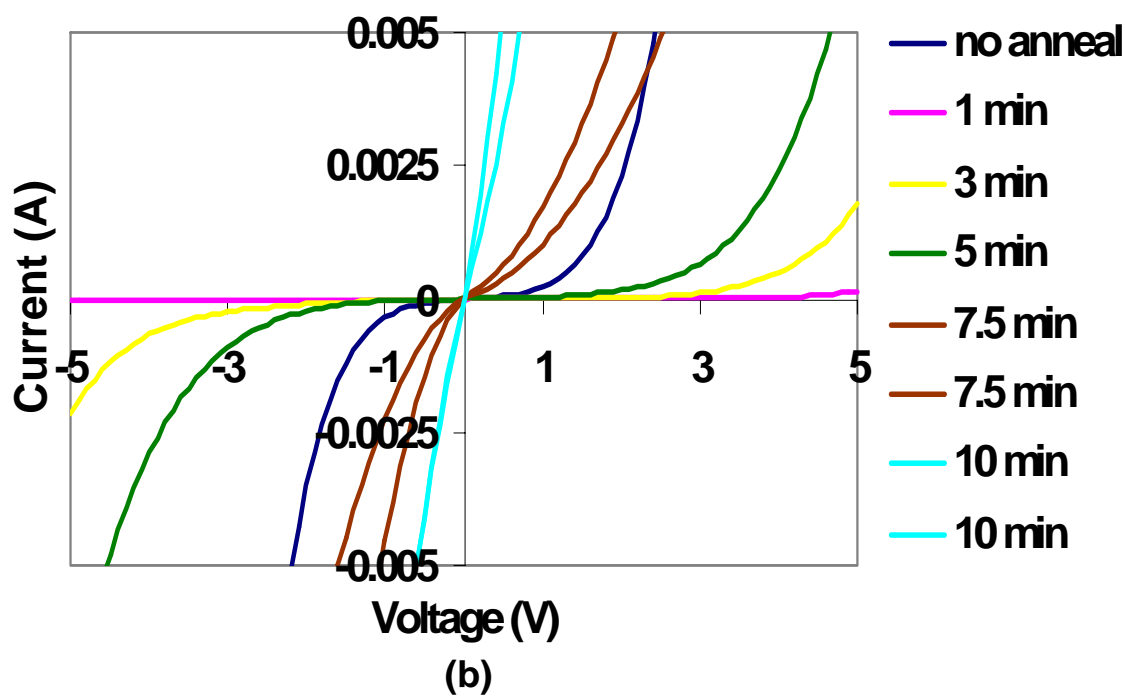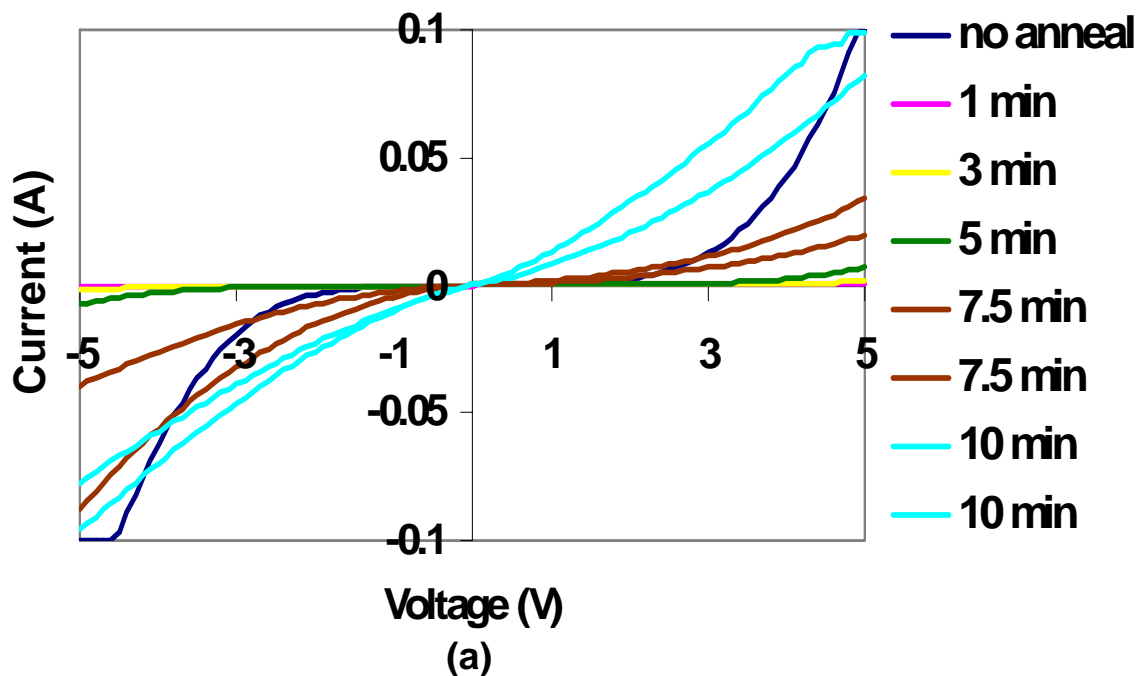
Figure 4.12. I/V curves for contacts composed of 50 Å Ti, 1500 Å Ni, and 500 Å Au annealed at 900 °C for the times indicated. The substrate is crystalline SiC. (a) is shown in full scale, while (b) has the current scale enlarged to show detail. Anneal times in excess of 10 min result in no reduction of the contact resistance.
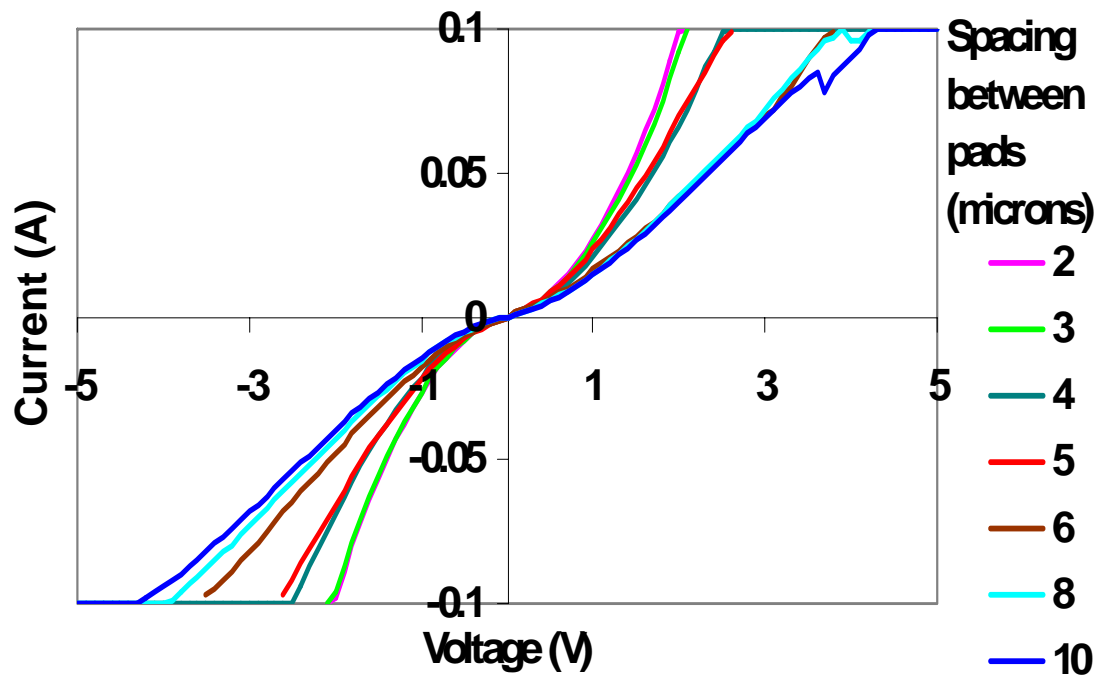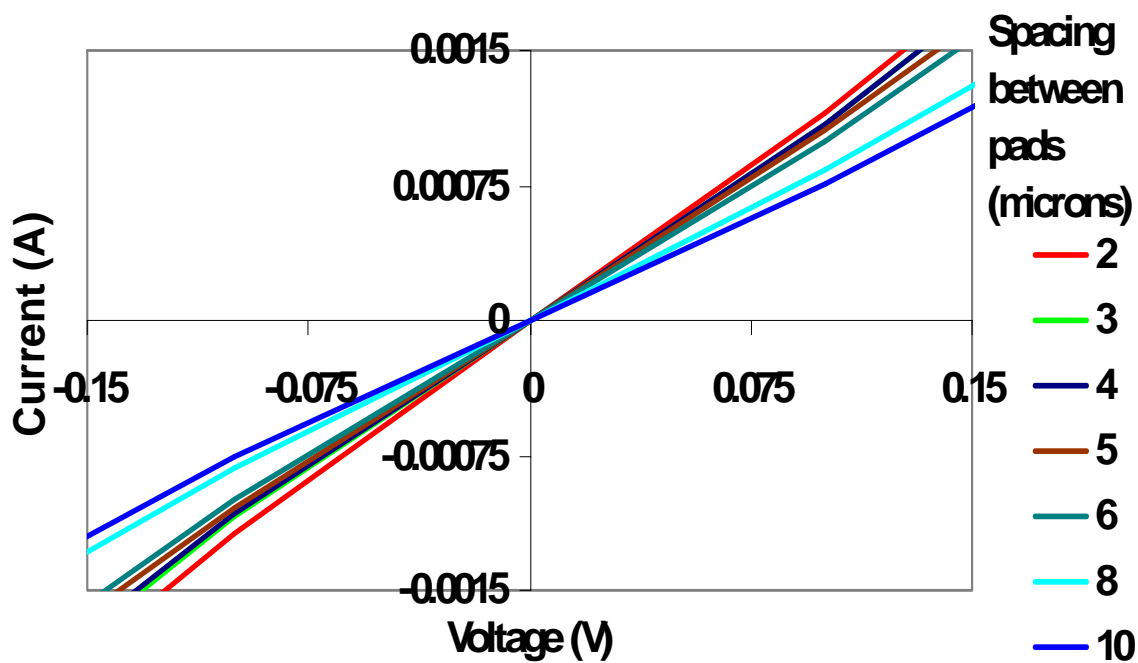
Figure 4.13. I/V data collected from a row of contact pads composed of 50 Å Ti, 1500 Å Ni, and 500 Å Au annealed at 900 ^{o}C for 10 min. The substrate is crystalline SiC. (a) is shown in full scale, while (b) has the current scale enlarged to show detail.
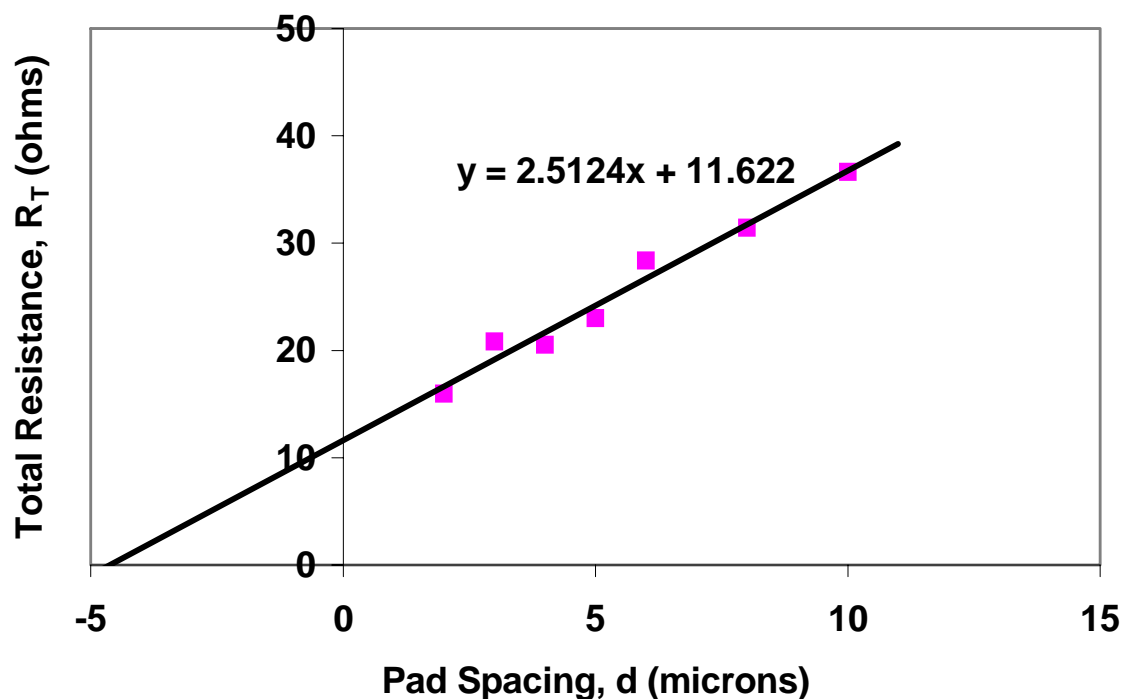
Figure 4.14. TLM data collected from a row of contact pads composed of 50 Å Ti, 1500 Å Ni, and 500 Å Au annealed at 900 $^{\circ}$C for 10 min. The substrate is crystalline SiC. Analysis of the data according to Eqs. 4.2-4.5 yields a specific contact resistance of 1.3 x 10^{-5} Ω cm^2 for these contacts.
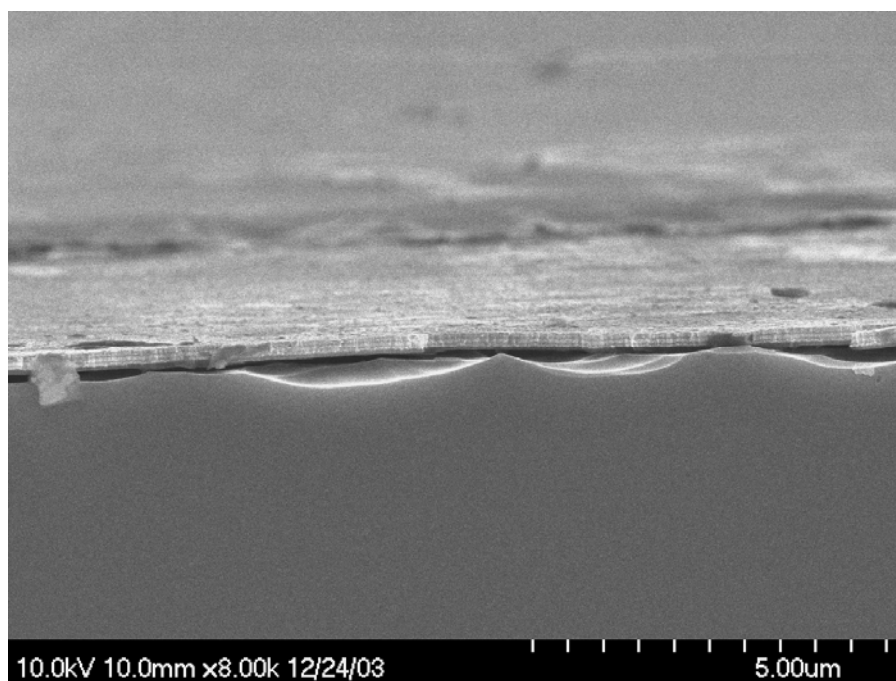
Figure 4.15. Cross-sectional SEM image of alternating Ni and Si layers argon sputtered onto a rough SiC crystalline surface. Notice the poor adhesion to the crystalline SiC substrate.
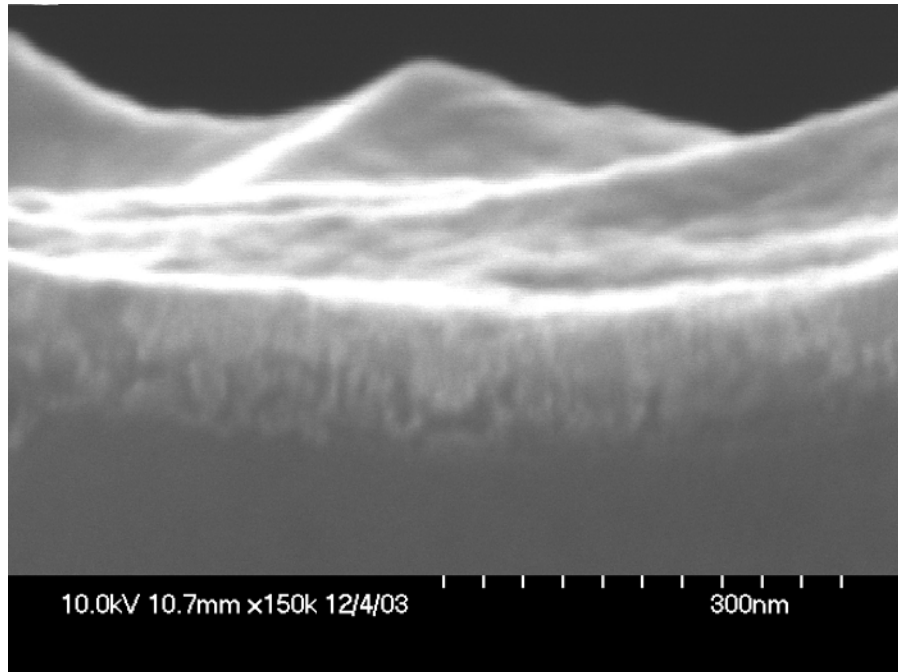
Figure 4.16. Cross-sectional SEM image of a contact composed of argon sputtered Si(15 nm)/Ni(16.4 nm)/Si(30 nm)/Ni(32.8 nm)/Si(30 nm)/Ni(32.8 nm)/SiC that has been capped with 25 nm Au and then annealed for 20 sec at 900 $^{\circ}$C. Notice the voids forming during the annealing reaction. The substrate is crystalline SiC.
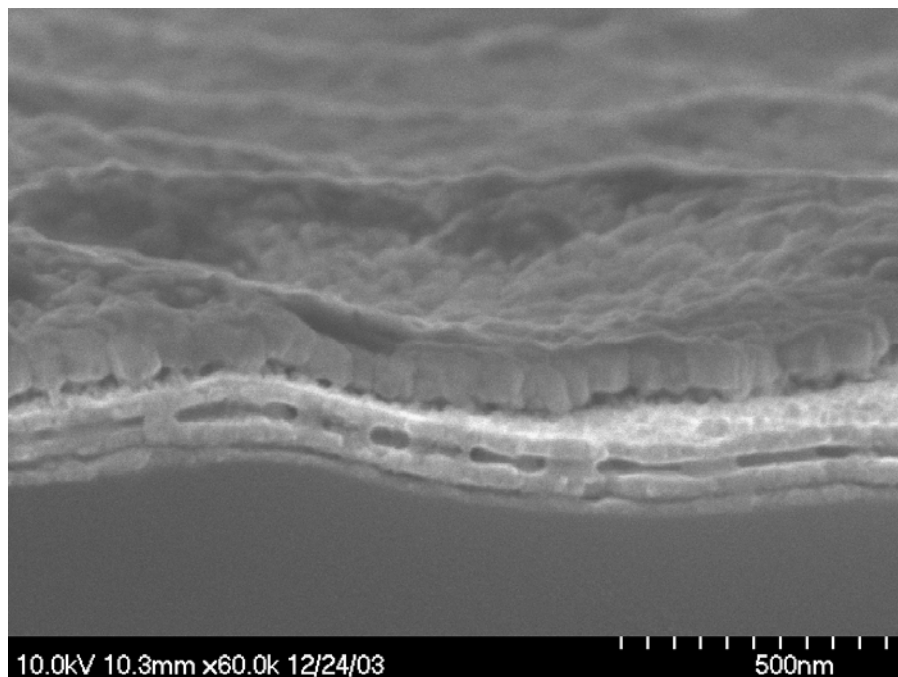
Figure 4.17. Cross-sectional SEM image of a contact composed of argon sputtered Si(15 nm)/Ni(16.4 nm)/Si(30 nm)/Ni(32.8 nm)/Si(30 nm)/Ni(32.8 nm)/SiC that has been annealed for 3 min at 1000 $^{\circ}$C and subsequently capped with 250 nm Au. Reaction between the alternating Ni and Si layers resulted in large voids and poor contact adhesion. The substrate is crystalline SiC.
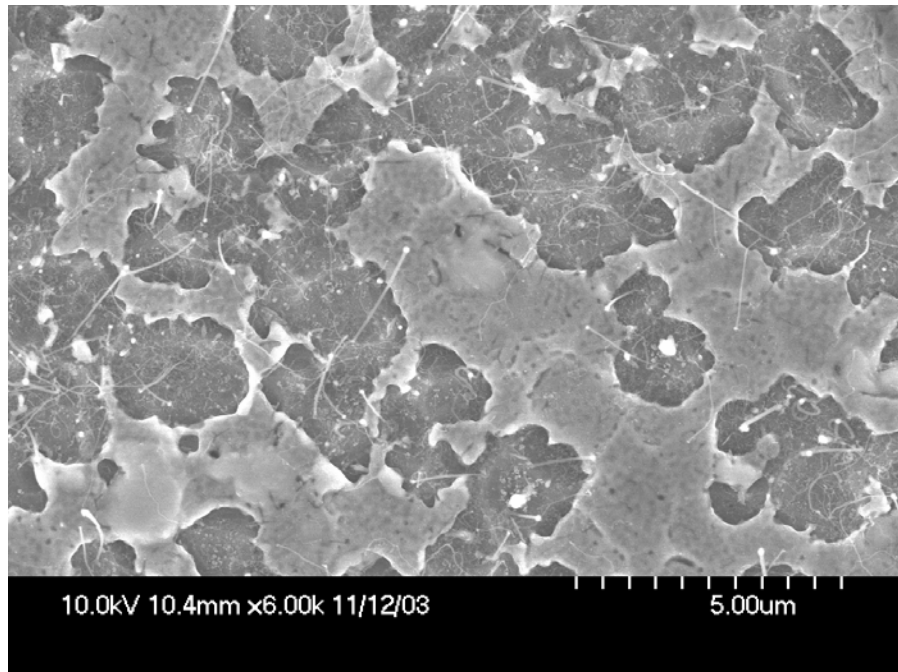
Figure 4.18. Plan view SEM image of a contact composed of argon sputtered Si(15 nm)/Ni(16.4 nm)/Si(30 nm)/Ni(32.8 nm)/Si(30 nm)/Ni(32.8 nm)/SiC that has been annealed for 10 min at 1000 $^{\circ}$C. Reaction between the alternating Ni and Si layers resulted in cratering of the top surface as well as the formation of nanowires. The substrate is crystalline SiC.
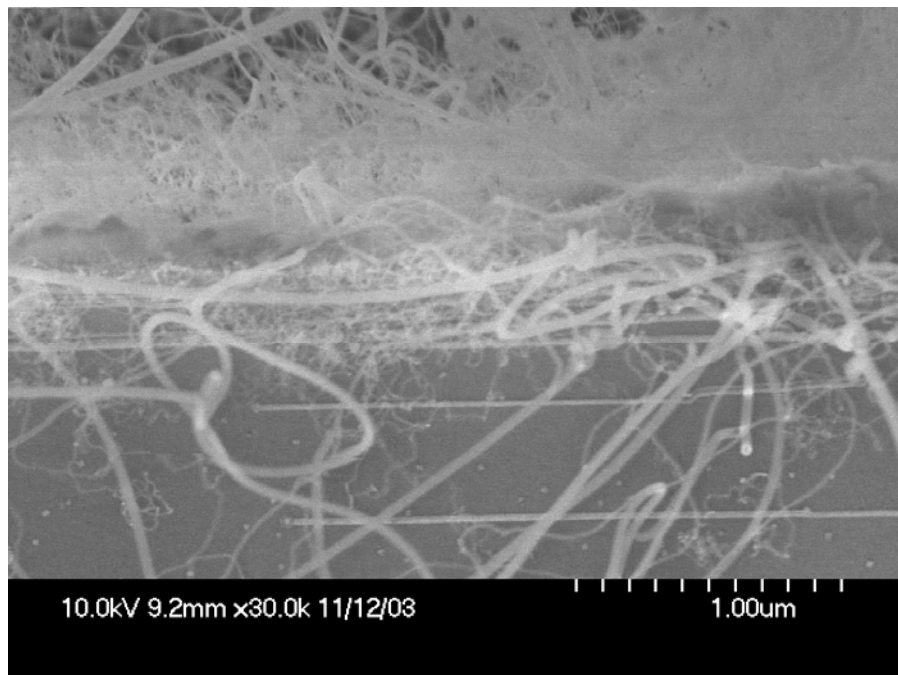
Figure 4.19. Cross-sectional SEM image of a contact composed of argon sputtered Si(15 nm)/Ni(16.4 nm)/Si(30 nm)/Ni(32.8 nm)/Si(30 nm)/Ni(32.8 nm)/SiC that has been annealed for 10 min at 1000 $^{\circ}$C. Reaction between the alternating Ni and Si layers resulted in the formation of nanowires. The substrate is crystalline SiC.
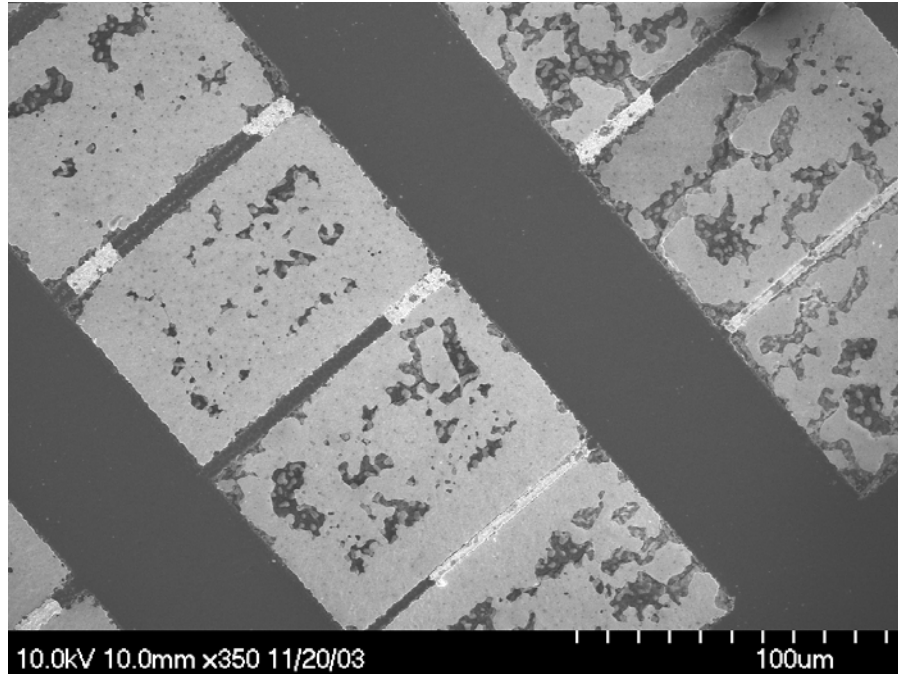
Figure 4.20. Plan view SEM image of a contact composed of argon sputtered Si(15 nm)/Ni(16.4 nm)/Si(30 nm)/Ni(32.8 nm)/Si(30 nm)/Ni(32.8 nm)/SiC that has been capped with 250 nm gold and then annealed for 2.5 min at 1000 $^{\circ}$C. Reaction between the alternating Ni and Si layers resulted in gaps forming in the gold cap layer. The substrate is crystalline SiC.

off. In addition, many of the remaining contacts were Schottky in nature (even though the gold was deposited over an ohmic Ni/Si contact), pointing to poor Au adhesion to the Ni/Si contact.

Nichrome has also been suggested as a possible contact material, particularly showing excellent adhesion to the gold cap layer and improved bonding characteristics.[63] Chromium also can form a stable carbide (Cr_3C_2), providing a benefit similar to the presence of titanium.[70] Nichrome contacts investigated in this work (1500 Å NiCr, 500 Å Au) were ohmic ~15% of the time (similar to the Ti/Ni/Au contacts), and showed specific contact resistances comparable to the Ti/Ni contacts. Contact conductivity as a function of annealing time is shown in Fig. 4.21; results are similar to those found for the Ti/Ni contacts.

Finally, aluminum was investigated in the contacts to prevent the formation of microvoids by reacting with excess carbon to form Al_4C_3.[60] Contacts composed of 200 Å Al and 1250 Å Ni were deposited via argon sputtering, followed by 500 Å Au deposited via thermal evaporation. The argon sputtering resulted in large grains of Ni being deposited on the crystalline SiC substrate (Fig. 4.22).

Subsequent annealing resulted in a granular contact (Fig. 4.23). These contacts were Schottky when unannealed and entirely prevented any current flow after annealing for 1 min or more at 900 $^{\circ}$C.

4.3.3.1.2 Porous SiC

Upon selection of Ti/Ni/Au and Ti/NiCr/Au as the best contact materials, ohmic contact to porous SiC layers was investigated. As detailed in section 4.3.2.2, the success rate of isolated TLM pad formation on porous SiC was low, due to the inability to use sonication to aid lift off of excess metal. For this reason, TLM studies on porous SiC were only conducted for the Ti/Ni/Au contacts.

The contact was found to have good adhesion to the porous substrate. The unannealed contact fills the top layer of pores well (Fig. 4.24). Upon annealing, the contact takes on a roughened surface and continues to fill the top layer of the porous morphology (Fig. 4.25). In fact, the contact adheres to the PSiC so strongly that sonication first leads to fracture within the porous film, while the contact retains its adhesion to the top of the porous layer (Fig. 4.26). Annealing at 900-1000 $^{\circ}$C does not appear to change the morphology of the PSiC film.

When making porous SiC TLM structures, a complete row of ohmic contact pads was never fabricated. Rather, some rows would have several good pads of one spacing, another row would have a couple of good pads of another spacing, etc. Therefore, specific contact resistance data for the porous samples was determined by average resistance values from numerous different rows in order to accumulate enough data. Raw data for the resistances found with porous SiC are given in Table 4.3. Using the data presented in Table 4.3, the specific contact resistance of the contacts to porous SiC is found to be 5.5 x 10^{-4} Ω cm^2 (Fig. 4.27).

4.3.3.2 Device Behavior

Crystalline devices displayed total resistances across the wafer always near 1-3 Ω. Of the porous devices tested, total resistances showed greater variance. When the contact was formed from Ti/Ni/Au, measured total resistances included 3 Ω, 40 Ω, 55 Ω, 161 Ω, and 185 Ω. The one device formed from a
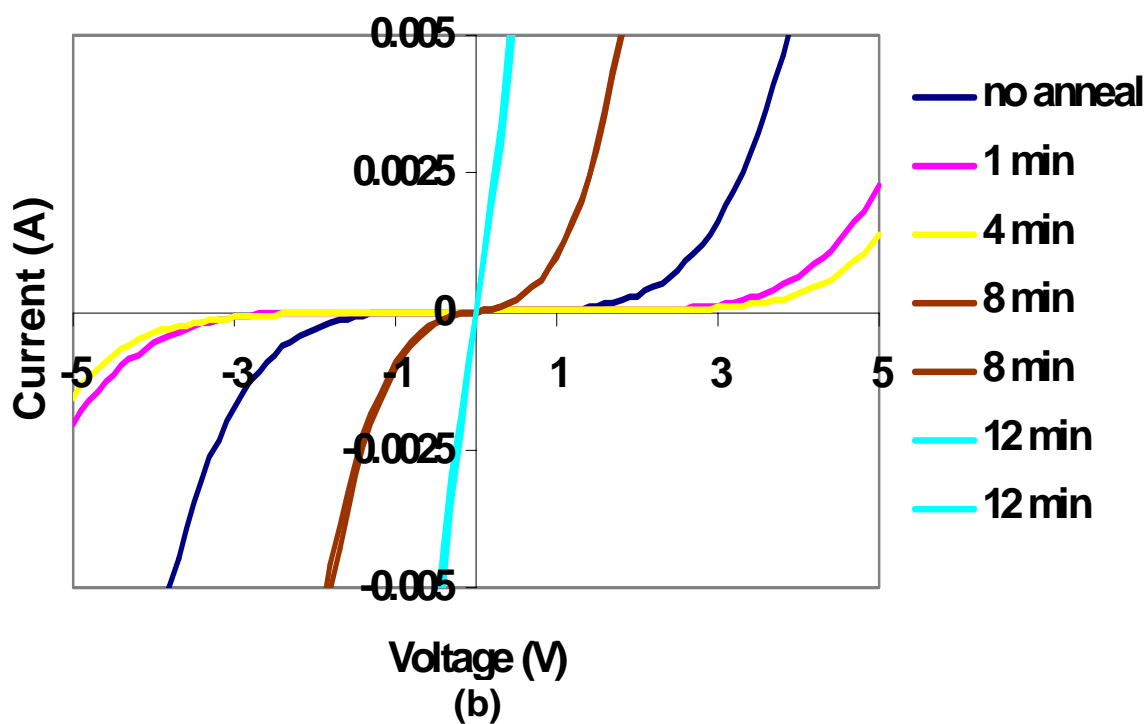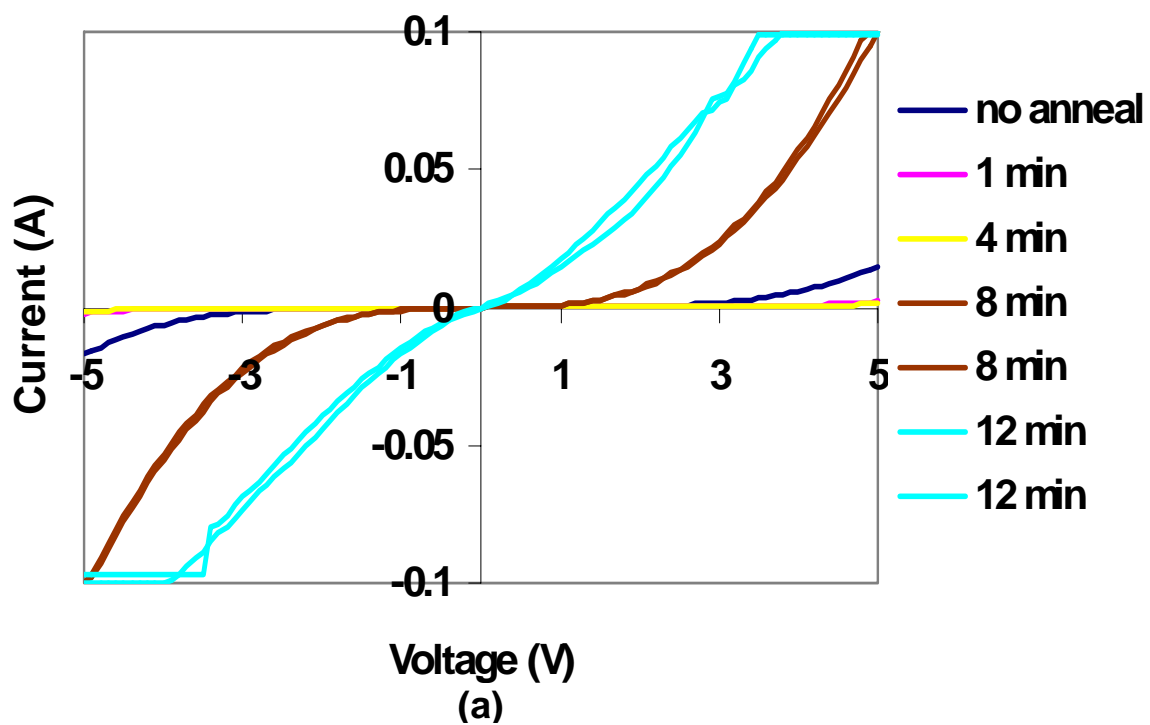
Figure 4.21. I/V curves for contacts composed of 1500 Å NiCr and 500 Å Au annealed at 900 °C for the times indicated. The substrate is crystalline SiC. (a) is shown in full scale, while (b) has the current scale enlarged to show detail.
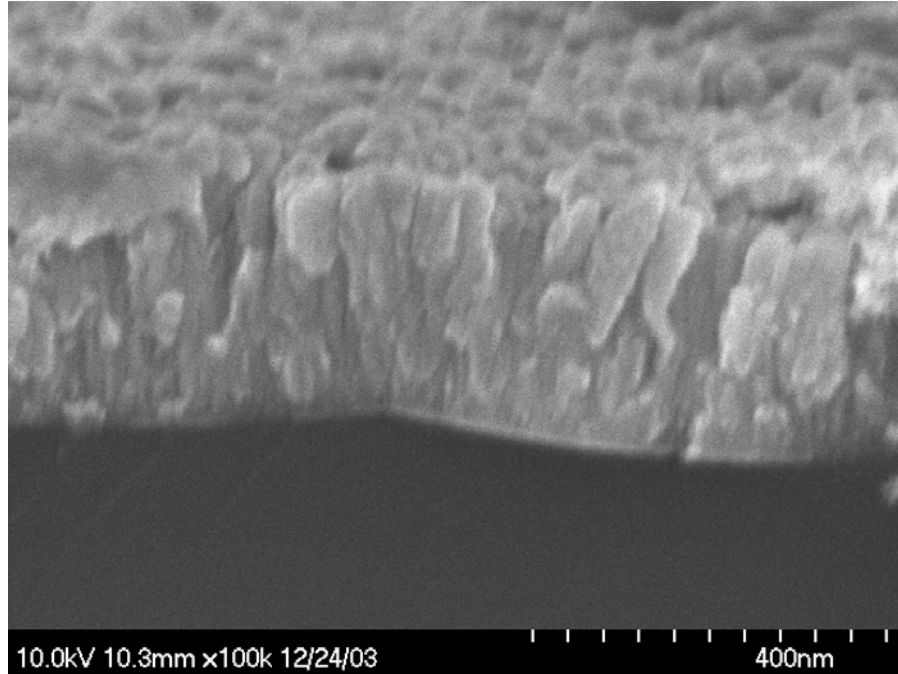
Figure 4.22. Cross-sectional SEM image of an unannealed contact composed of argon sputtered Al (200 Å) and Ni (1250 Å) followed by 500 Å Au deposited via thermal evaporation. The substrate is crystalline SiC.
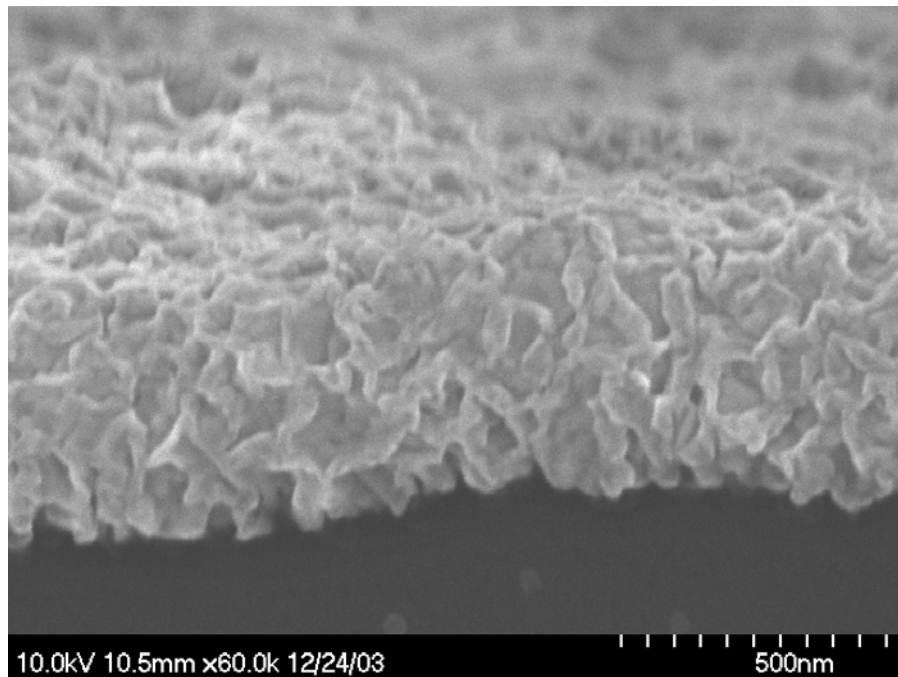
Figure 4.23. Cross-sectional SEM image of a contact composed of argon sputtered Al (200 Å) and Ni (1250 Å) followed by 500 Å Au deposited via thermal evaporation. The contact has been annealed at 900 ^{o}C for 1 min. The substrate is crystalline SiC.
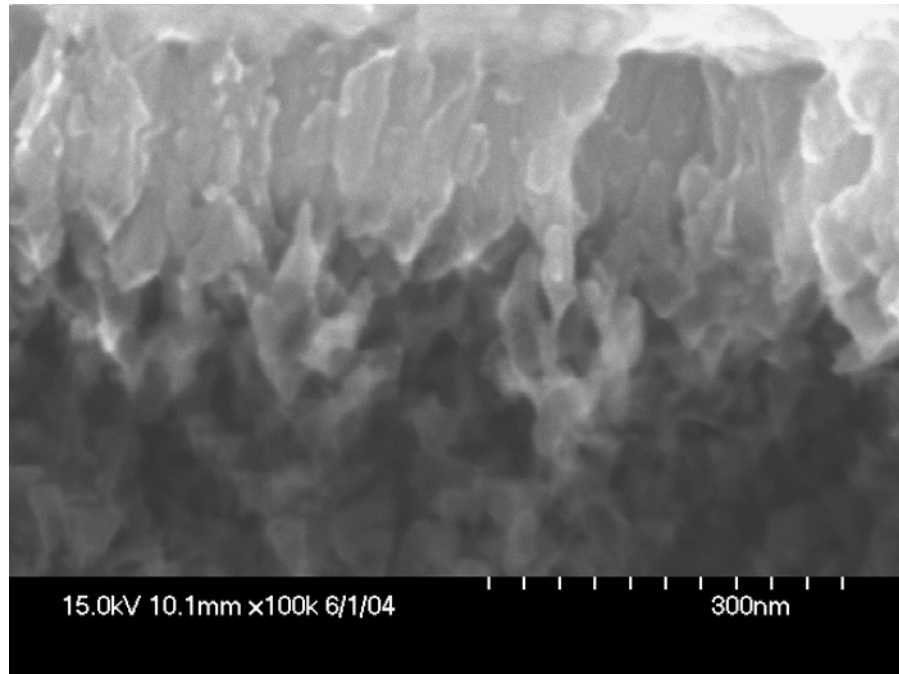
Figure 4.24. Cross-sectional SEM image of an unannealed contact composed of 50 Å Ti, 1500 Å Ni, and 500 Å Au. The substrate is porous SiC.
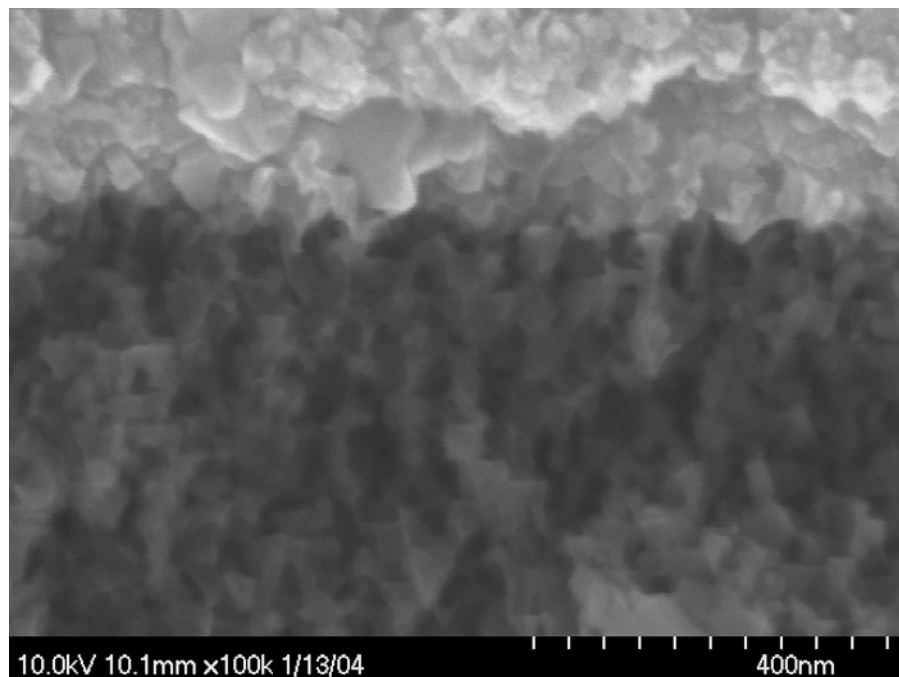
Figure 4.25. Cross-sectional SEM image of a contact composed of 50 Å Ti, 1500 Å Ni, and 500 Å Au, annealed at 900 $^{\circ}$C for 5 min. The substrate is porous SiC. Notice the macroscopic adhesion of the metal contact to the porous morphology.
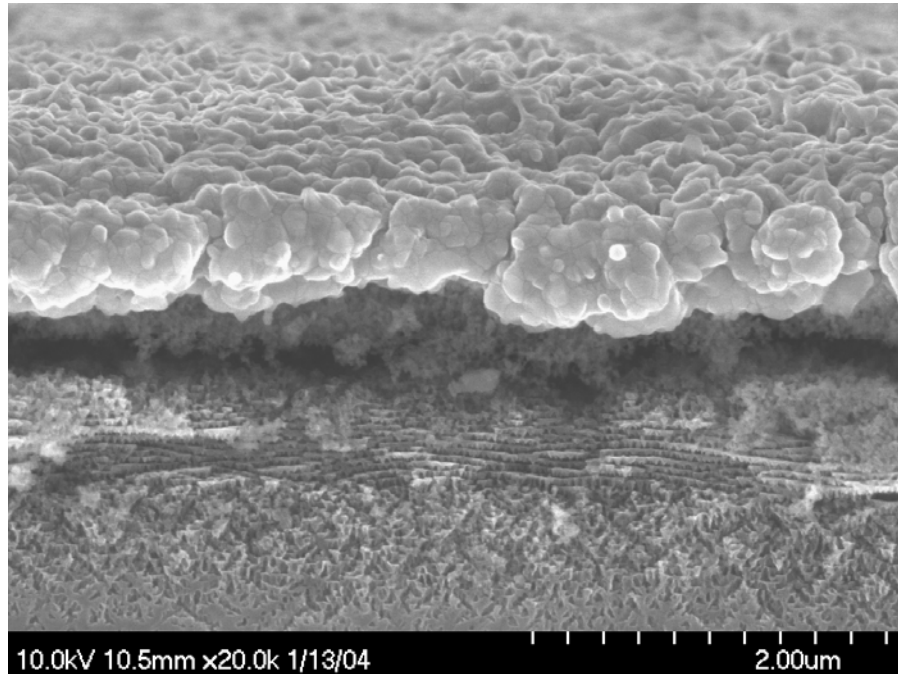
Figure 4.26. Cross-sectional SEM image of a contact composed of 50 Å Ti, 1500 Å Ni, and 500 Å Au annealed at 900 $^{\circ}$C for 5 min. The substrate is porous SiC, and the sample has been sonicated to aid in metal lift off. Notice how sonication has lead to fracture of the porous layer, but the contact remains adhered to the porous morphology.
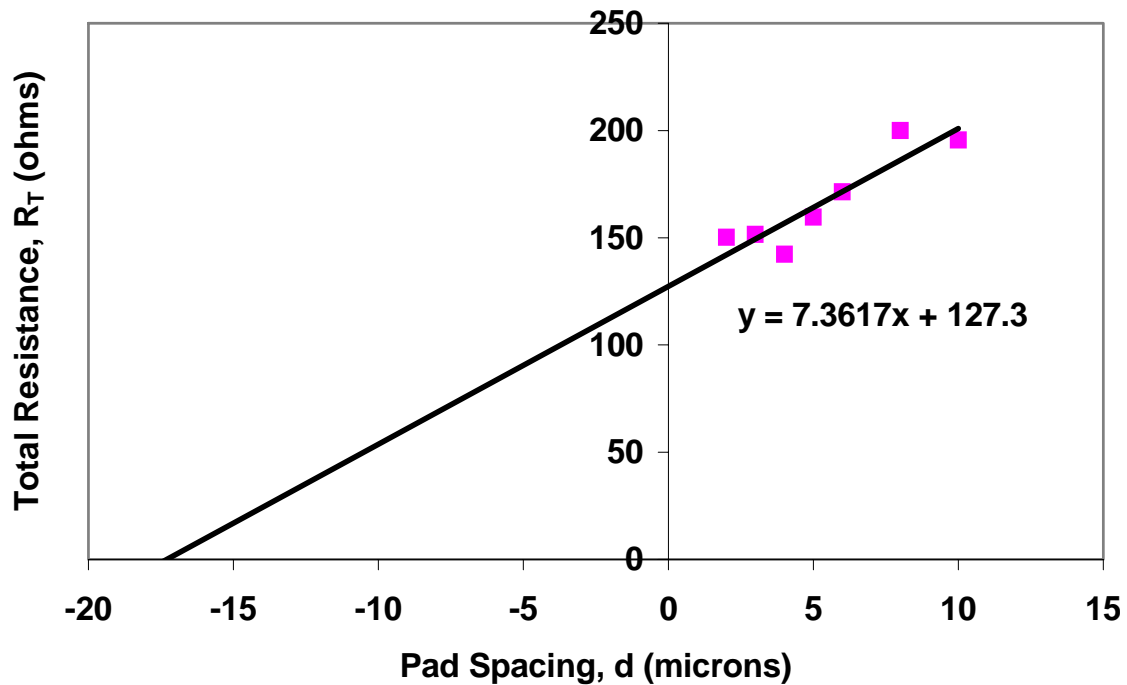
Figure 4.27. TLM data collected from a row of contact pads composed of 50 Å Ti, 1500 Å Ni, and 500 Å Au annealed at 900 $^{\circ}$C for 10 min. The substrate is porous SiC. Analysis of the data according to Eqs. 4.2-4.5 yields a specific contact resistance of 5.5 x 10^{-4} Ω cm^2 for these contacts.

Table 4.3. Raw Data for the Resistance of Different Pad Spacings
During TLM Studies of Ti/Ni/Au Contacts on Porous SiC

Pad Spacing (μm)	Measured Resistance (Ω)
2	144, 165, 149, 143
3	153, 157, 126, 159, 163
4	125, 154, 184, 134, 115
5	165, 143, 170, 174, 146
6	146, 156, 187, 185, 183
8	187, 207, 203, 209, 194
10	203, 211, 171, 189, 204

Ti/NiCr/Au contact had a total resistance of 6 Ω. As a source of comparison, a Schottky (unannealed)

Ti/Ni/Au contact showed a resistance of 285 Ω across a PSiC device at 300 mV applied potential.

When exposed to a constant (250 sccm) flow of nitrogen gas and heated from 25-500 ^{o}C,

crystalline and porous SiC devices behaved as shown in Table 4.4.

Table 4.4 Response of SiC Sensors to Temperature Increases in an Ambient of Pure N_2

Sample	Contact	Change in resistance	
		25 – 250 ^{o}C	25 – 500 ^{o}C
Crystalline SiC	(1) Ohmic Ti/Ni/Au	(1) 0.9% decrease	(1) 4.8% decrease
	(2) Ohmic Ti/Ni/Au	(2) 6.3% decrease	(2) 12.0% decrease
	(3) Ohmic Ti/Ni/Au	(3) 0.3% increase	(3) 4.7% increase
Porous SiC	(1) Ohmic Ti/Ni/Au	(1) 15.1% decrease	(1) 45.5% decrease
	(2) Ohmic Ti/Ni/Au	(2) 29.4% decrease	(2) 42.7% decrease
	(3) Ohmic Ti/NiCr/Au	(3) 20.7% decrease	(3) 34.5% decrease

The data in Table 4.4 indicates that the SiC wafer is behaving as an intrinsic semiconductor for

the most part (except for the one crystalline sample that experienced an increase in resistance upon

heating). This behavior is to be expected if the donor levels are relatively shallow (< 25 meV), as nearly

all of the donor electrons would already be in the conduction band at room temperature and therefore

intrinsic behavior would result. Previous results in the literature support this possibility.[85,86] Moore[85]

shows that the binding energy of nitrogen donors in cubic SiC is 54 meV, as confirmed by photoluminescence studies. However, conductivity studies confirm the existence of another donor at < 20 meV, which could arise from a variety of sources. First, the shallow donor energy level may be due to higher concentration pockets of nitrogen donors. Lin[87] showed that at concentrations higher than 2.5 x 10^{18} cm^{-3} (slightly less doped than our wafer), arsenic in silicon (whose binding energy approximates that of N in SiC) showed a similar reduction in binding energy. Alternatively, the shallow donor level could be due to the existence of D$^-$ (overcharged nitrogen) centers or donor complexes. Nitrogen in the vicinity of inversion domain boundaries or some other source of excess electrons could create the necessary D$^-$ centers.[85]

The data in Table 4.4 also indicates that the resistance of the porous devices is much more sensitive to changes in the temperature of the surrounding gas. One possible explanation for this phenomenon is the presence of deep (on the order of a few hundred meV below the conduction band edge) traps. It is entirely plausible that the crystalline material has very few deep traps, but that the porous material has many more as a result of the anodization process. If the electrochemical etching produces an abundance of deep traps that are significantly populated within the porous material, then the promotion of electrons from these trap states into the conduction band could account for the decreased resistance in the porous material upon heating. Regardless of the cause, PSiC has a much larger temperature coefficient of conductivity than crystalline SiC, and this may eventually open up new avenues of temperature sensing with PSiC.

Conductivity changes as a function of exposure to hydrogen, acetone, ethanol, and pure nitrogen are presented in Table 4.5 and Table 4.6 (the hydrogen, acetone, and ethanol are diluted in N_2 to the concentrations indicated). An example of some representative data is presented in Figs. 4.28 and 4.29. The acetone, ethanol, and hydrogen tests were conducted at total flow rates of 100 sccm. Each individual resistance measurement has error bars of $\pm 0.6\%$.
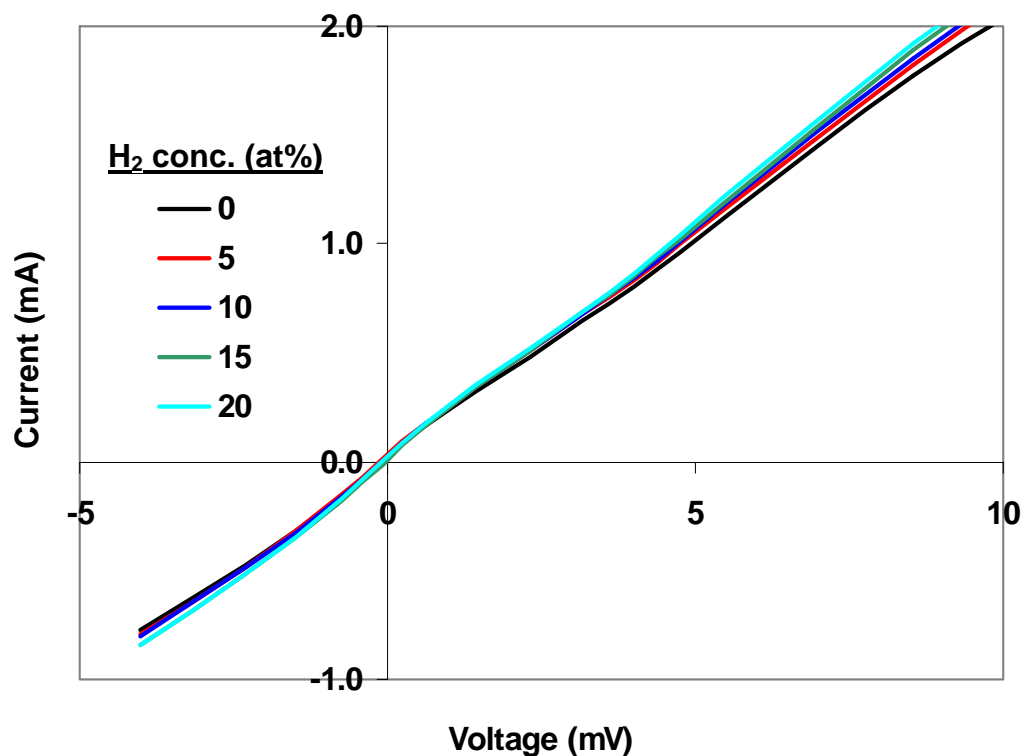
Figure 4.28. An example of conductometric data collection. This typical data shows the change in resistance of a PSiC sensor when exposed from an increasing concentration of 0-20% H_2. The H_2 is diluted in N_2 to a total flow rate of 100 sccm; the wafer is at 250 ^{o}C.
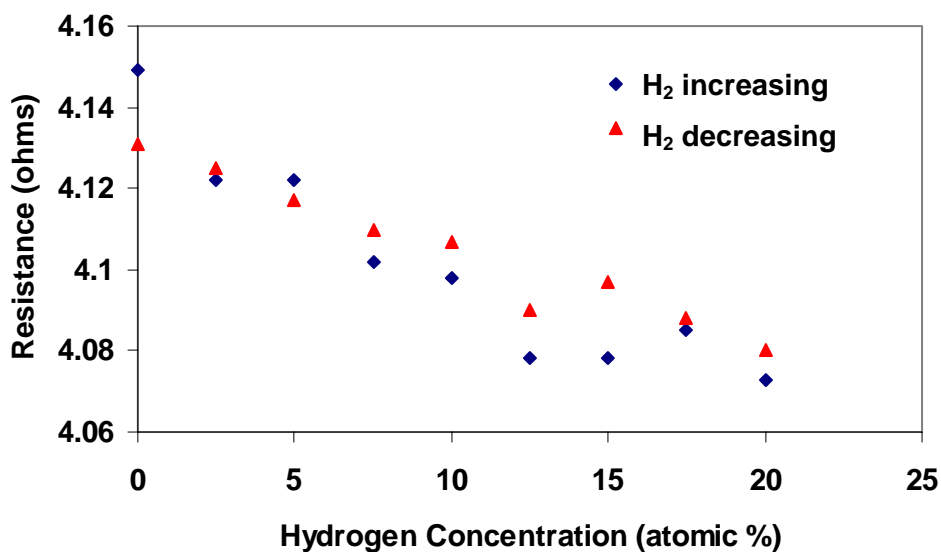
Figure 4.29. An example of conductometric data collection. This typical data shows the change in resistance of a PSiC sensor when exposed from an increasing concentration of 0-20% H_2, followed by decreasing the concentration from 20-0% H_2. The H_2 is diluted in N_2 to a total flow rate of 100 sccm; the wafer is at 250 ^{o}C.

Table 4.5. Summary of Tests in which the Device was Maintained at a <u>Constant Temperature;</u> Data from Unique Devices is Denoted by (#)

Crystalline SiC

Gas	Concentration range (at%)	Room temp	250 ^{o}C	500 ^{o}C
Acetone	0-0.85%	No response	No response	No response
Ethanol	0-0.65%	No response	No response	No response
Hydrogen	0-1.6%	No response	No response	No response
Hydrogen	0-20%	No response	No response	No response

Porous SiC

Gas	Concentration range (at%)	Room temp	250 ^{o}C	500 ^{o}C
Acetone	0-0.85%	No response	No response	No response
Ethanol	0-0.65%	No response	No response	No response
Hydrogen	0-1.6%	No response	No response	No response
Hydrogen	0-20%	No response	(1) No response	(1) ΔR = -5.1% (145 mΩ)
			(2) No response	(2) ΔR = -7.0% (321 mΩ)
			(3) ΔR = -1.2% (50 mΩ)	(3) ΔR = -5.6% (224 mΩ)

Table 4.6. Summary of Tests in which the Device was Supplied a <u>Constant Applied Heat</u> (Device Temperature was Allowed to Change as the Gas Flow was Varied); Data from Unique Devices is Denoted by (#)

Crystalline SiC

Gas	Concentration range (at%)	~250 ^{o}C	~500 ^{o}C
Acetone	0-0.85%	ΔR = +0.4% (7 mΩ); ΔT = +4.3 ^{o}C	ΔR = -0.7% (11 mΩ); ΔT = 0
Ethanol	0-0.65%	ΔR = +2.4% (42 mΩ); ΔT = +6.1 ^{o}C	ΔR = -1.0% (17 mΩ); ΔT = 0
Hydrogen	0-20%	ΔR = -1.3% (23 mΩ); ΔT = +18.6 ^{o}C	ΔR = -3.5% (60 mΩ); ΔT = +31.1 ^{o}C

Porous SiC

Gas	Concentration range (at%)	~250 ^{o}C	~500 ^{o}C
Acetone	0-0.85%	No response, ΔT = +3.8 ^{o}C	ΔR = -1.5% (32 mΩ); ΔT = 0
Ethanol	0-0.65%	No response, ΔT = +3.4 ^{o}C	No response; ΔT = 0

Hydrogen	0-1.6%	No response, $\Delta T = 0$	(1) $\Delta R = -0.9\%$ (29 mΩ); $\Delta T = 0$
			(2) $\Delta R = -0.5\%$ (16 mΩ); $\Delta T = +3.2\ ^{o}C$
Hydrogen	0-20%	(1) No response, $\Delta T = +44.8\ ^{o}C$	(1) $\Delta R = -21\%$ (388 mΩ); $\Delta T = +28\ ^{o}C$
		(2) $\Delta R = -1.2\%$ (51 mΩ); $\Delta T = +17\ ^{o}C$	(2) $\Delta R = -8.9\%$ (227 mΩ); $\Delta T = +26\ ^{o}C$

As seen in Tables 4.5 and 4.6, none of the devices were able to sense any analyte flow at room temperature. In addition, even at high temperature, neither acetone nor ethanol causes changes in the total resistance much greater than the noise for the measurements. Of course, as shown above, only small concentrations of ethanol and acetone have been investigated, as these initial experiments were conducted in order to look for low detection limits comparable to the results found from the Schottky diode sensor results in the literature. Our later studies focused on hydrogen at a wide range of concentrations due to its economic and safety considerations for NASA operations.

Examining the hydrogen data collected at constant temperature (Table 4.5), the crystalline device is unable to sense H_2 at any temperature investigated in this work. However, the PSiC sensor begins to reproducibly detect H_2 once the system is heated to 500 ^{o}C. The experiments conducted at constant applied heat (Table 4.6) verify this result, although the constant heat tests show slightly greater decreases in resistance, probably due to the additive effects of convective wafer heating (H_2 has a higher heat capacity than N_2) and changes in conduction.

Given that 20% H_2 in the gas flow yields approximately a 6% decrease in total resistance, and resistance measurements are ±0.6%, a linear response of the porous sensors would yield an estimated minimum detection limit of 2% H_2 at 500 ^{o}C. Consistent with this estimate the sensors were unable to detect 1.6% H_2 at 500 ^{o}C, yet reliably and reproducibly measured a decrease in resistance when exposed to 2.5% H_2 (the first data point in the 0-20% H_2 tests, as shown for example in Fig. 4.29).

One device was made using the same contact recipe, but was not annealed, therefore yielding a Schottky contact. For a 300 mV potential, this device yielded a 380% increase in current when heated from 25-500 $^{\circ}$C. This is a relatively large increase in signal strength when compared to the results from the ohmic contacts presented above (Table 4.4). However, it was found that the current through the Schottky device changed (decreased) from experiment to experiment, and it is possible that the heating cycles were instigating interfacial reactions within the contact layers. Like the annealed, ohmic contacts, this device did not sense H_2 flow at 250 $^{\circ}$C. The Schottky diode did experience a 14% increase in current, though, when exposed to 20% H_2 at 500 $^{\circ}$C. This result is greater than the results found for the ohmic contacts above. The increase in current could be due to the combined effects of H_2 adsorption to the semiconducting skeleton surface as well as lowering the Schottky barrier at the contact/SiC interface. However, upon a few hours of exposure to 500 $^{\circ}$C, the Schottky contact was found to fail and suffer a dramatic decrease in current.

Wide voltage sweeps (-2.5 to 2.5 V) were conducted at room temperature to compare the ohmicity of the various contacts for a wide range of potentials (Fig. 4.30). As expected, the ohmic contacts to the crystalline devices have the most linear and steepest slopes. The ohmic contacts to the porous devices show good linearity, too, although the slope is less than the crystalline ohmic contacts (indicating the higher resistances described in the beginning of this section). As expected, the Schottky (unannealed) contact to the porous device shows a dramatically decreased current flow and non-linearity.

4.3.4 Conclusions

These experiments do not address whether hydrogen absorption into the SiC crystal lattice is the root cause of the changes in conductivity found during these conductometric tests. However, studies of hydrogen passivation of SiC support this interpretation. When hydrogen absorption into the wafer is conducted at high pressure (10 bars) accompanied by high temperatures (1500-1700 $^{\circ}$C), quenching results in hydrogen-nitrogen complexes (passivation), which decrease the free carrier concentration of n-type SiC wafers,[88] because the hydrogen bonds with the extra electron on the donor nitrogen atoms. The decrease in the free carrier concentration should lead to an increase in resistance, not the decrease in
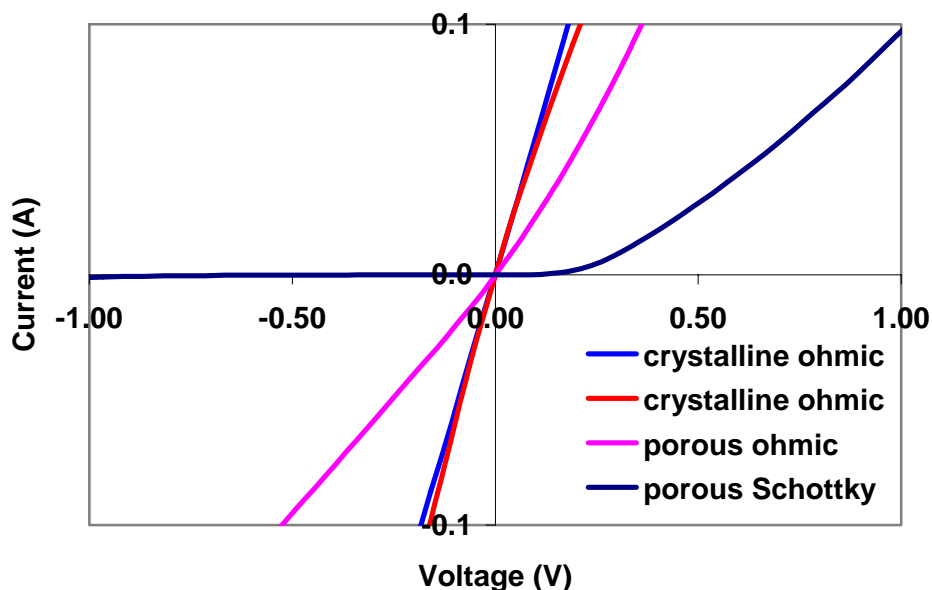
Figure 4.30. Large sweeps of current, demonstrating the properties of ohmic and Schottky contacts to both crystalline and porous SiC.

resistance observed in these studies. However, studies of SiC exposed to H_2 gas at 500 ^{o}C (a temperature closer to those used in this study), show that hydrogen is present in the bulk of the SiC, but that the hydrogen-nitrogen binding reaction is thermodynamically or kinetically impeded.[89] Furthermore, in n+ material, such as the wafers used in this study, H$^-$ is expected to be the dominant species, because the Fermi level is high and therefore the probability for the hydrogen acceptor level to be occupied is large.[89] Finally, it has been shown that atomic hydrogen is mobile in SiC even down to room temperature.[90] As a result, it is reasonable to surmise that ambient molecular hydrogen may be dissociated and absorbed into the porous semiconducting skeleton, and that hydrogen may be free to serve as an additional charge carrier.

This work indicates that PSiC conductometric sensors cannot compete with the low detection limits realized with crystalline SiC Schottky diode devices. However, the PSiC sensors may be able to fill a niche in a sensor array to quantify relatively high (> 2%) H_2 concentrations. As indicated earlier the hydrogen sensors which respond to ppm-level hydrogen loads saturate at levels far below the 2-20% range of H_2 concentration to which the PSiC sensors respond.

There are bulk sensors that are of semiconductor oxide or "hot-wire" type. In these sensors, the resistance of the sensor materials changes as the sensor surface is reduced. One architecture reported in the literature utilized SnO_2 sintered in a bead covering a Pt wire coil.[91] Due to reduction at the SnO_2 surface, the resistance of the Pt wire changes as the sensor is exposed to H_2. However, these devices still saturate at relatively low ($< 1\%$) H_2 concentrations.

Therefore, planar thermoelectric gas sensors have also been investigated.[92-96] Utilizing alumina substrates, these sensors are fabricated by partially coating a nickel oxide thick ($\sim$700 nm) film with a thin ($\sim$75 nm) film of Pt. Catalytic reactions of the Pt with hydrogen heats the platinum coated surface, and then the thermoelectric voltage builds up along the hot and cold region of the oxide film. These sensors have been shown to detect 0.025-10% H_2 in air at 80 $^{\circ}$C via relatively large ($> 100\%$) changes in voltage. However, temperature control of these devices could be an issue during implementation. For example, 3% H_2 in air shows only a 0.12 $^{\circ}$C temperature difference (and 0.087 mV signal) at room temperature.[92] In addition, the catalytic activity is highly dependent upon the oxidation state and the degree of crystallization of the thermoelectric materials. Finally, weak adhesion between the thermoelectric thick film and the substrate has been a problem.

In order to eliminate the processing concerns associated with the production of the nickel oxide layer, thermoelectric gas sensors have also been formed by partially coating a $Si_{0.8}Ge_{0.2}$ thin film with Pt.[97,98] This device exhibited a 6-10 mV potential increase when exposed to 10% H_2. However, the device has been researched primarily at temperatures below 150 $^{\circ}$C, because the device is selective toward H_2 below 150 $^{\circ}$C, but showed response to several other gases (methanol, ethanol, butane, CO, methane) at higher temperatures.

In current solid state hydrogen detection systems, a hydrogen sensitive resistor provides detection of higher hydrogen concentrations (greater than approximately 1% H_2) while a Schottky diode quantifies lower hydrogen concentrations.[99] Our results indicate that PSiC sensors could fill the void in the array of sensors for the relatively high concentrations of hydrogen detection.

In the early 1990's, thin film hydrogen resistors were composed of Pd/Ag or later Pd/Ni. The resistances of these metal films have a response proportional to the partial pressure of H_2: $\left(P_{H_2}\right)^{1/2}$. This dependence is due to the sensor detection mechanism: migration of hydrogen into the bulk of the metal changing the bulk conductance of the metal.[100] These sensors generally have low sensitivity at low hydrogen concentrations but a continued response over a wide range of hydrogen concentrations. Pd/Ni thin films were made that showed ~3% decrease in resistance when exposed to 10% H_2.[101]

Current thin film hydrogen resistors are usually composed of palladium chrome or palladium titanium alloy, as the alloys show a greater resistance to phase transformation during hydrogen absorption.[99,102] The palladium titanium alloys (71-99 at% Pd) have shown an increase in resistance of up to 16% when exposed to 100% hydrogen, and an increase in resistance of 5% when exposed to an environment of 10% hydrogen.[102] Therefore, it can be seen that the results obtained in this dissertation show magnitudes of resistance change slightly less than current high concentration hydrogen sensing via thin metallic films.

4.4 References

(1)   Zangooie, S.; Bjorklund, R.; Arwin, H. *Sens. Act. B* **1997**, *43*, 168.

(2)   Zangooie, S.; Bjorklund, R.; Arwin, H. *Thin Solid Films* **1998**, *313-314*, 825.

(3)   Zangooie, S.; Jansson, R.; Arwin, H. *J. Appl. Phys.* **1999**, *86*, 850.

(4)   Arwin, H.; Gavutis, M.; Gustafsson, J.; Schultzberg, M.; Zangooie, S.; Tengvall, P. *Phys. Status Solidi A* **2000**, *182*, 515.

(5)   Ben-Chorin, M.; Kux, A.; Schechter, I. *Appl. Phys. Lett.* **1994**, *64*, 481.

(6)   Coffer, J. L.; Lilley, S. C.; Martin, R. A.; Files-Sesler, L. A. *J. Appl. Phys.* **1993**, *74*, 2094.

(7)   Harper, J.; Sailor, M. J. *Anal. Chem* **1996**, *68*, 3713.

(8)   Song, J. H.; Sailor, M. J. *J. Am. Chem. Soc.* **1997**, *119*, 7381.

(9)   Letant, S. E.; Content, S.; Tan, T. T.; Zenhausern, F.; Sailor, M. J. *Sens. Act. B* **2000**, *69*, 193.

(10)   Starodub, V. M.; Fedorenko, L. L.; Sisetskiy, A. P.; Starodub, N. F. *Sens. Act. B* **1999**, *58*, 409.

(11)   Gao, J.; Gao, T.; Sailor, M. J. *Appl. Phys. Lett.* **2000**, *77*, 901.

(12)   Lin, V. S.; Motesharei, K.; Dancil, K. S.; Sailor, M. J.; Ghadiri, M. R. *Science* **1997**, *278*, 840.

(13)   Dancil, K. P. S.; Greiner, D. P.; Sailor, M. J. *J. Am. Chem. Soc.* **1999**, *121*, 7925.

(14)   Curtis, C. L.; Doan, V. V.; Credo, G. M.; Sailor, M. J. *J. Electrochem. Soc.* **1993**, *140*, 3492.

(15)   Gao, J.; Gao, T.; Li, Y. Y.; Sailor, M. J. *Langmuir* **2002**, *18*, 2229.

(16)   Sohn, H.; Letant, S.; Sailor, M. J.; Trogler, W. C. *J. Am. Chem. Soc.* **2000**, *122*, 5399.

(17)   Janshoff, A.; Dancil, K. P. S.; Steinem, C.; Greiner, D. P.; Lin, V. S. Y.; Gurtner, C.; Motesharei, K.; Sailor, M. J.; Ghadiri, M. R. *J. Am. Chem. Soc.* **1998**, *120*, 12108.

(18)   Letant, S. E.; Sailor, M. J. *Adv. Mater.* **2000**, *12*, 355.

(19)   Kim, S. J.; Lee, S. H.; Lee, C. J. *J. Phys. D: Appl. Phys.* **2001**, *34*, 3505.

(20)   Angelucci, R.; Poggi, A.; Dori, L.; Tagliani, A.; Cardinali, G. C.; Corticelli, F.; Marisaldi, M. *J. Porous Mat.* **2000**, *7*, 197.

(21)   Foucaran, A.; Pascal-Delannoy, F.; Giani, A.; Sackda, A.; Combette, P.; Boyer, A. *Thin Solid Films* **1997**, *297*, 317.

(22)   Han, P. G.; Wong, H.; Poon, M. C.; Wang, N. *J. Vac. Sci. Technol. A* **1999**, *17*, 1832.

(23)   Luth, H.; Thust, M.; Steffen, A.; Kordos, P.; Schoning, M. J. *Mat. Sci. Engng. B* **2000**, *B69-70*, 104.

(24)   Schechter, I.; Ben-Chorin, M.; Kux, A. *Anal. Chem* **1995**, *67*, 3727.

(25)   Taliercio, T.; Dilhan, M.; Massone, E.; Foucaran, A.; Gue, A. M.; Bretagnon, T.; Fraisse, B.; Montes, L. *Sens. Act. A* **1995**, *46-47*, 43.

(26)   George, M. A.; Ayoub, M. A.; Ila, D.; Larkin, D. J. *Mat. Res. Soc. Symp. Proc.* **1999**, *572*, 123.

(27)   Hunter, G. W.; Neudeck, P. G.; Chen, L.; Knight, D.; Liu, C. C.; Wu, Q. H. *Inst. Phys. Conf. Ser.* **1996**, *142*, 817.

(28)   Shields, V. B.; Ryan, M. A.; Williams, R. M.; Spencer, M. G.; Collins, D. M.; Zhang, D. *Inst. Phys. Conf. Ser.* **1996**, *142*, 1067.

(29)   Allan, R. *Electron. Design* **1997**, *45*, 35.

(30)   Petrova-Koch, V.; Sreseli, O.; Polisski, G.; Kovalev, D.; Muschik, T.; Koch, F. *Thin Solid Films* **1995**, *255*, 107.

(31)   Choyke, W. J. In *DURINT Conference: Nanoporous SiC and GaN*: Tampa, Florida, 2002

(32)   Sieber, N.; Mantel, B. F.; Seyller, T.; Ristein, J.; Ley, L.; Heller, T.; Batchelor, D. R.; Schmeiber, D. *Appl. Phys. Lett.* **2001**, *78*, 1216.

(33)   Nakagomi, S.; Azuma, T.; Kokubun, Y. *Electrochemistry* **2001**, *70*, 174.

(34)   Serina, F.; Ng, K. Y. S.; Huang, C.; Auner, G. W.; Rimai, L.; Naik, R. *Appl. Phys. Lett.* **2001**, *79*, 3350.

(35)   Kim, J.; Gila, B. P.; Abernathy, C. R.; Chung, G. Y.; Ren, F.; Pearton, S. J. *Solid State Electron.* **2003**, *47*, 1487.

(36)   Kim, C. K.; Lee, J. H.; Choi, S. M.; Noh, I. H.; Kim, H. R.; Cho, N. I.; Hong, C.; Jang, G. E. *Sens. Act. B* **2001**, *77*, 455.

(37)   Svenningstorp, H.; Tobias, P.; Lundstrom, I.; Salomonsson, P.; Martensson, P.; Ekedahl, L. G.; Spetz, A. L. *Sens. Act. B* **1999**, *57*, 159.

(38)   Roy, S.; Jacob, C.; Lang, C.; Basu, S. *J. Electrochem. Soc.* **2003**, *150*, H135.

(39)   Chen, L.; Hunter, G. W.; Neudeck, P. G.; Knight, D. *Solid State Electron.* **1998**, *42*, 2209.

(40)   Chen, L.; Hunter, G. W.; Neudeck, P. G.; Bansal, G.; Petit, J. B.; Knight, D. *J. Vac. Sci. Technol. A* **1997**, *15*, 1228.

(41)   Hunter, G. W.; Neudeck, P. G.; Gray, M.; Androjna, D.; Chen, L.; Hoffman, R. W.; Liu, C. C.; Wu, Q. H. *Mat. Sci. Forum* **2000**, *338-342*, 1439.

(42)   Hunter, G. W.; Neudeck, P. G.; Chen, L. Y.; Knight, D.; Liu, C. C.; Wu, Q. H. *Mat. Sci. Forum* **1998**, *264-268*, 1093.

(43)   Nakagomi, S.; Shindo, Y.; Kokubun, Y. *Phys. Stat. Sol. (A)* **2001**, *185*, 33.

(44)   Xu, J. P.; Lai, P. T.; Zhong, D. G.; Chan, C. L. *IEEE Electron Dev. Lett.* **2003**, *24*, 13.

(45)   Schalwig, J.; Kreisl, P.; Ahlers, S.; Muller, G. *IEEE Sens. J.* **2002**, *2*, 394.

(46)   Spetz, A. L.; Uneus, L.; Svenningstorp, H.; Tobias, P.; Ekedahl, L. G.; Larsson, O.; Goras, A.; Savage, S.; Harris, C.; Martensson, P.; Wigren, R.; Salomonsson, P.; Haggendahl, B.; Ljung, P.; Mattsson, M.; Lundstrom, I. *Phys. Stat. Sol. (A)* **2001**, *185*, 15.

(47)   Jin, Z. H.; Zhou, H. J.; Jin, Z. L.; Savinell, R. F.; Liu, C. C. *Sens. Act. B* **1998**, *52*, 188.

(48)   Kim, C. K.; Lee, J. H.; Lee, Y. H.; Cho, N. I.; Kim, D. J. *Sens. Act. B* **2000**, *66*, 116.

(49)   Samman, A.; Gebremariam, S.; Rimai, L.; Zhang, X.; Hangas, J.; Auner, G. W. *J. Appl. Phys.* **2000**, *87*, 3101.

(50)   Roy, S.; Jacob, C.; Basu, S. *Sens. Act. B* **2003**, *94*, 298.

(51)   Hunter, G. W.; Chen, L.; Neudeck, P. G.; Knight, D.; Liu, C.; Wu, Q.; Zhou, H. *NASA Technical Memorandum 107444* **1997**.

(52)   Cole, M. W.; Joshi, P. C.; Hubbard, C.; Demaree, J. D.; Ervin, M. *J. Appl. Phys.* **2002**, *91*, 3864.

(53)   Hultman, L.; Ljungcrantz, H.; Hallin, C.; Janzen, E.; Sundgren, J. E.; Pecz, B.; Wallenberg, L. R. *J. Mater. Res.* **1996**, *11*, 2458.

(54)   Lu, W.; Mitchel, W. C.; Thornton, C. A.; Collins, W. E.; Landis, G. R.; Smith, S. R. *J. Electrochem. Soc.* **2003**, *150*, G177.

(55)   Okojie, R. S.; Lukco, D.; Chen, Y. L.; Spry, D. J. *J. Appl. Phys.* **2002**, *91*, 6553.

(56)   Porter, L. M.; Davis, R. F. *Mat. Sci. Engng. B* **1995**, *B34*, 83.

(57)   van de Lagemaat, J.; Vanmaekelbergh, D.; Kelly, J. J. *J. Appl. Phys.* **1998**, *83*, 6089.

(58)   Chen, J. S.; Bachli, A.; Nicolet, M. A.; Baud, L.; Jaussaud, C.; Madar, R. *Mat. Sci. Engng. B* **1995**, *29*, 185.

(59)   Crofton, J.; Barnes, P. A.; Williams, J. R.; Edmond, J. A. *Appl. Phys. Lett.* **1993**, *62*, 384.

(60)   Hallin, C.; Yakimova, R.; Pecz, B.; Georgieva, A.; Marinova, T. S.; Kasamakova, L.; Kakanakov, R.; Janzen, E. *J. Electron. Mater.* **1997**, *26*, 119.

(61)   Jang, T.; Porter, L. M.; Rutsch, G. W. M.; Odekirk, B. *Appl. Phys. Lett.* **1999**, *75*, 3956.

(62)   Levit, M.; Grimberg, I.; Weiss, B. Z.; Eizenberg, M. *Mat. Res. Soc. Symp. Proc.* **1996**, *423*, 125.

(63)   Luckowski, E. D.; Williams, J. R.; Bozack, M. J.; Isaacs-Smith, T.; Crofton, J. *Mat. Res. Soc. Symp. Proc.* **1996**, *423*, 119.

(64)   Lundberg, N.; Ostling, M. *Solid State Electron.* **1995**, *38*, 2023.

(65)   Schmid, U.; Getto, R.; Sheppard, S. T.; Wondrak, W. *J. Appl. Phys.* **1999**, *85*, 2681.

(66)   Crofton, J.; McMullin, P. G.; Williams, J. R.; Bozack, M. J. *J. Appl. Phys.* **1994**, *77*, 1317.

(67)   Uemoto, T. *Jpn. J. Appl. Phys.* **1995**, *34*, L7.

(68)   Kakanakova-Georgieva, A.; Marinova, T.; Noblanc, O.; Arnodo, C.; Cassette, S.; Brylinski, C. *Thin Solid Films* **1999**, *343-344*, 637.

(69)   Dezauzier, C.; Becourt, N.; Arnaud, G.; Contreras, S.; Ponthenier, J. L.; Camassel, J.; Robert, J. L.; Pascual, J.; Jaussaud, C. *Sens. Act. A* **1995**, *46-47*, 71.

(70)   Liu, S.; Reinhardt, K.; Severt, C.; Scofield, J. *Inst. Phys. Conf. Ser.* **1996**, *142*, 589.

(71)   Marinova, T.; Kakanakova-Georgieva, A.; Krastev, V.; Kakanakov, R.; Neshev, M.; Kassamakova, L.; Noblanc, O.; Arnodo, C.; Cassette, S.; Brylinski, C.; Pecz, B.; Radnoczi, G.; Vincze, G. *Mat. Sci. Engng. B* **1997**, *B46*, 223.

(72)   Pecz, B.; Radnoczi, G.; Cassette, S.; Brylinski, C.; Arnodo, C.; Noblanc, O. *Diamond Relat. Mater.* **1997**, *6*, 1428.

(73)   Pecz, B. *Appl. Surf. Sci.* **2001**, *184*, 287.

(74)   Pecz, B. *Phys. Stat. Sol. (A)* **2003**, *195*, 214.

(75)   Gasser, S. M.; Bachli, A.; Garland, C. M.; Kolawa, E.; Nicolet, M. A. *Microelectron. Eng.* **1997**, *37/38*, 529.

(76)   Wu, K. H.; Fang, Y. K.; Hsieh, W. T.; Ho, J. J.; Lin, W. J.; Hwang, J. D. *Electron. Lett.* **1998**, *34*, 2243.

(77)   Ronkel, F.; Schultze, J. W.; Arens-Fischer, R. *Thin Solid Films* **1996**, *276*, 40.

(78)   Gole, J. In *MRS Bulletin*, 2003; Vol. 28, p 263-28.

(79)   Kang, C.; Kang, M.; Lee, C.; Paek, S.; Hong, S.; Min, N. *J. Korean Phys. Soc.* **2003**, *42*, S719.

(80)   Crofton, J.; Porter, L. M.; Williams, J. R. *Phys. Stat. Sol. (B)* **1997**, *202*, 581.

(81)   Cox, R. H.; Strack, H. *Solid State Electron.* **1967**, *10*, 1213.

(82)   Schroder, D. K. *Semiconductor Material and Device Characterization*; John Wiley and Sons, Inc.: New York, 1990.

(83)   Chaddha, A. K.; Parsons, J. D.; Kruaval, G. B. *Appl. Phys. Lett.* **1995**, *66*, 760.

(84)   Goesmann, F.; Schmid-Fetzer, R. *Mat. Sci. Engng. B* **1997**, *B46*, 357.

(85)   Moore, W. *J. Appl. Phys.* **1993**, *74*, 1805.

(86)   Weingartner, R.; Albrecht, A.; Wellmann, P. J.; Winnacker, A. *Mat. Sci. Forum* **2003**, *433-436*, 341.

(87)   Lin, A. L. *Appl. Phys. Lett.* **1988**, *53*, 766.

(88)   Gendron, F.; Porter, L. M.; Porte, C.; Bringuier, E. *Appl. Phys. Lett.* **1995**, *67*, 1253.

(89)   Theys, B.; Gendron, F.; Porte, C.; Bringuier, E.; Dolin, C. *J. Appl. Phys.* **1997**, *82*, 6346.

(90)   Achtziger, N.; Hulsen, C.; Janson, M.; Linnarsson, M. K.; Svensson, B. G.; Witthuhn, W. *Mat. Sci. Forum* **2000**, *338-342*, 933.

(91)   Katsuki, A.; Fukui, K. *Sens. Act. B* **1998**, *52*, 30.

(92)   Shin, W.; Imai, K.; Izu, N.; Murayama, N. *Jpn. J. Appl. Phys.* **2001**, *40*, L1232.

(93)   Matsumiya, M.; Qiu, F.; Shin, W.; Izu, N.; Murayama, N.; Kanzaki, S. *Thin Solid Films* **2002**, *419*, 213.

(94)   Shin, W.; Matsumiya, M.; Qiu, F.; Izu, N.; Murayama, N. *Sens. Act. B* **2004**, *97*, 344.

(95)   Matsumiya, M.; Shin, W.; Izu, N.; Murayama, N. *Sens. Act. B* **2003**, *93*, 309.

(96)   Shin, W.; Matsumiya, M.; Qiu, F.; Izu, N.; Murayama, N. *J. Ceram. Soc. Jpn.* **2002**, *110*, 995.

(97)   Qiu, F.; Shin, W.; Matsumiya, M.; Izu, N.; Murayama, N. *Jpn. J. Appl. Phys.* **2003**, *42*, 1563.

(98)   Qiu, F.; Matsumiya, M.; Shin, W.; Izu, N.; Murayama, N. *Sens. Act. B* **2003**, *94*, 152.

(99)   Hunter, G. W.; Neudeck, P. G.; Makel, D.; Liu, C. C.; Ward, B.; Wu, Q. H.; Thomas, V.; Dutta, P.; Frank, M.; Trimbol, J.; Fulkerson, M.; Patton, B. In *IEEE Sensors 2002*; Institute of Electrical and Electronics Engineers: Orlando, FL, **2002**; Vol. 2, 1126.

(100)   Hunter, G. W.; Liu, C.; Makel, D. B. "Microfabricated Chemical Sensors for Aerospace Applications." In *MEMS Handbook*; Gad-el-Hak, M., Ed.; CRC Press LLC: Boca Raton, **2002**, pp 22/1-22/24.

(101)   Hughes, R. C.; Schubert, W. K. *J. Appl. Phys.* **1992**, *71*, 542.

(102)   Hunter, G. W. 1996. PdTi Metal Alloy as a Hydrogen or Hydrocarbon Sensitive Material. US Patent 5,520,753, filed Dec. 30, 1994, and issued May 28, 1996.

CHAPTER 5

FUTURE DIRECTIONS

5.1 Electroless Etching

There are many etching parameters that can be manipulated during electroless etching, such as the identity of the metal catalyst, the etchant composition, etc. However, the primary factor that determines the morphology of electrolessly etched PSiC is determined before etching even begins: the quality of the starting SiC wafer. Current SiC production is simply still in the research phase, and the growth of pure, defect-controlled SiC is not available with today's technology and growth techniques. An example of current deficiencies is our 4H-SiC wafer with its preponderance of 6H regions. In addition, dopant concentrations often differ by more than an order of magnitude between the center of a 2" wafer and its edges. Relatively high concentrations of dopants such as boron and nitrogen are present in all commercially available wafers today except for the purist (and most expensive) of growth conditions.

But the wafer characteristic that appears to most determine the resulting PSiC morphology is defect structure and concentration. The concentration of micropipes has decreased dramatically in recent years, but even now micropipe densities on the order of 100 pipes/cm^2 or less are difficult to obtain in bulk wafers. Simple edge and screw dislocation densities are much higher than this number, and are much greater than the dislocation densities obtained in the mature Si production. This research showed that the morphology of the porous structure is highly dependent upon the micropipes and defects (both stacking faults and threading dislocations) in the SiC wafer. Once the impurity fluctuations and defect concentrations in crystalline SiC wafers can be controlled and minimized, electroless etching of PSiC can begin in earnest.

5.2 Further Characterization of Porous SiC

An additional spectroscopic characterization technique of PSiC that could prove useful is near-field scanning optical microscopy (NSOM). NSOM would allow for simultaneous correlation of light emission and scattering properties with the morphology of the porosity. Therefore, further correlations

could be made in regard to the origin of spectral emission from PSiC. In addition, NSOM would permit the collection of photoluminescent data that is much more localized to the surface region of the PSiC film.

Two-phonon Raman studies may also prove useful if porous SiC layers are ever developed into temperature sensors.[1-3] Two-phonon Raman experiments would probe the local phonon density of states, which directly determines the thermal conductivity of the material. Thermal conductivity is obviously an important material parameter to know accurately in order to form a temperature sensor. Therefore, the phonon density of states could be mapped as a function of etching conditions. This information would be particularly useful for studies being performed by a collaborator at UIUC, in which the flexing of interdigitated arrays of porous SiC cantilevers is being monitored as a temperature detector.

5.3 High Temperature Sensing with PSiC

All of the porous sensors in this work were anodically etched with the same conditions (current, time, and therefore porous film thickness). Experiments should be conducted in which the etching current is varied between sensors, as varying the current could alter both the porous morphology to a limited degree as well as possibly the surface termination (including the presence of dangling bonds). In addition, anodically etching for longer times in order to produce thicker porous films could lower the detection limit of these sensors.

Making ohmic electrical contact directly to porous SiC is still an art in need of improvement. Lift off of excess metal continued to be a problem throughout this work. There are a variety of processing parameters that can be manipulated during contact formation; however, the single most useful alteration would probably be the use of a thick photoresist. Coupled with the correct developer to form sharp ("boat dock") features, lift off of excess metal from porous regions could be greatly enhanced. When one of the devices that had poor lift off was examined in SEM, it was found that the photoresist had dissolved, but that the overlying metal was so thick that the metal remained suspended over an area that should have become bare (Fig. 5.1).

The initial response time as well as the relaxation time of the sensor to nominal conditions after the H_2 flow was stopped was not investigated in this work. Rather, as the H_2 concentration was
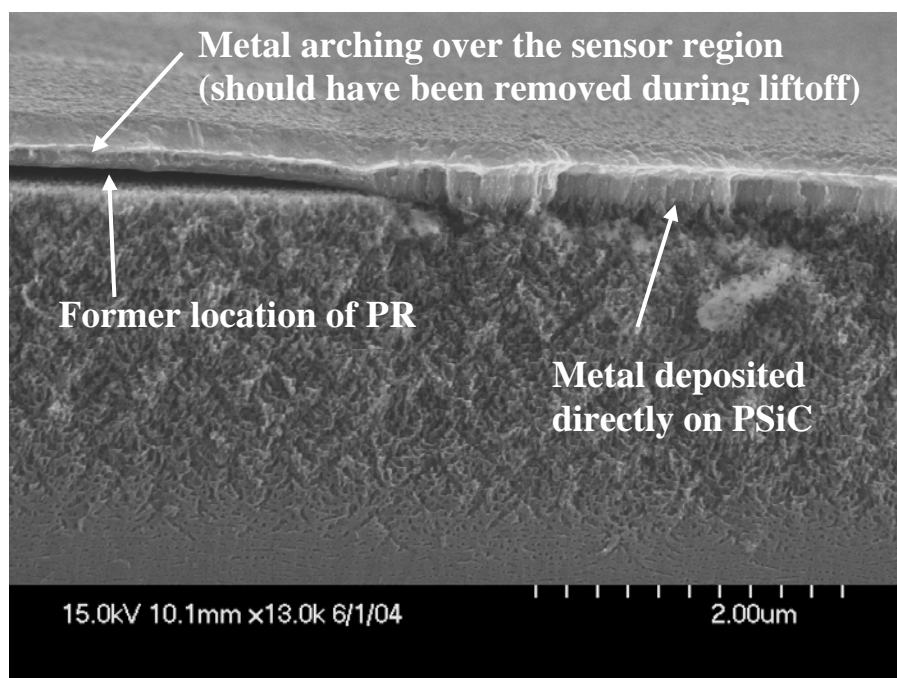
125

Fig. 5.1 Cross-sectional SEM image of a contact composed of 50 Å Ti, 1500 Å Ni, and 2500 Å Au. The region on the right of the image is the location where the contact metal is bonded directly to the PSiC and should remain after lift off. The region in the left of the image is the location in which photoresist existed so that lift off would remove this metal. The metallization is too thick for the photoresist and has bridged the gap where the photoresist dissolved away during lift off.

manipulated, the sensor was simply given an adequate (5 min) time to equilibrate to the new gas flow condition. Transient condition time responses could be conducted by applying a steady voltage and monitoring the change in current with time. This would require the construction of a smaller flow cell that could allow for immediate exposure of the sensor to the new flow conditions, as the relatively large flow cell used in this work was designed for simultaneous interferometry and conductivity studies. Results of these studies could also elucidate whether changes in conductivity are due to adsorption to the surface or absorption into the lattice.

As noted in Chapter 4, the Schottky diode sensors detailed in the literature behave quite differently depending upon whether the gas flow is fuel rich or fuel lean. No experiments were conducted in this work with O_2 in the flow with the H_2. The presence of oxygen in the gas flow may not change the response of these PSiC sensors considering that (1) a stable native oxide already exists on the sensors

investigated in this work, and (2) these sensors proved insensitive to low concentrations of acetone and ethanol. Experiments with both fuel rich and fuel lean conditions should be conducted to verify this hypothesis.

Furthermore, experiments with higher concentrations of other hydrogen-containing species (such as ethanol) should be conducted. This work only investigated low concentrations (< 1%) of ethanol and acetone in order to compare the response of the PSiC sensors to the Schottky sensors detailed in the literature. However, as our future H_2 tests showed, the PSiC sensors respond to only relatively large concentrations of ambient hydrogen. The PSiC sensors may also be able to detect relatively large concentrations of hydrocarbons.

Buriak and Allen showed that the hydrosilylation of alkynes and alkenes to porous Si produced remarkably stable surfaces.[4] The PSi surface was partially covered with the covalently bound vinyl/alkyl groups, and the original Si-H porous surface termination remained to some degree. However, the Si-H surface appeared to be effectively capped, as exposure of the PSi to HF and KOH did not result in oxide formation or dissolution of the porous film. A similar surface treatment may be beneficial in producing PSiC sensors. It may be possible to anodically etch a bulk SiC wafer to form PSiC, immediately followed by a surface treatment that continues to permit H_2 adsorption on the surface, yet is resistant to oxidation. A PSiC surface that is resistant to oxidation, yet still responsive to H_2 in the surrounding environment, would be an extremely powerful sensor for the ever-changing fuel/oxygen ratios found in an engine's exhaust.

5.4 References

(1)   Windl, W.; Karch, K.; Pavone, P.; Schutt, O.; Strauch, D.; Weber, W. H.; Hass, K. C.; Rimai, L. *Phys. Rev. B* **1994**, *49*, 8764.

(2)   Burton, J. C.; Sun, L.; Long, F. H.; Feng, Z. C.; Ferguson, I. T. *Phys. Rev. B* **1994**, *59*, 7282.

(3)   Hofmann, M.; Zywietz, A.; Karch, K.; Bechstedt, F. *Phys. Rev. B* **1994**, *50*, 13401.

(4)   Buriak, J. M.; Allen, M. J. *J. Am. Chem. Soc.* **1998**, *120*, 1339.

QUANTUM CONFINEMENT FIT MATHEMATICA CODE

```
C = 1.5117;  (* NANOMETERS  *)

GAMMA0 = 11.80;  (*  INVERSE CM  *)

<< STATISTICS`DATASMOOTHING`;

OMEGASQ[Q_] := 657500 + 270000 COS[PI Q/2];

OMEGA[Q_] := SQRT[OMEGASQ[Q]];

CC0[Q_, L_] := EXP[-Q^2 L^2 /(4*C^2)];  (* L IN UNITS OF NANOMETERS  *)

INTEGRAND[Q_, W_, L_] := 4 PI (Q^2) CC0[Q, L]/((W - OMEGA[Q])^2 + (GAMMA0/2)^2);

INTENSITY[W_, L_] := NINTEGRATE[INTEGRAND[Q, W, L], {Q, 0, 1}];


(*  FUNCTIONS TO SELECT AND SMOOTH DATA  *)

TERMFIND[DATA_, VALUE_] := (

   FOR[JJ = 1, JJ ≤ LENGTH[DATA], JJ++,

    IF[DATA[[JJ]][[1]] < VALUE, COUNTER = JJ, BREAK]

   ];

   COUNTER

  );

PEAKFIND[DATA_] := {DATA[[(POSITION[DATA, MAX[DATA]][[1]][[1]])]][[1]],

      DATA[[(POSITION[DATA, MAX[DATA]][[1]][[1]])]][[2]]};

SMOOTHDATA[DATA_, TERMS_, FIRST_, LAST_] := (

   SMOOTH = MOVINGAVERAGE[DATA, TERMS];

   TABLE[SMOOTH[[N]], {N, FIRST, LAST}]

  );

SMOOTHWAVE[DATA_, TERMS_, LOWLAM_, HIGHLAM_] := (
```

```
    FIRST = TERMFIND[DATA, LOWLAM];

    LAST = TERMFIND[DATA, HIGHLAM] + 1;

    SMOOTHDATA[DATA, TERMS, FIRST, LAST]

  );

SKIMDATA[DATA_, NUMBER_] := (

    FCN[X_] := INTERPOLATION[DATA][X];

    LEN = LENGTH[DATA];

    DX = (DATA[[LEN]][[1]] - DATA[[1]][[1]])/NUMBER;

    XX[N_] := DATA[[1]][[1]] + N*DX;

    TABLE[{XX[N], FCN[XX[N]]}, {N, 0, NUMBER}]

  );

THRESHOLD[DATA_, OFFSET_] := MIN[PART[TRANSPOSE[DATA], 2]] - OFFSET;

TREATDATA[DATA_, OFFSET_] := (

    THRHLD = THRESHOLD[DATA, OFFSET];

    TABLE[{DATA[[N]][[1]], DATA[[N]][[2]] - THRHLD}, {N, 1, LENGTH[DATA]}]

  );


(* INTEGRATES OVER DATA    *)

DATASUM[DATA_] := SUM[DATA[[N]][[2]]*(DATA[[LENGTH[DATA]]][[1]] -

        DATA[[1]][[1]])/LENGTH[DATA], {N, 1, LENGTH[DATA]}];


(* BESTLPEAK FINDS BEST L VALUE BASED ON POSITION OF PEAK IN DATA *)

BESTLPEAK[DATA_] := (

    PEAKLAMBDA = PEAKFIND[DATA][[1]];

    LOWLAM = DATA[[1]][[1]];

    HIGHLAM = DATA[[LENGTH[DATA]]][[1]];
```

```
    L /. FINDROOT[PEAKLAMBDA ==

        (W /.FINDMINIMUM[1/INTENSITY[W, L], {W, LOWLAM, HIGHLAM}][[2]]), {L, 1, 10}]

    );

COMPAREPEAK[DATA_] := (

    PLT1 = LISTPLOT[DATA];

    LVAL = BESTLPEAK[DATA];

    PRINT["BEST FITTED L=", LVAL];

    PEAKDATA = PEAKFIND[DATA];

    NORMDATA = PEAKDATA[[2]];

    LEN = LENGTH[DATA];

    NORMFIT = INTENSITY[W = PEAKDATA[[1]], LVAL];

    PLT2 =

        PLOT[NORMDATA*INTENSITY[W, LVAL]/NORMFIT, {W, DATA[[1]][[1]],

        DATA[[LEN]][[1]]}];

    SHOW[PLT1, PLT2, PLOTLABEL -> "COMPARISON OF DATA WITH BEST PEAK FIT"];

    );


(*  FWHM FINDS FULL WIDTH AT HALF MAX FOR INTERPOLATED DATA  *)

FWHM[DATA_] := (

    CHEKPTS = 100;

    LEN = LENGTH[DATA];

    START = DATA[[1]][[1]];

    ENDD = DATA[[LEN]][[1]];

    PEAK = PEAKFIND[DATA];

    CURVE[X_] := INTERPOLATION[DATA][X];

    FIRST = CATCH[FOR[FIRST = START;
```

```
        JJ = 0, JJ ≤ CHEKPTS, JJ++,

        LAMFRONT = START + JJ*(ENDD - START)/CHEKPTS;

        IF[CURVE[LAMFRONT] > PEAK[[2]]/2, THROW[LAMFRONT]];

      ]];

    LAST = CATCH[FOR[LAST = ENDD;

      KK = 0, KK ≤ CHEKPTS, KK++,

      LAMBACK = ENDD - KK*(ENDD - START)/CHEKPTS;

      IF[CURVE[LAMBACK] > PEAK[[2]]/2, THROW[LAMBACK]];

      ]];

    LAST - FIRST

  );

FWHMTHEORY[DATA_, L_] := (

    CHEKPTS = 100;

    LEN = LENGTH[DATA];

    START = DATA[[1]][[1]];

    ENDD = DATA[[LEN]][[1]];

    THEORYCURVE[X_] := INTENSITY[X, L];

    PEAK = 1/(FINDMINIMUM[1/THEORYCURVE[XX], {XX, {START, ENDD}}][[1]]);

    FIRSTLAM = CATCH[FOR[FIRST = START;

      JJ = 0, JJ ≤ CHEKPTS, JJ++,

      LAMFRONT = START + JJ*(ENDD - START)/CHEKPTS;

      IF[THEORYCURVE[LAMFRONT] > PEAK/2, THROW[LAMFRONT]];

      ]];

    LASTLAM = CATCH[FOR[LAST = ENDD;

      KK = 0, KK ≤ CHEKPTS, KK++,

      LAMBACK = ENDD - KK*(ENDD - START)/CHEKPTS;
```

```
        IF[THEORYCURVE[LAMBACK] > PEAK/2, THROW[LAMBACK]];

    ]];

    LASTLAM - FIRSTLAM

  );

(*  FINDS BEST L BASED ON FITTING WIDTHS OF THEORY AND DATA *)

BESTLFWHM[DATA_] := LL /. FINDROOT[FWHMTHEORY[DATA, LL] == FWHM[DATA], {LL,

        {1, 100}}];

JLMATKHFWHM[L_, DATA_] := (

    BSTL = BESTLFWHM[DATA];

    NORMDATA = DATASUM[DATA];

    LEN = LENGTH[DATA];

    NORMFIT = NINTEGRATE[INTENSITY[WW, BSTL], {WW, DATA[[1]][[1]], DATA[[

        LEN]][[1]]}];

    SUM[(INTENSITY[DATA[[N]][[1]], L]/NORMFIT - DATA[[N]][[2]]/NORMDATA)^2, {N, 1,

        LEN}]

  );


(*  BESTLSQPK FINDS BEST L BASED ON RENORM MIN SQUARE DEVIATION  *)

BESTLSQFWHM[DATA_] := (

    BSTL = BESTLFWHM[DATA];

    NORMDATA = DATASUM[DATA];

    LEN = LENGTH[DATA];

    NORMFIT = NINTEGRATE[INTENSITY[WW, BSTL], {WW, DATA[[1]][[1]], DATA[[

        LEN]][[1]]}];

    {BSTL, LL /. FINDMINIMUM[SUM[(INTENSITY[DATA[[N]][[1]], LL]/NORMFIT -

        DATA[[N]][[2]]/NORMDATA)^2, {N, 1, LEN}], {LL, {1, 10}}][[2]]
```

132

```
    );

BESTLSQIT[DATA_, TIMES_] := (

    BSTL = BESTLFWHM[DATA];

    NORMDATA = DATASUM[DATA];

    LEN = LENGTH[DATA];

    TRIALL = BSTL;

    FOR[JJ = 1, JJ ≤ TIMES, JJ++,

      NORMFIT = NINTEGRATE[INTENSITY[WW, TRIALL], {WW, DATA[[1]][[1]],

        DATA[[LEN]][[1]]}];

        TRIALL = LL /. FINDMINIMUM[SUM[(INTENSITY[DATA[[N]][[1]], LL]/NORMFIT -

                DATA[[N]][[2]]/NORMDATA)^2, {N, 1, LEN}], {LL, {1, 10}}][[2]];

      ];

    TRIALL

    );

COMPARESQIT[DATA_, ITERATIONS_] := (

    PLT1 = LISTPLOT[DATA];

    LVL = BESTLSQIT[DATA, ITERATIONS];

    PRINT["BEST FITTED L=", LVL, "NANOMETERS"];

    NORMDATA = DATASUM[DATA];

    LEN = LENGTH[DATA];

    NORMFIT = NINTEGRATE[INTENSITY[W, LVL], {W, DATA[[1]][[1]], DATA[[LEN]][[1]]}];

    PLT2 =

      PLOT[NORMDATA*INTENSITY[W, LVL]/NORMFIT, {W, DATA[[1]][[1]],

        DATA[[LEN]][[1]]}];

    SHOW[PLT1, PLT2, PLOTLABEL -> "COMPARISON OF DATA WITH BEST FIT"];

    LVL
```

```
);


(* FITNCOMPARE GIVES BEST L = NANOCRYSTALLITE SIZE FOR

    ARRAYNM DATAPOINTS FROM MINIMUM OMEGA WMIN TO MAXIMUM OMEGA WMAX,

    GIVING A BACKGROUND SIZE ABOVE THE MINIMUM DATAVALUE OF BACKGRND,

    SMOOTHING THE DATA BY AVERAGING OVER PTS2AV POINTS, MINIMIZING THE

    DEVIATIONS OVER SKIMPTS FINAL NUMBER OF POINTS, AND INTERATING

    INTERATIONS TIMES *)

FITNCOMPARE[ARRAYNM_, WMIN_, WMAX_, BACKGRND_, PTS2AV_, SKIMPTS_,

        ITERATIONS_] :=

  COMPARESQIT[SKIMDATA[TREATDATA[SMOOTHWAVE[ARRAYNM, PTS2AV, WMIN,

        WMAX], BACKGRND], SKIMPTS], ITERATIONS];


TKHDATPTS0 = READLIST["D:\SICT7A.TXT", {REAL, REAL}];

TKHDATPTS7 = READLIST["D:\SICT7A.TXT", {REAL, REAL}];


BACKGRND = 10;

TREATDAT0 = TREATDATA[SMOOTHWAVE[TKHDATPTS0, 3, 900, 1000], BACKGRND];

TREATDAT7 = TREATDATA[SMOOTHWAVE[TKHDATPTS7, 3, 900, 1000], BACKGRND];


POINTS = 15;  (*  NUMBER OF SKIMMED POINTS TO FIT   *)

SKIMDAT0 = SKIMDATA[TREATDAT0, POINTS];

SKIMDAT7 = SKIMDATA[TREATDAT7, POINTS];


BESTL[DATA_, TIMES_, SKIMPOINTS_] := (

    BSTLL = BESTLFWHM[DATA];
```

```
SKIMPTS = SKIMDATA[DATA, SKIMPOINTS];

NORMDATA = DATASUM[SKIMPTS];

LEN = LENGTH[SKIMPTS];

TRIALL = BSTLL;

FOR[JJ = 1, JJ ≤ TIMES, JJ++,

  NORMFIT = NINTEGRATE[INTENSITY[WW, TRIALL], {WW, SKIMPTS[[1]][[1]],

     SKIMPTS[[LEN]][[1]]}];

 TRIALL = LL /. FINDMINIMUM [SUM[(INTENSITY[SKIMPTS[[N]][[1]], LL]/NORMFIT -

     SKIMPTS[[N]][[2]]/NORMDATA)^2, {N, 1, LEN}], {LL, {1, 10}}][[2]];

  ];

  TRIALL

 );


COMPAREPLOT[DATA_, ITERATIONS_, SKIMPOINTS_] := (

  PLT0 = LISTPLOT[TREATDAT0, PLOTJOINED -> TRUE,

     PLOTSTYLE -> RGBCOLOR[1, 0, 0], PLOTLABEL -> "POINTS0"];

  PLT1 = LISTPLOT[DATA, PLOTLABEL -> "TREATED DATAPOINTS"];

  LVL = BESTL[DATA, ITERATIONS, SKIMPOINTS];

  NORMDATA = DATASUM[DATA];

  LEN = LENGTH[DATA];

  NORMFIT = NINTEGRATE[INTENSITY[W, LVL], {W, DATA[[1]][[1]],

     DATA[[LEN]][[1]]}];

  PLT2 = PLOT[NORMDATA*INTENSITY[W, LVL]/NORMFIT, {W, DATA[[1]][[1]],

    DATA[[LEN]][[1]]}

     PLOTLABEL -> "THEORETICAL BEST FIT OF TREATED DATAPOINTS"];

  PRINT["BEST FITTED L=", LVL, "  NANOMETERS"];
```

```
    SHOW[PLT0, PLT1, PLT2, PLOTLABEL -> "COMPARISON OF DATA WITH BEST FIT"];

    LVL

  );


RENORMINTENSITY[DATA_, W_, LL_] := (

    NORMDATA = DATASUM[DATA];

    LEN = LENGTH[DATA];

    NORMFIT = NINTEGRATE[INTENSITY[WWW, LL], {WWW, DATA[[1]][[1]],

        DATA[[LEN]][[1]]}];

    NORMDATA*INTENSITY[W, LL]/NORMFIT

  );


DATANTHEORY[DATA_, LL_] := (

    LEN = LENGTH[DATA];

    TABLE[{DATA[[NNN]][[1]], DATA[[NNN]][[2]],

    RENORMINTENSITY[DATA, DATA[[NNN]][[1]], LL]}, {NNN, 1, LEN}]

  );

PLT0 = LISTPLOT[TREATDAT0, PLOTJOINED -> TRUE,

    PLOTSTYLE -> RGBCOLOR[1, 0, 0], PLOTLABEL -> "POINTS0"];

PLT7 = LISTPLOT[TREATDAT7, PLOTJOINED -> TRUE,

    PLOTSTYLE -> RGBCOLOR[0, 0, 1], PLOTLABEL -> "POINTS7"];

SHOW[PLT0, PLT4, PLT7, PLOTLABEL -> "ALL POINTS"];
```
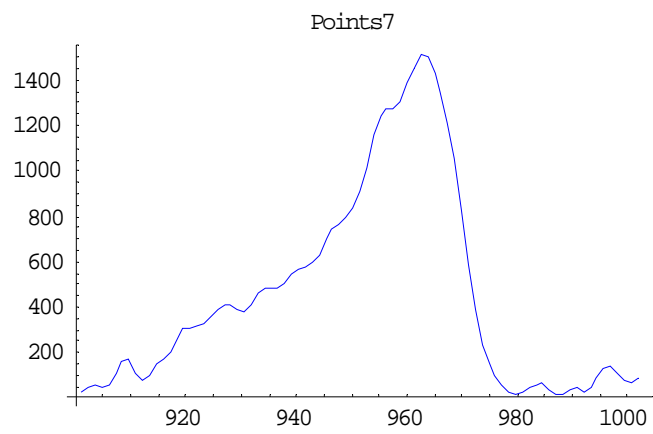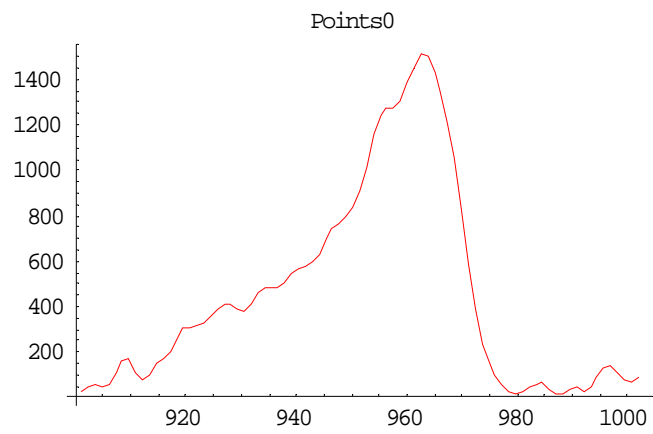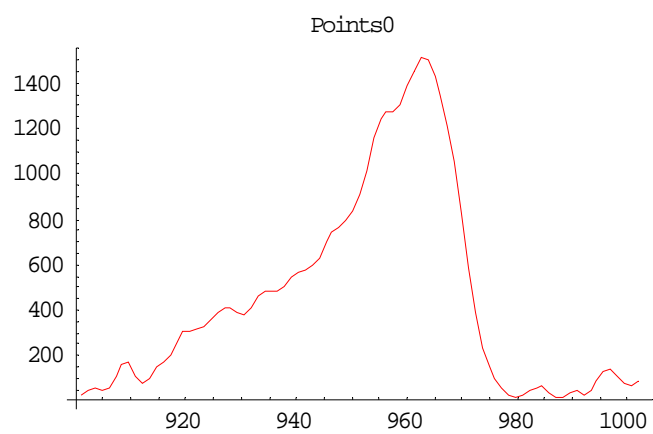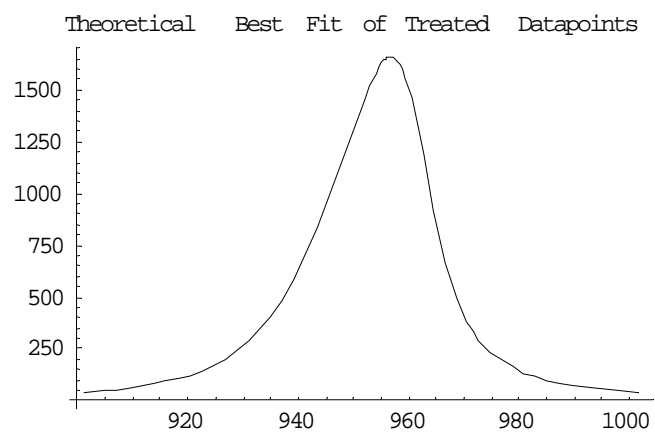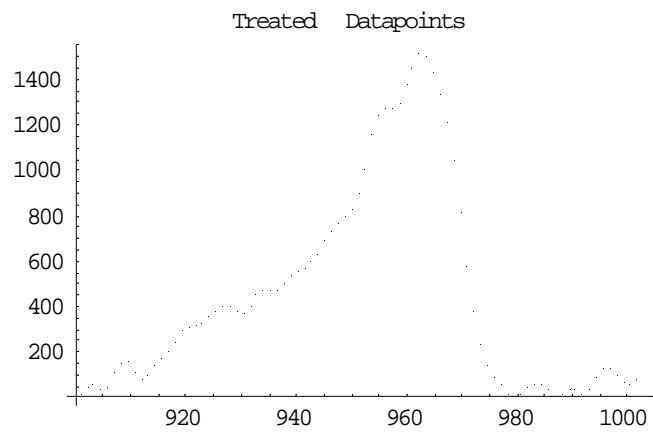
Points0

Points7

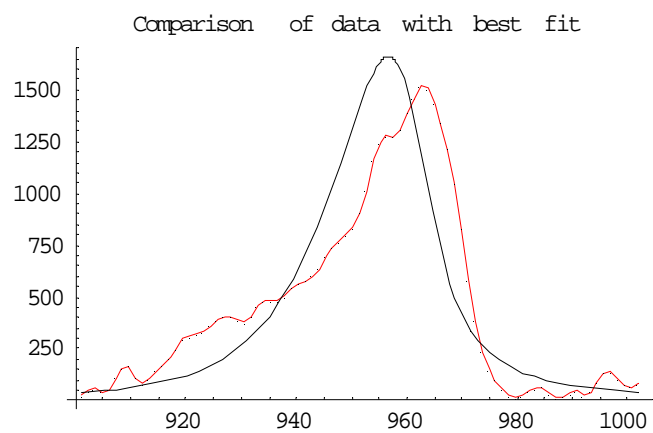compareplot[treatdat7, iterations = 2, skimpoints = 15];

Points0

Treated Datapoints

Theoretical   Best Fit of Treated Datapoints

"Best Fitted L="\[InvisibleSpace]15.2803\[InvisibleSpace]" nanometers"

Comparison   of data with best fit

{{901.036, 24.0333, 38.6076}, {902.266, 48.5333, 40.8618}, {903.496, 57.3333, 43.3257}, {904.725, 41.9333, 46.0247}, {905.955, 52.3, 48.9876}, {907.185, 110.767, 52.2468}, {908.415, 157.167, 55.8396}, {909.644, 166.767, 59.8081}, {910.874, 110.433, 64.2003}, {912.104, 80.3667, 69.0705}, {913.333, 101.367, 74.4807}, {914.563, 145., 80.5009}, {915.793, 173.233, 87.2109}, {917.023, 203.633, 94.7006}, {918.252, 247.867, 103.072}, {919.482, 300.933, 112.441}, {920.712, 308.567, 122.937}, {921.942, 320.033, 134.706}, {923.171, 329.933, 147.913}, {924.401, 359.867, 162.741}, {925.631, 389.067, 179.395}, {926.86, 407.7, 198.103}, {928.09, 407.633, 219.116}, {929.32, 387.433, 242.712}, {930.55, 375.333, 269.192}, {931.779, 404.7, 298.883}, {933.009, 456.733, 332.135}, {934.239, 479.3, 369.32}, {935.469, 481.2, 410.824}, {936.698, 478.9, 457.041}, {937.928, 505.533, 508.359}, {939.158, 541.333, 565.146}, {940.387, 564.5, 627.728}, {941.617, 575.767, 696.355}, {942.847, 597.8, 771.163}, {944.077, 633.233, 852.118}, {945.306, 699.433, 938.951}, {946.536, 739.567, 1031.07}, {947.766, 767.833, 1127.45}, {948.996, 797.667, 1226.49}, {950.225, 834.233, 1325.89}, {951.455, 909.233, 1422.44}, {952.685, 1011.7, 1511.86}, {953.914, 1162.43, 1588.63}, {955.144, 1247.77, 1645.99}, {956.374, 1276.57, 1676.09}, {957.604, 1275.6, 1670.69}, {958.833, 1305.63, 1622.61}, {960.063, 1384.8, 1528.31}, {961.293, 1455.7, 1391.17}, {962.523, 1515.47, 1223.69}, {963.752, 1507.97, 1045.38}, {964.982, 1433.07, 875.731}, {966.212, 1343.77, 727.346}, {967.441, 1215.1, 604.359}, {968.671, 1052.57, 505.248}, {969.901, 825.967, 426.189}, {971.131, 585.5, 363.089}, {972.36, 385.933, 312.405}, {973.59, 235.033, 271.324}, {974.82, 148.467, 237.689}, {976.05, 97.0667, 209.867}, {977.279, 57.9667, 186.627}, {978.509, 25.0333, 167.033}, {979.739, 10., 150.371}, {980.969, 21.3, 136.089}, {982.198, 46.6667, 123.757}, {983.428, 58.9333, 113.036}, {984.658, 63.5333, 103.658}, {985.887, 36.7667, 95.4082}, {987.117, 13.6, 88.112}, {988.347, 16.5, 81.6279}, {989.577, 36.5, 75.8392}, {990.806, 45.1, 70.6498}, {992.036, 24.8667, 65.9794}, {993.266, 42.9, 61.7607}, {994.496, 88.2667, 57.937}, {995.725, 131.833, 54.4605}, {996.955, 136.333, 51.29}, {998.185, 105.033, 48.3905}, {999.414, 74.1333, 45.732}, {1000.64, 62.7, 43.2881}, {1001.87, 82.4333, 41.0364}}

VITA

Tilghman Lee Rittenhouse was born in Phoenix, Arizona, on 20 May 1972. He graduated from the United States Air Force Academy (Colorado Springs, CO) in 1994 with a bachelor's degree in Materials Science and Engineering. As an undergraduate, Tim participated in summer research at Wright Patterson Air Force Base (Dayton, OH) as well as numerous military and flying programs. Upon graduation, Tim was designated a distinguished graduate. Following graduation, Tim served three years at Kirtland Air Force Base (Albuquerque, NM) developing chemical oxygen-iodine laser systems for the airborne laser program. Next, Tim attended the Massachusetts Institute of Technology (Cambridge, MA) and was awarded a master's degree in Materials Science and Engineering in 1999 under the direction of Dr. August Witt. Tim's thesis work at MIT involved Czochralski growth of silicon-germanium alloys, comparing the micro- and macrosegregation effects on earth to experiments conducted in zero-g. Tim then returned to the United States Air Force Academy, where he was an instructor of general chemistry and physical chemistry laboratory courses from 1999-2001. While instructing at USAFA, Tim also lead a research group of senior cadets involved in forming fine dense powders of lithium aluminum hexahydride as a hydrogen fuel source. Tim's graduate study at the University of Illinois (Urbana, IL) under the direction of Professor Paul W. Bohn studied the formation of porous silicon carbide films and their ability to sense chemicals at elevated temperatures. Following the completion of his Ph.D., Tim will be returning to an operational assignment at Patrick Air Force Base, FL.

CERTIFICATE OF COMMITTEE APPROVAL

University of Illinois at Urbana-Champaign
Graduate College

We hereby recommend that the thesis by:

Entitled:

Be accepted in partial fulfillment of the requirements for the degree of:

Signatures:

_____   _____
Director of Research -   *Head of Department -*

Committee on Final Examination*

_____   _____
Chairperson -   *Committee Member -*

_____   _____
Committee Member -   *Committee Member -*

_____   _____
Committee Member -   *Committee Member -*

* Required for doctoral degree but not for master's degree